# Plasma-Induced Chemical Processing for Biomolecules in Aqueous Solution

EISUKE TAKAI

Doctoral Program in Applied Physics

Submitted to the Graduate School of
Pure and Applied Sciences
in Partial Fulfillment of the Requirements
for the Degree of Doctor of Philosophy in
Engineering

at the
University of Tsukuba

# Content

# Chapter 1

# General Introduction

## Medical applications of atmospheric-pressure plasma

In physical sciences, “plasma” refers to the fourth state of matter; on the other hand, in medicine and biology plasma is known as the non-cellular fluid component of blood. Intriguingly, the term plasma has been coined by Irving Langmuir to emphasize that the characteristics of ionic liquids ubiquitous in biology and medicine are analogous to plasma in the physical sciences [1]. Recently, it is expected to inform the development of plasma medicines [2] for cancer [3-6], glioma [7], blood coagulation [8], disruption of the human hepatocyte cytoskeleton [9], sterilization [10-19], and Parkinson’s disease [20]. Therefore, plasma medicine is an attractive new research area [21-23].

## Low-frequency plasma jet generates reactive oxygen species

Atmospheric-pressure cold plasma (APCP) has been used for various applications and has many advantages: (i) inexpensive operation costs in vacuum-free systems; (ii) use of a moderate gas temperature; (iii) facilitation of delicate and flexible operations; and (iv) generation of reactive oxygen species (ROS) [24], typically hydroxyl radicals (OH•) [25-29], superoxide anion radicals ($O_2^-$•) [30], hydroperoxy radicals (HOO•) [31], singlet oxygen ($^1O_2$), and atomic oxygen (O) [32]. These features of APCP enable the exploitation of a novel field of chemical reactions both in solution [33-35] and under dry conditions. In particular, medical applications using ROS generated by APCP is at the center of intense research efforts [36].

For the study, a low-frequency (LF) plasma jet was used for the APCP processing. The plasma shape was elongated from the end of a glass tube, in which helium gas flowed, by the application of an alternating-current high voltage (ranging from -3.5 to +5.0 kV at a frequency of 13.9 kHz) to a single-sided electrode. Helium plasma with a low gas temperature was generated in an elongated shape. The discharge power of the plasma was approximately 3 W. Various active oxygen species such as superoxide anion radicals produced from $O_2$ of the ambient gas by the plasma were supplied to the solution. Thus, plasma-induced chemical processing, which diffuse into the liquid phase and thus react with substances in solution, is induced by LF plasma jet.

## The reduced pH method for plasma sterilization

Sterilization in aqueous solution is one of the most in-demand applications of plasma medicine because the organism is also present in aqueous conditions, such as root canal therapy in dentistry [37] and the prevention of surgical site infection [38]. For sterilization in aqueous solution, our research group has presented a new method of plasma sterilization, named “the reduced pH method”, by which plasma sterilization in solution under acidic conditions (pH <4.8) occurs much more efficiently than under neutral conditions (pH 6.5) [31].

The assumed mechanism of plasma sterilization in solution using the reduced pH method is as follow [38]. The plasma-generated $O_2^-$• in air diffuses into solution. $O_2^-$• in the solution is known to be in equilibrium with HOO• in which acid dissociation constant is pH 4.8 [39, 40]. This reaction means that $O_2^-$• converts into HOO• at lower pH conditions (<4.8). Unlike the charged molecular $O_2^-$•, the non-charged molecular HOO• easily permeates into the cell membrane, of which the lipid bilayer has a permselective property. Therefore, the HOO• can then react with biomolecules inside the cell and cause various molecular changes to induce highly effective bacterial inactivation.

## Fundamental understanding of the chemical effect

Proteins are built from series of up to twenty $_L$-amino acids and have all functions in biological systems. For example, proteins play roles such as catalyst, transporter and scaffolding in cytoplasm. These proteins are different from most of synthetic polymers because of their structure accounted for by the unique monomer unit. Most of the proteins fold into characteristic shape by following the sequence of the monomer units in contrast with synthetic polymers. Interactions involved in the protein folding are van der Waals force, hydrogen bond, and electrostatic and hydrophobic interactions. Among them, hydrogen bond confines the protein conformation and, therefore it mainly defines their characteristic structure.

Although various biomedical applications of the atmospheric pressure plasma have been developed over the past decade, fundamental understanding of interactions between plasma and biomacromolecules has remained insufficient. Few experiments have examined the atmospheric pressure plasma destructed the tertiary structure of DNA in aqueous solution [41, 42] and degradation of protein in dry conditions [43, 44]. Recently, it has been reported that the APCP degrades proteins in aqueous solution. For example, APCP inactivates infectious prion protein [45], activates lipase in solution after treated within one minute [46], and inactivates recombinant green fluorescent protein (GFP) in E. coli cells [47].

## Objective for this study

Plasma medicine is an attractive new research area, but fundamental understanding of interaction between plasma and biomolecules and molecular mechanism of plasma medicine has remained insufficient. In this study, we investigated the chemical effects of atmospheric-pressure cold plasma on an enzyme hen egg white lysozyme, 20 naturally occurring amino acids, and amyloid-ß fibrils in aqueous solution and the mechanism of plasma sterilization in solution using the reduced pH method. These data provide fundamental information for elucidating the mechanism of protein inactivation and sterilization for biomedical plasma applications.

## References


[1] Compton K T and Langmuir I 1930 Electrical Discharges in Gases. Part I. Survey of Fundamental Processes *Reviews of Modern Physics* **2** 123-242

[2] Babaeva N Y and Kushner M J 2013 Reactive fluxes delivered by dielectric barrier discharge filaments to slightly wounded skin *J. Phys. D: Appl. Phys.* **46** 025401

[3] Sato T, Yokoyama M and Johkura K 2011 A key inactivation factor of HeLa cell viability by a plasma flow *J. Phys. D: Appl. Phys.* **44** 372001

[4] Kim K, Choi J D, Hong Y C, Kim G, Noh E J, Lee J-S and Yang S S 2011 Atmospheric-pressure plasma-jet from micronozzle array and its biological effects on living cells for cancer therapy *Appl. Phys. Lett.* **98** 073701

[5] Kim S J, Chung T H, Bae S H and Leem S H 2010 Induction of apoptosis in human breast cancer cells by a pulsed atmospheric pressure plasma jet *Appl. Phys. Lett.* **97** 023702

[6] Kim C H, Kwon S, Bahn J H, Lee K, Jun S I, Rack P D and Baek S J 2010 Effects of atmospheric nonthermal plasma on invasion of colorectal cancer cells *Appl. Phys. Lett.* **96** 243701

[7] Vandamme M, Robert E, Pesnel S, Barbosa E, Dozias S, Sobilo J, Lerondel S, Le Pape A and Pouvesle J M 2010 Antitumor Effect of Plasma Treatment on U87 Glioma Xenografts: Preliminary Results *Plasma Processes and Polymers* **7** 264-73

[8] Fridman G, Peddinghaus M, Balasubramanian M, Ayan H, Fridman A, Gutsol A and Brooks A 2006 Blood Coagulation and Living Tissue Sterilization by Floating-Electrode Dielectric Barrier Discharge in Air *Plasma Chem. Plasma Process.* **26** 425-42

[9] Gweon B, Kim D, Kim D B, Jung H, Choe W and Shin J H 2010 Plasma effects on subcellular structures *Appl. Phys. Lett.* **96** 101501

[10] Perni S, Shama G, Hobman J L, Lund P A, Kershaw C J, Hidalgo-Arroyo G A, Penn C W, Deng X T, Walsh J L and Kong M G 2007 Probing bactericidal mechanisms induced by cold atmospheric plasmas with Escherichia coli mutants *Appl. Phys. Lett.* **90** 073902

[11] Feng H Q, Wang R X, Sun P, Wu H Y, Liu Q, Fang J, Zhu W D, Li F T and Zhang J 2010 A study of eukaryotic response mechanisms to atmospheric pressure cold plasma by using Saccharomyces cerevisiae single gene

mutants *Appl. Phys. Lett.* **97** 131501

[12] Bussiahn R, Brandenburg R, Gerling T, Kindel E, Lange H, Lembke N, Weltmann K D, von Woedtke T and Kocher T 2010 The hairline plasma: An intermittent negative dc-corona discharge at atmospheric pressure for plasma medical applications *Appl. Phys. Lett.* **96** 143701

[13] Kolb J F, Mohamed A A H, Price R O, Swanson R J, Bowman A, Chiavarini R L, Stacey M and Schoenbach K H 2008 Cold atmospheric pressure air plasma jet for medical applications *Appl. Phys. Lett.* **92** 241501

[14] Zhang X, Huang J, Liu X, Peng L, Guo L, Lv G, Chen W, Feng K and Yang S-z 2009 Treatment of Streptococcus mutans bacteria by a plasma needle *J. Appl. Phys.* **105** 063302

[15] Lu X, Ye T, Cao Y, Sun Z, Xiong Q, Tang Z, Xiong Z, Hu J, Jiang Z and Pan Y 2008 The roles of the various plasma agents in the inactivation of bacteria *J. Appl. Phys.* **104** 053309

[16] Majumdar A, Singh R K, Palm G J and Hippler R 2009 Dielectric barrier discharge plasma treatment on E. coli: Influence of CH[sub 4]/N[sub 2], O[sub 2], N[sub 2]/O[sub 2], N[sub 2], and Ar gases *J. Appl. Phys.* **106** 084701

[17] Burlica R, Grim R G, Shih K Y, Balkwill D and Locke B R 2010 Bacteria Inactivation Using Low Power Pulsed Gliding Arc Discharges with Water Spray *Plasma Processes and Polymers* **7** 640-9

[18] Zhang Q, Liang Y, Feng H, Ma R, Tian Y, Zhang J, Fang J 2013 A study of oxidative stress induced by non-thermal plasma-activated water for bacterial damage *Appl. Phys. Lett.* **102** 203701

[19] Nagatsu M, Zhao Y, Motrescu I, Mizutani R, Fujioka Y and Ogino A 2012 Sterilization Method for Medical Container Using Microwave-Excited Volume-Wave Plasma *Plasma Processes and Polymers* **9** 590-6

[20] Karakas E, Munyanyi A, Greene L and Laroussi M 2010 Destruction of alpha-synuclein based amyloid fibrils by a low temperature plasma jet *Appl. Phys. Lett.* **97** 143702

[21] Fridman G, Friedman G, Gutsol A, Shekhter A B, Vasilets V N and Fridman A 2008 Applied plasma medicine *Plasma Processes and Polymers* **5** 503-33

[22] Kong M G, Kroesen G, Morfill G, Nosenko T, Shimizu T, van Dijk J and Zimmermann J L 2009 Plasma medicine: an introductory review *New J Phys* **11** 115012

[23] Morfill G E, Kong M G and Zimmermann J L 2009 Focus on Plasma Medicine *New J Phys* **11**

[24] Bruggeman P, Iza F, Lauwers D and Gonzalvo Y A 2010 Mass spectrometry study of positive and negative ions in a capacitively coupled atmospheric pressure RF excited glow discharge in He-water mixtures *J Phys D Appl Phys* **43** 012003

[25] Locke B R, Sato M, Sunka P, Hoffmann M R and Chang J S 2006 Electrohydraulic discharge and nonthermal plasma for water treatment *Ind. Eng. Chem. Res.* **45** 882-905

[26] Sahni M and Locke B R 2006 The effects of reaction conditions on liquid-phase hydroxyl radical production in gas-liquid pulsed-electrical-discharge reactors *Plasma Processes and Polymers* **3** 668-81

[27] Sahni M and Locke B R 2006 Quantification of hydroxyl radicals produced in aqueous phase pulsed electrical discharge reactors *Ind. Eng. Chem. Res.* **45** 5819-25

[28] Bruggeman P and Leys C 2009 Non-thermal plasmas in and in contact with liquids *J Phys D Appl Phys* **42** 053001

[29] Burlica R, Shih K Y and Locke B R 2010 Formation of H-2 and H2O2 in a Water-Spray Gliding Arc Nonthermal Plasma Reactor *Ind. Eng. Chem. Res.* **49** 6342-9

[30] Tani A, Ono Y, Fukui S, Ikawa S and Kitano K 2012 Free radicals induced in aqueous solution by non-contact atmospheric-pressure cold plasma *Appl. Phys. Lett.* **100** 254103

[31] Ikawa S, Kitano K and Hamaguchi S 2010 Effects of pH on Bacterial Inactivation in Aqueous Solutions due to Low-Temperature Atmospheric Pressure Plasma Application *Plasma Processes and Polymers* **7** 33-42

[32] Liu D X, Rong M Z, Wang X H, Iza F, Kong M G and Bruggeman P 2010 Main Species and Physicochemical Processes in Cold Atmospheric-pressure He + O-2 Plasmas *Plasma Processes and Polymers* **7** 846-65

[33] Furusho H, Miyamoto D, Nagasaki Y, Kitano K and Hamaguchi S 2007 Synthesis of uniformly dispersed metal nanoparticles with dispersion stability by nonequilibrium atmospheric plasma jets *J. Photopolym. Sci. Technol.* **20** 229-33

[34] Furusho H, Kitano K, Hamaguchi S and Nagasaki Y 2009 Preparation of Stable Water-Dispersible PEGylated Gold Nanoparticles Assisted by Nonequilibrium Atmospheric-Pressure Plasma Jets *Chem. Mater.* **21** 3526-35

[35] Sumitani S, Murotani H, Oishi M, Kitano K, Hamaguchi S and Nagasaki Y 2009 Nonequilibrium Atmospheric Plasma Jets Assisted Stabilization of Drug Delivery Carriers: Preparation and Characterization of Biodegradable Polymeric Nano-Micelles with Enhanced Stability *J. Photopolym. Sci. Technol.* **22** 467-71

[36] Graves D B 2012 The emerging role of reactive oxygen and nitrogen species in redox biology and some implications for plasma applications to medicine and biology *J Phys D Appl Phys* **45**

[37] Yamazaki H, Ohshima T, Tsubota Y, Yamaguchi H, Jayawardena J A and Nishimura Y 2011 Microbicidal activities of low frequency atmospheric pressure plasma jets on oral pathogens *Dent. Mater. J.* **30** 384-91

[38] K. Kitano S I, A. Tani, T. Ohshima, H. Yamaguchi, H. Yamazaki, R. Arakawa, T. Kitamura, and N. Ohnishi, Innovative plasma disinfection of bacteria in water by the reduced pH method combined with free radicals supplied by non-contact atmospheric plasma *in Proceedings of the 20th International Symposium on Plasma Chemistry (ISPC-20), Philadelphia, USA, 24–29 July 2011, p. 17.*

[39] Bielski B H J, Cabelli D E, Arudi R L and Ross A B 1985 Reactivity of Ho2/O-2 Radicals in Aqueous-Solution *J. Phys. Chem. Ref. Data* **14** 1041-100

[40] D. Behar G C, J. Rabani, Leon M. Dorfman, Harold A. Schwarz 1970 Acid dissociation constant and decay kinetics of the perhydroxyl radical *The Journal of Physical Chemistry* **74** 3209-13

[41] Yan X, Zou F, Lu X P, He G Y, Shi M J, Xiong Q, Gao X, Xiong Z L, Li Y, Ma F Y, Yu M, Wang C D, Wang Y S and Yang G X 2009 Effect of the atmospheric pressure nonequilibrium plasmas on the conformational changes of plasmid DNA *Appl. Phys. Lett.* **95** 083702

[42] Li G, Li H P, Wang L Y, Wang S, Zhao H X, Sun W T, Xing X H and Bao C Y 2008 Genetic effects of radio-frequency, atmospheric-pressure glow discharges with helium *Appl. Phys. Lett.* **92**

[43] Deng X T, Shi J J and Kong M G 2007 Protein destruction by a helium atmospheric pressure glow discharge: Capability and mechanisms *J. Appl. Phys.* **101**

[44] Deng X T, Shi J J, Chen H L and Kong M G 2007 Protein destruction by atmospheric pressure glow discharges *Appl. Phys. Lett.* **90** 013903

[45] Julák J, Janoušková O, Scholtz V and Holada K 2011 Inactivation of Prions Using Electrical DC Discharges at Atmospheric Pressure and Ambient Temperature *Plasma Processes and Polymers* **8** 316-23

[46] Li H-P, Wang L-Y, Li G, Jin L-H, Le P-S, Zhao H-X, Xing X-H and Bao C-Y 2011 Manipulation of Lipase Activity by the Helium Radio-Frequency, Atmospheric-Pressure Glow Discharge Plasma Jet *Plasma Processes and Polymers* **8** 224-9

[47] Yasuda H, Hashimoto M, Rahman M M, Takashima K and Mizuno A 2008 States of Biological Components in Bacteria and Bacteriophages during Inactivation by Atmospheric Dielectric Barrier Discharges *Plasma Processes and Polymers* **5** 615-21

# Chapter 2

# Mechanism of Plasma Sterilization Using the Reduced pH Method

## 2.1 Molecular Mechanism of Plasma Sterilization in Solution with the Reduced pH Method: Importance of Permeation of HOO Radicals into Cell Membrane

## Introduction

Low-temperature atmospheric-pressure plasma (LTAPP) has attracted considerable attention for use in various medical and life science applications. The merits for LTAPP are as follows: (i) inexpensive operation costs in vacuum-free systems, (ii) use of moderate gas temperature, (iii) facilitation of delicate and flexible operations, and (iv) generation of reactive oxygen species (ROS) [1], typically hydroxyl radicals (OH•) [2-6], superoxide anion radicals ($O_2^-$•) [7], hydroperoxy radicals (HOO•) [8], singlet oxygen ($^1O_2$), and atomic oxygen (O) [9]. These features allow for the exploitation of a novel field of chemical reaction in solution [10-12], as well as under dry conditions. For example, the recent pioneering applications of LTAPP include the development of plasma medicines [13, 14] for cancer [15-18], Parkinson's disease [19], blood coagulation [20], disruption of the human hepatocyte cytoskeleton [21], and sterilization [22-29].

The sterilization of bacteria in solution is one of the most in-demand applications of plasma medicine because the organism is also present in aqueous conditions, typically involving root canal therapy in dentistry [30] and the prevention of surgical site infection [31]. For sterilization of bacteria in solution, our research group has presented a new concept for plasma application in solution, called "plasma-induced chemical processing" [32] and a new method of plasma sterilization, named "the reduced pH method" [8]. Briefly, in plasma-induced chemical processing, LTAPP generates chemically reactive species in the gas phase, which diffuse into the liquid phase and thus react with

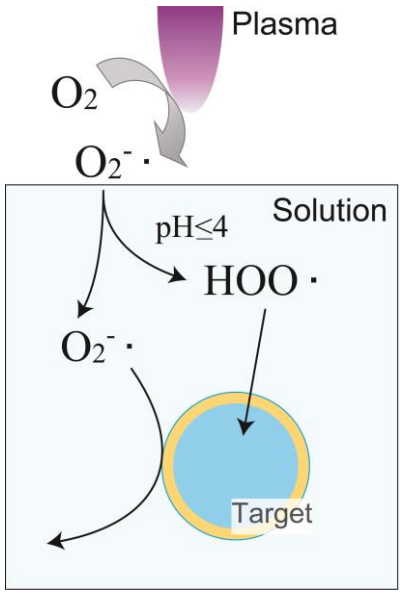


**Figure. 2.1.1.** Schematic mechanism of plasma sterilization in solution by using plasma-induced chemical processing and the reduced pH method. The "target" of the plasma sterilization corresponds to the test bacteria or the dye-included micelle as a bacterial model. The yellow layer of the target is the cell membrane or surfactant micelle, both of which are semi-permeable.

substances in solution. Plasma sterilization in solution under acidic conditions (pH <4.8) occurs much more efficiently than under neutral conditions (pH 6.5) when plasma-induced chemical processing and the reduced pH method are used [8].

The mechanism of plasma sterilization in solution using plasma-induced chemical processing and the reduced pH method is shown in Figure 2.1.1 by K. Kitano et al. [31]. The plasma-generated $O_2^-$• in air diffuses into solution. $O_2^-$• in the solution is known to be in equilibrium with HOO•, as shown by the following reaction [33, 34]:

$$O_2^- \cdot + H^+ \rightleftarrows HOO \cdot \qquad pK_a = 4.8 \qquad (1)$$

Here, $pK_a$ means acid dissociation constant. This reaction shows that $O_2^-$• converts into HOO• at lower pH conditions (<4.8). Unlike charged (anion) molecular $O_2^-$•, non-charged (neutral) HOO• easily permeates into the cell membrane, of which the lipid bilayer has a permselective property. The HOO• can then react with biomolecules inside the cell and cause various molecular changes such as conformational changes in DNA [34-37], DNA damage [38], and inactivation of enzymes [39], to induce bacterial inactivation.

Generally, the death rate of the bacteria is known to be proportional to the concentration of the bactericidal factor [40]. If the sterilization mechanism of the reduced pH method is actually

involved in the neutralization of $O_2^-$• to HOO•, the death rates should be proportional to the concentration of HOO• at various pH values. To evaluate this hypothesis, we investigated the experimental results by using 3 kinds of bacteria and a bacterial model of a micelle system and examined the chemical reactions of active species in solution.

# Materials and methods

## Materials

*Streptococcus mutans* JCM 5705 and *Campylobacter rectus* JCM 6301 were obtained from the RIKEN BioResource Center, Japan Collection of Microorganisms. *Escherichia coli* NBRC 3301 was obtained from Biological Resource Center, NITE. The soybean-casein digest (SCD) agar and sheep blood agar (SBA) plates were obtained from Nissui Pharmaceutical (Tokyo, Japan). The LB (Luria-Bertan) broth Miller and LB agar Miller plates were obtained from Becton, Dickinson and Company (Franklin Lakes, NJ, USA). Nile red was obtained from Sigma Chemical Co. (St. Louis, MO, USA). Tween 20 was obtained from Tokyo Kasei Kogyo Co. Ltd. (Tokyo, Japan). Sodium citrate, potassium chloride, glycine, citric acid, sodium phosphate, and sodium bicarbonate were obtained from Wako Pure Chemical Industries Ltd. (Osaka, Japan).

## Plasma jet generation

A low-frequency (LF) plasma jet was used in a manner similar to that described in a previous study [8]. The plasma shape is elongated from the end of a quartz glass tube, in which helium gas flows, by the application of an alternating current high voltage (ranging from -3.5 to +5.0 kV at a frequency of 13.9 kHz) to a single-sided electrode. The electrode consists of a small copper sheet wound around the glass tube (Fig. 2.1.2a). Helium plasma with a low gas temperature was generated in an elongated shape (Fig. 2.1.2b).

## Bacterial inactivation assay

*S. mutans* was cultivated on an SCD agar plate for 48 h at 37 °C. *C. rectus* was cultivated on an SBA plate for 48 h at 37 °C under anaerobic conditions. Both these cultivated bacteria samples were harvested from the surfaces of the plates. *E. coli* was cultivated in LB broth for 18 h at 30 °C with 110 rpm reciprocal shaking and was subsequently harvested by centrifugation. All harvested bacteria were suspended in an appropriate volume of distilled water (DW). The bacterial suspension was diluted with DW to $OD_{600} = 0.1$, which contained approximately $7 \times 10^7$ cells·$mL^{-1}$ of bacteria.

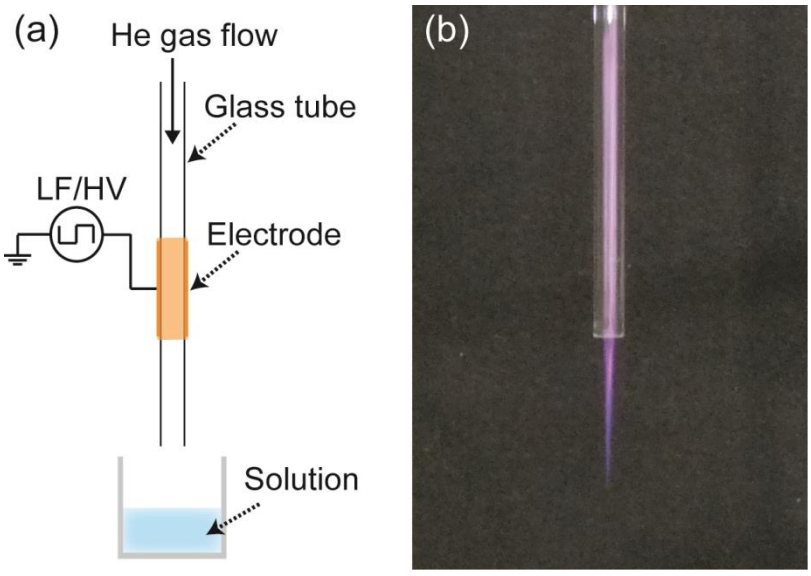


**Figure. 2.1.2.** Plasma jet system. (a) Schematic representation of the plasma jet system with a sample solution. The plume-like structure of the plasma extends toward the surface of a solution containing a bacterial suspension or surfactant micelles. (b) Photograph of the plasma jet. The plasma of helium gas flows through the glass tube. The discharge power of the plasma was 3 W.

Bacterial inactivation assays were performed in the following manner using LF plasma jets. The prepared bacterial suspension ($OD_{600}$ = 0.1) was diluted 10-fold with a 2.0 mM sodium citrate buffer (pH range of 6.5–3.7) and subsequently, 500 µL of this diluted solution was distributed into 24-well microplates. The plasma jet was applied to the surface of the bacteria suspension in each well for predetermined time intervals in ambient air. The tip of the tube that produces the plasma jets was located approximately 17 mm above the solution surface. The helium gas flow rate was 2.0 slm.

The number of living bacteria after plasma application was determined by a colony forming unit (CFU) assay performed as follows. After plasma exposure, the suspensions were recovered from the wells and DW was added to each recovered solution to replenish water lost by evaporation during the process. Subsequently, the solutions were serially diluted further with DW, and 100 µL of each dilution was spread on the SCD agar, blood agar, and LB agar plates used for *S. mutans*, *C. rectus*, and *E. coli*, respectively. These plates were incubated for 48 h at 37 °C (only *C. rectus* was incubated under anaerobic conditions), thereby enabling the development and subsequent counting of the bacterial colonies. The minimum detection value of the CFU assay in this study was 10 $CFU \cdot mL^{-1}$. The operations to plating for CFU assay from suspension of bacteria were terminated within 30 min.

## Dye decoloration assay of surfactant micelles

Surfactant micelles that included a dyeing agent were prepared by agitating a solution containing 116

μM Nile red and 20% v/v Tween 20 at 25 °C for 24 h. In the plasma exposure experiments, a 300-μL micelle sample containing 5.8 μM Nile red, 1% v/v Tween 20, and 100 mM buffer was applied to the vessel as the target solution. The buffers of the target solutions were potassium chloride at pH 1, glycine at pH 2, 3, 9, and 10, citric acid at pH 4–6, phosphate at pH 7 and 8, and bicarbonate at pH 11.

The decoloration assay measurements were obtained as follows. The plasma jet was generated within an airtight chamber (at its center) using the plasma generation device described above. The ambient gas in the chamber was controlled via an oxygen ($O_2$) gas supply port connected to the side of the plasma jet port to avoid the generation of nitrogen species that could affect the pH value. The flow rates of He and $O_2$ gas were 0.50 and 0.15 slm, respectively. To enable the exchange of ambient gas, He and $O_2$ gases were initially made to flow into the chamber for 5 min. The various reactive-oxygen species produced from $O_2$ gas by the helium plasma were supplied to the solution in the chamber.

# Results

## Calculation of the concentration of radicals

Radical species are generally unstable with short lifetimes; hence, it is impossible to determine the concentration of radicals in aqueous solution after plasma treatment. Here, we introduce the theoretical calculation of the concentration of HOO• and $O_2^-$•. The detail was cited in Reference 31.

The concentration of HOO• and $O_2^-$• as a function of pH was calculated considering not only acid dissociation equilibrium (eq (1)) but also dismutation of radicals (eq (2)–(4)). First, $O_2^-$• radials related to HOO•, as determined by eq (1), contribute to bacterial inactivation in aqueous solution [41] because of a long lifetime of $O_2^-$• (5 s at $1.0 \times 10^{-6}$ M) [42]. $O_2^-$• and HOO• are consumed in solution in the proportions indicated by equations (2)–(4) [33, 34].

$$O_2^- \bullet + HOO\bullet + H^+ \rightarrow H_2O_2 + O_2 \qquad k_1 = 9.7 \times 10^7\ M^{-1}s^{-1} \qquad (2)$$

$$HOO\bullet + HOO\bullet \rightarrow H_2O_2 + O_2 \qquad k_2 = 8.3 \times 10^5\ M^{-1}s^{-1} \qquad (3)$$

$$O_2^- \bullet + O_2^- \bullet + 2\ H^+ \rightarrow H_2O_2 + O_2 \qquad k_3 = 0.3\ M^{-1}s^{-1} \qquad (4)$$

Here, $k_1$, $k_2$, and $k_3$ denote the respective reaction rates. The supply of $O_2^-$• generated by plasma in the gas phase to the solution balances the consumption of $O_2^-$• and HOO• in solution. Consequently, using equations (1)–(4), the overall reaction can be written as below.

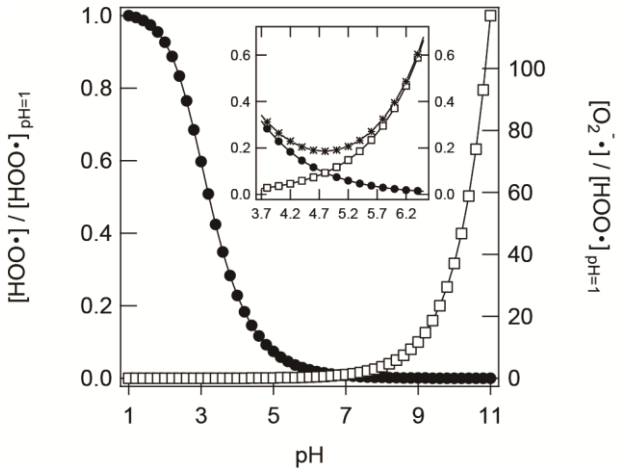


**Figure. 2.1.3.** The relative concentration of HOO• and $O_2^-$•. The HOO• concentration is described by equation (6) (with respect to the left axis, closed circle) and the $O_2^-$• concentration is described by equation (6) (with respect to the right axis, open square) for a pH range of 1.0–11.0. (Inset) The relative concentration of HOO•, $O_2^-$• and (HOO• + $O_2^-$•) at pH 3.7–6.5. The (HOO• + $O_2^-$•) concentration is shown by an asterisk. In the inset figure, the left and right axes show the same range.

$$\begin{aligned} V_s = V_d &= k_1[O_2^-\bullet][HOO\bullet] + k_2[HOO\bullet]^2 + k_3[O_2^-\bullet]^2 \\ &= k_1 \times 10^{(pH\,-\,4.8)}\,[HOO\bullet]^2 + k_2[HOO\bullet]^2 + k_3\times 10^{2(pH\,-\,4.8)}\,[HOO\bullet]^2 \\ &= k_1 \times 10^{(1-\,4.8)}\,([HOO\bullet]_{pH=1})^2 + k_2\,([HOO\bullet]_{pH=1})^2 + k_3\times 10^{2(1-\,4.8)}\,([HOO\bullet]_{pH=1})^2 \end{aligned} \quad (5)$$

Here, $V_s$ and $V_d$ denote the supply rate of the $O_2^-$• from gas phase to solution by plasma treatment and the consumption rate of $O_2^-$• and HOO•, respectively. Because $V_s$ is constant at any pH, the fraction of HOO• concentration at each pH value can be described using the following equation, derived from equation (5).

$$[HOO\bullet]/[HOO\bullet]_{pH\,=\,1} = (9.2 \times 10^2) \times (k_1 \times 10^{(pH-4.8)} + k_2 + k_3 \times 10^{2(pH-4.8)})^{-1/2} \quad (6)$$

Consequently, using equations (1) and (6), the fraction of $O_2^-$• concentration at each pH can be written as below.

$$[O_2^-\bullet]/[HOO\bullet]_{pH=1} = 9.2 \times 10^2 \times 10^{(pH-4.8)} \times (k_1 \times 10^{(pH-4.8)} + k_2 + k_3 \times 10^{2(pH-4.8)})^{-1/2} \quad (7)$$

The corresponding rate curve for equations (6) and (7) was plotted in Figure 2.1.3; the obtained curve was in good agreement with the results of the previous paper for spectrophotometric analysis of spontaneous disproportionation of radicals [42]. Therefore, the result indicates that the

concentration of HOO• and $O_2^{-}$• can be arbitrarily controlled by the pH of the solution.

## Bacterial inactivation

If Figure 1 describes the mechanism of plasma sterilization, the bacterial inactivation rate should be proportional to the concentration of HOO• in solution. Here, we investigated the inactivation of 3 kinds of bacteria at various pH values. The efficiency of bacterial inactivation was evaluated using the decimal reduction value (D value), which refers to the time required to inactivate 90% of bacteria in a given sample. The reciprocal of the D value is also the death rate of the bacteria, which implies the sterilizing power.

The death rate of bacteria was examined at pH 3.7–6.5 for typical types of bacteria using 3

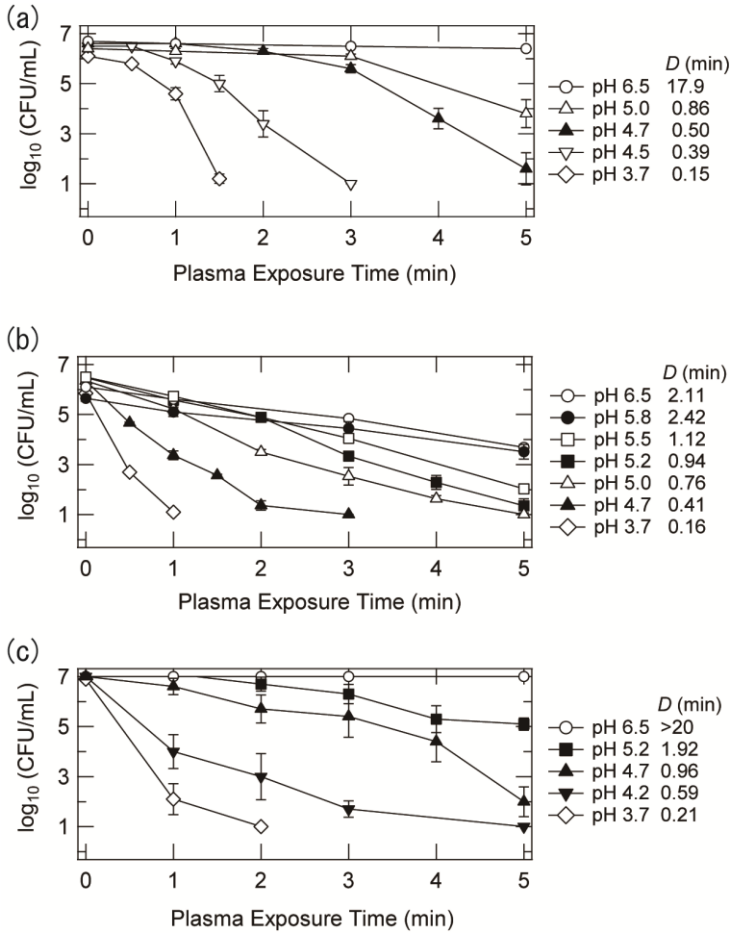


**Figure. 2.1.4.** Bacterial inactivation at various pH values as a function of plasma exposure time. Suspensions of (a) *S. mutans*, (b) *C. rectus*, and (c) *E. coli* were exposed to the plasma jet for 0–5 min. All data are obtained from triplicate experiments. The number of living cells after the plasma application was determined by a colony-forming unit (CFU) assay. The corresponding decimal reduction values (D values) are shown for each species of bacteria. The minimum detection value of the CFU assay was 10 CFU · $mL^{-1}$.

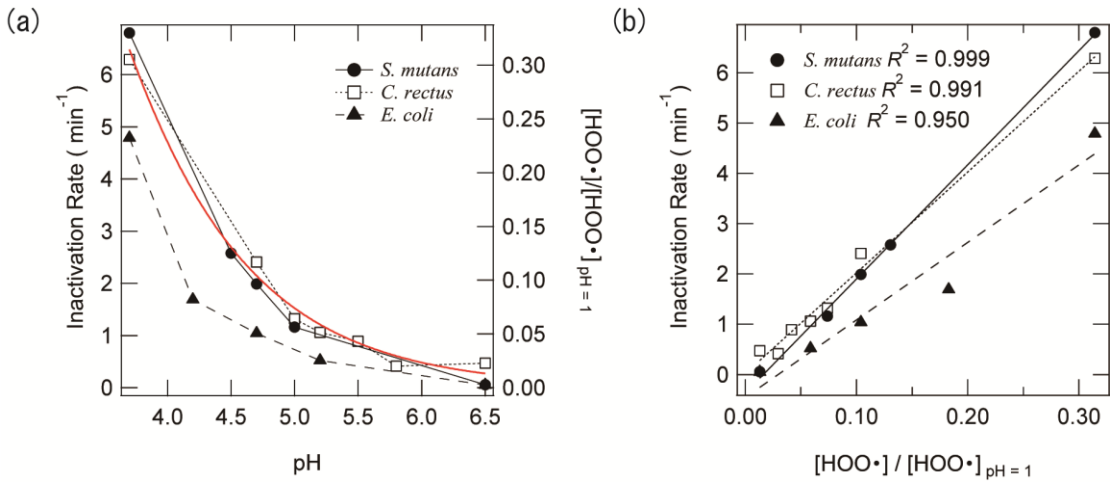


**Figure. 2.1.5.** Assessment of the bacterial inactivation. (a) Bacterial inactivation rate (reciprocal of the D value) for plasma treatment at various pH values. The inactivation rates were calculated from each corresponding D value. The red line (with respect to the right axis) indicates the relative concentration of HOO• in the pH range of 3.7–6.5. The HOO• concentration is expressed by equation (6). (b) Correlation between the inactivation rate of *S. mutans*, *C. rectus*, and *E. coli* and the HOO• concentration.

different species: *S. mutans*, a gram-positive acid-resistant bacterium causing human dental caries [43], *C. rectus*, a gram-negative anaerobic bacterium causing periodontal diseases [44], and *E. coli*, a gram-negative facultative anaerobic bacterium. These bacteria were not sterilized by the treatment in acid solution for several hours. *Pseudomonas aeruginosa*, which is an opportunistic human pathogen, was not used because of its high sensitivity to acidic solution. Although *S. mutans* was partially inactivated by the plasma treatment of a target solution at pH 6.5 for 5 min, the inactivation rate increased as the pH decreased from 5.0 to 3.7 (Fig. 2.1.4a). The D values of *S. mutans* obtained at pH values of 6.5, 5.0, 4.7, 4.5, and 3.7 were 17.9, 0.86, 0.50, 0.39, and 0.15 min, respectively (Fig. 2.1.4a). *C. rectus* was inactivated slowly at pH 6.5, and the inactivation rate increased with decreasing pH (Fig. 2.1.4b). The D values of *C. rectus* obtained at pH values of 6.5, 5.8, 5.5, 5.2, 5.0, 4.7, and 3.7 were 2.1, 2.4, 1.1, 0.94, 0.76, 0.41, and 0.16 min, respectively. *E. coli* was not inactivated at pH 6.5 after an interval of 5 min; however, the inactivation rate gradually increased with decreasing pH (Fig. 2.1.4c). In the case of *E. coli*, the D values obtained were 1.9, 0.96, 0.59, and 0.21 min at pH values of 5.2, 4.7, 4.2, and 3.7, respectively. The deactivation curves of *E. coli* at pH 7 using Na-phosphate buffer was obtained similar date at pH 6.5. It is noteworthy that the lag time for the curve of *S. mutans* before inactivation was greater than that for *C. rectus* or *E. coli*. This lag may be because the bacteria's tolerance to oxidative stress depends on the bacterial species.

The inactivation curves of *S. mutans*, C. *rectus*, and *E. coli* were consistent with the theoretical calculation of HOO• concentration (Fig. 2.1.5a). As shown in Figure 2.1.5a, the

inactivation rates of all bacteria decreased with increasing pH values. Figure 2.1.5b shows the inactivation rates of 3 bacteria as a function of HOO• concentration. As expected, the bacterial inactivation rates increased with an increasing concentration of HOO•, which is in consistent with the basic principle of microbiology that bacterial inactivation is proportional to the concentration of the bactericidal factor [40]. It should be noted that the difference in the slopes in Figure 2.1.5b resulted from differences in sensitivity to the radicals; the correlation coefficients were 0.999, 0.991, and 0.950 for *S. mutans*, *C. rectus*, and *E. coli*, respectively. This result indicates that the plasma sterilization of bacteria can be attributed to the presence of HOO•.

## Decoloration of surfactant micelles

We further investigated the relationship between radical species and bacterial inactivation. A simple bacterial model was constructed using a surfactant and a hydrophobic dye (Fig. 2.1.6a). This dye-included micelle was used for the cell membrane model that cannot be permeated by the $O_2^-$• charged radical, but can be permeated by the non-charged (neutral) HOO• radical. After penetration, the radicals react with the dye in the core of the micelle and result in decoloration, indicating the plasma effect for the bacterial model.

The dye-included micelle was constructed using a surfactant and a hydrophobic dye (Fig. 2.1.6a). The Nile red hydrophobic dye is known to have high stability against UV irradiation, acidic conditions, and heat treatment [45-48]. For example, Nile red is not affected by UV irradiation, acidic conditions, or heat from LTAPP. Nile red is also insoluble in aqueous solution owing to its hydrophobic property [49] (Fig. 2.1.6a). Tween 20 is an amphipathic surfactant with a hydrophilic

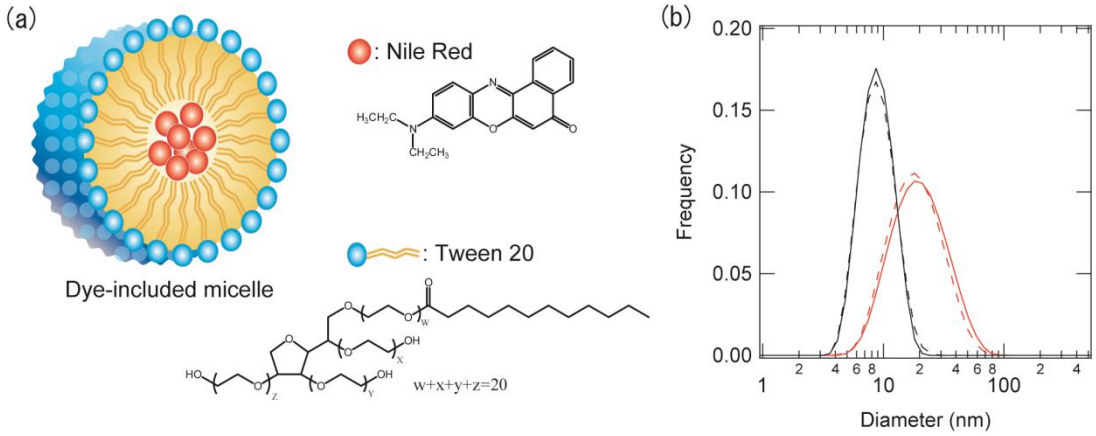


**Figure. 2.1.6.** Dye-included micelle. (a) Schematic representation of the dye-included micelle. The legends and chemical structures of Nile red and Tween 20 are shown. (b) Particle size distribution of the 1% v/v Tween 20 micelle was prepared without (black line) or with (red line) Nile red after 0 (solid line) and 20 (broken line) min of plasma exposure time, as monitored by dynamic light scattering.

head and hydrophobic tail (Fig. 2.1.6a), and it forms a spherical structure in an aqueous solution. The hydrophobic region of the micelle has permselectivity equivalent to that of a cell membrane. Moreover, unlike live bacterial cells, the surfactant micelle does not undergo metabolic reactions or show homeostatic responses to pH changes. Radical penetration into surfactant micelles leads to decoloration of Nile red, thereby resulting in a decrease in the absorbance of the solution at 552 nm. In fact, the use of a system involving the decoloration of a dye has previously been reported for quantitative analyses for plasma treatment [50-52]. Thus, a surfactant micelle consisting of a Nile red core is an appropriate model to validate that the key factor in bacterial sterilization is the permeability of radicals into the bacterial membrane.

The size and homogeneity of the dye-included micelles were characterized by dynamic light scattering (Fig. 2.1.6b). The hydrodynamic diameter of the micelle with Tween 20 alone was 9.3 nm, whereas that of the dye-included micelles was 20.6 nm. It is noted that these hydrodynamic diameters of the micelles with/without dye did not change during plasma application for 20 min. These results suggest that dye-included nondestructive micelles are suitable as a model of the cytoplasm and biomembrane to evaluate the chemical effects of atmospheric-pressure plasma in solution.

The decoloration of the dye-included micelles over a pH range of 1.0–11.0 was measured after plasma treatment. Figure 2.1.7a shows representative photographs of the samples at pH 2.0 and pH 10.0. The samples at pH 2 were decolorized after plasma treatment for 20 min, whereas those at pH 10.0 were only partly decolorized even after 20 min. Control experiments that included the use of helium flow only, UV irradiation, and hydrogen peroxide did not cause decoloration of the dye-included micelles (data not shown). The monitoring of the absorbance of the target solution at 552 nm, which corresponds to the maximum absorbance of Nile red, yielded a quantitative evaluation of the decoloration of the dye-included micelle by plasma. At pH 2.0, the dye-included micelle was decolorized rapidly in the interval of 0–10 min. At pH values of 4.0–10.0, the rates of decoloration of the dye-included micelles decreased as the pH increased. The longer duration of plasma treatment for the decoloration of the included dye than that for the sterilization of bacterium shown in Figure 2.1.4 may result from the detection sensitivity of the radical reaction. The curves in Figure 2.1.7b were fit to the following equation:

$$F = F_0 \exp(-at) \qquad (7)$$

Where $F$ denotes the fraction of the dye-included micelles, $F_0$ denotes the fraction of dye-included micelles at 0 min, $t$ represents the time of plasma application, and $a$ denotes the rate constant of decoloration.

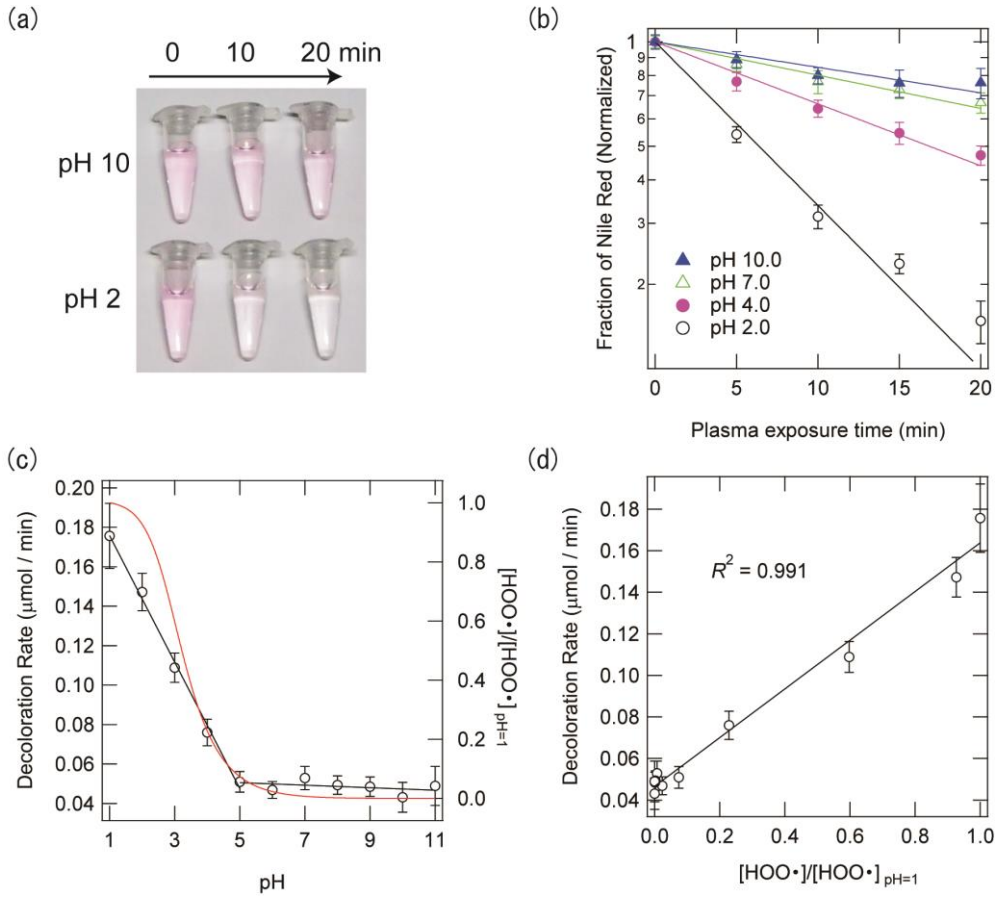


**Figure. 2.1.7.** Decoloration in dye-included micelles. (a) Photograph of the sample solution for pH values of 2.0 and 10.0 after plasma application for the indicated times. (b) Fraction of residual Nile red calculated from the absorbance at 552 nm after plasma application to the solution at pH values of 2.0, 4.0, 7.0, and 10.0. The absorbance values at 552 nm along the vertical axis are normalized. Error bars are based on the results of triplicate experiments. The decrease in the absorbance is fitted to equation (7). (c) Decoloration rate ($a_{t = 0\text{-}5}$) after plasma application for various pH values of the Nile red solution (indicated by open circles with respect to the left axis). Error bars are based on the results of triplicate experiments. The red line (with respect to the right axis) indicates the relative concentration of HOO• for the pH range of 1.0–11.0. The HOO• concentration is described by equation (6). (d) Assessment of decoloration in dye-included micelles. A correlation was shown between the decoloration rate and HOO• concentration.

The decoloration rate ($a_{t = 0\text{-}5}$) for the pH range of 1.0–11.0 is shown in Figure 2.1.7c. The decoloration rate ($a_{t = 0\text{-}5}$) was calculated from the data for intervals of 0 and 5 min of plasma application as an approximation of the rate constant of decoloration to avoid the influence of solution evaporation with long plasma treatment times. The decoloration rates of the dye-included micelles at pH 1.0–4.0 increased with decreasing pH, whereas they remained constant for the pH range of 5.0–11.0. The experimental results show that the decoloration rate of dye-included micelles subject to plasma treatment increases under acidic conditions, in a manner similar to the bacterial

inactivation rates shown in Figures 2.1.4 and 2.1.5. The boundary region between pH values of 4.0 and 5.0 showed good agreement with that described in a previous study reporting that plasma application inactivates bacteria effectively at pH levels below 4.8 [8]. Figure 7d shows the theoretical calculation curve of HOO• concentration (eq. 6). It is significant that the decoloration rates strongly correlate with the concentration of HOO• for the pH range of 1.0–11.0. Figure 6d shows the correlation between the decoloration rate and the amount of HOO• for a correlation coefficient of 0.991. This result indicates that decoloration in surfactant micelles can also be attributed to the presence of HOO•; the different permeability of radicals into the cell membrane is a key factor in plasma sterilization in solution.

# Discussion

## Molecular mechanism of bacterial sterilization

In this study, we demonstrated the mechanism of bacterial sterilization by using plasma-induced chemical processing with the reduced pH method, as illustrated in Figure 2.1.1. Molecular mechanisms of plasma sterilization achieved using the reduced pH method are discussed below. We can assume that bacterial sterilization results from $O_2^-$• and/or HOO• in solution, which are generated by LTAPP. As shown in Figure 2.1.3, comparison of pH-dependence on the concentration of $O_2^-$•, HOO•, and (HOO• + $O_2^-$•) revealed that the profile of only HOO• was similar to that of the inactivation rates for the 3 bacteria tested (Fig. 2.1.5a). Furthermore, the concentration of HOO• correlated well with all the inactivation rates of all bacteria (Fig. 2.1.5b). These results indicate that HOO• predominantly contributes to the plasma sterilization achieved using the reduced pH method.

These data raise the question as to why HOO• rather than $O_2^-$• plays a key role in plasma sterilization achieved using the reduced pH method. It is known that charged substances possess a low level of permeability across the cell membrane. Indeed, it has reported that $O_2^-$• has an electric charge of -1, which hinders its ability to permeate the cell membrane [53]. On the other hand, HOO• is not charged, which allows it to easily cross the cell membrane. Therefore, bacterial sterilization by radicals may depend on differences in permeability into the biomembrane.

To more clearly define the relationship between bacterial sterilization and permeability of radicals into the biomembrane, we constructed the dye-included micelle bacterial model (Fig. 2.1.6a). The decoloration system using dye-included micelles allowed us to detect only the chemical reactions of radicals in the micelle. Consequently, clear results were obtained; pH-dependence of the decoloration rate was similar to that of the concentration of HOO• (Fig. 2.1.7c), and the

concentration of HOO• was well correlated with the decoloration rates (Fig. 2.1.7d). Taken together, we successfully demonstrated that plasma sterilization achieved using the reduced pH method results only from HOO• due to its permeability into the biomembrane. We have reported that plasma treatment induced inactivation of protein in solution, although the protein was dispersed in the solution, and it did not remain in the micelle or cell membrane [39]. Furthermore, we have showed that the sterilization of bacteria by the plasma was not related the visible destruction of bacteria [8]. Thus, we concluded that the mechanism of sterilization using the reduced pH method is as follows: (Step 1) penetration of HOO• into the cell (Fig. 1); (Step 2) penetrated radicals react with and inactivate proteins in the cell; and (Step 3) sterilization is induced by inactivation of protein/s that are important for bacteria. We will try the challenge to control experiment using the radical species generated by other means but treatment of acidic solution with the jet in future.

## Assay of plasma sterilization

Several assays for plasma sterilization have been reported by other researchers, such as number of surviving CFUs plotted against dissipated power [27]. However, it is well known that bacterial inactivation is proportional to the concentration of the bactericidal factor [40]. This study shows a new assessment for plasma sterilization (Fig. 5b, 7d). It is of interest that a different gradient was found for each bacterium, which results from the different sensitivity of the bacteria to plasma treatment in solution. This result indicates that the gradient shows the sterilizing power of the plasma system for each bacterium. Consequently, the assay of plasma sterilization in solution is appropriate to plot the death rate of bacterial inactivation with the concentration of key species. In the feature, it is expected to elucidate the various situation of sterilization under medical applications by determination and quantitative measurement of other possible radicals which may cause similar effects.

Various plasma systems have been reported for sterilization [54, 55] and medicines [56], although these systems have not assessed the relationship between plasma treatment and radical behavior. Among them, our dye-included micelle successfully evaluated bacterial inactivation, which has simple components of abundant detergent and Nile red, which is known to have high stability against UV irradiation, acidic conditions, and heat treatment. Thus, we propose that the dye-included micelle system can be widely used as an assay of plasma systems for plasma sterilization in solution.

## Contribution to plasma medicines

We believe that our research contributes to plasma medicine. The inactivation rates of all bacteria tested increased with a decreasing pH (Fig. 2.1.5). Other researchers have also reported that plasma treatment effectively sterilizes bacteria under acidic conditions. For example, *S. aureus* was

effectively inactivated at pH 3.7–4.5 compared to pH 4.5–7.5 [57], *Bacillus subtilis* spores were inactivated only in acidic solution [58], and the eukaryotic microbe, *Neurospora crassa*, showed a rapid decrease in spore germination in acidic water [59]. Thus, we conclude that plasma treatment generally effectively sterilizes bacteria under acidic conditions.

We assume that the sterilization in solution by using plasma-induced chemical processing may be applicable to plasma medicine. However, human lymph and blood are at neutral pH with a buffering capacity. Therefore, the reduced pH method is necessary for the plasma sterilization. Actually, plasma treatment for 5 min had no effect at pH 6.5 but sterilized S. mutans, which is a model oral microorganism in dental plaques in biofilms at pH 4.5 [30]. Thus, the reduced pH method may be applicable to plasma medicine, such as for burn injury and bedsore.

There has been a growing interest in plasma medicine for its application in removing cancer cells [60]. For example, the permeability of radicals into the biomembrane can be controlled by pore formation by using Magainin 2 peptide [61], and the electroporation of cell membranes can be accomplished using electric pulses [62]. The combination of modifying cell membranes and using atmospheric-pressure plasma [63, 64] can increase the efficiency of plasma therapy for cancerous tumors by increasing the permeability of radicals into the membranes of cancer cells. Although it has been proposed that plasma treatment is toxic because of the generation of neutral reactive species, instead of ozone [65], the controversy is solved by our data. Our results can significantly contribute toward an increasingly efficient and safer application of plasma sterilization for medicinal purposes. The effective permeation of radicals into the cell membrane implies the possibility of using plasma therapy for the removal of cancer cells.

# Conclusion

In this study, we demonstrated the mechanism of efficient bactericidal inactivation with the reduced pH method illustrated in Figure 1, by using 3 kinds of living bacteria and a simple bacterial model. Our data showed that the death rate of the bacteria tested was proportional to the concentration of hydroperoxy radicals in the solution (Fig. 2.1.5b and 2.1.7d). These results indicate that the key species for the plasma sterilization with the reduced pH method is hydroperoxy radicals, and its key role is to bring about high permeation of radicals into the cell membrane in order to achieve efficient bactericidal activity of plasma treatment in solution. Our data contribute to the development of not only plasma sterilization but also plasma medicine.

# References


[1] Bruggeman P, Iza F, Lauwers D and Gonzalvo Y A 2010 Mass spectrometry study of positive and negative ions in a capacitively coupled atmospheric pressure RF excited glow discharge in He-water mixtures *J. Phys. D: Appl. Phys.* **43** 012003

[2] Locke B R, Sato M, Sunka P, Hoffmann M R and Chang J S 2006 Electrohydraulic discharge and nonthermal plasma for water treatment *Ind. Eng. Chem. Res.* **45** 882-905

[3] Sahni M and Locke B R 2006 The effects of reaction conditions on liquid-phase hydroxyl radical production in gas-liquid pulsed-electrical-discharge reactors *Plasma Process. Polym.* **3** 668-81

[4] Sahni M and Locke B R 2006 Quantification of hydroxyl radicals produced in aqueous phase pulsed electrical discharge reactors *Ind. Eng. Chem. Res.* **45** 5819-25

[5] Bruggeman P and Leys C 2009 Non-thermal plasmas in and in contact with liquids *J. Phys. D: Appl. Phys.* **42** 012003

[6] Burlica R, Shih K Y and Locke B R 2010 Formation of H-2 and H2O2 in a Water-Spray Gliding Arc Nonthermal Plasma Reactor *Ind. Eng. Chem. Res.* **49** 6342-9

[7] Tani A, Ono Y, Fukui S, Ikawa S and Kitano K 2012 Free radicals induced in aqueous solution by non-contact atmospheric-pressure cold plasma *Appl. Phys. Lett.* **100** 254103

[8] Ikawa S, Kitano K and Hamaguchi S 2010 Effects of pH on bacterial inactivation in aqueous solutions due to low-temperature atmospheric pressure plasma application *Plasma Process. Polym.* **7** 33-42

[9] Liu D X, Rong M Z, Wang X H, Iza F, Kong M G and Bruggeman P 2010 Main species and physicochemical processes in cold atmospheric-pressure He + O-2 plasmas *Plasma Process. Polym.* **7** 846-65

[10] Furusho H, Miyamoto D, Nagasaki Y, Kitano K and Hamaguchi S 2007 Synthesis of uniformly dispersed metal nanoparticles with dispersion stability by nonequilibrium atmospheric plasma jets *J. Photopolym. Sci. Technol.* **20** 229-33

[11] Furusho H, Kitano K, Hamaguchi S and Nagasaki Y 2009 Preparation of stable water-dispersible PEGylated gold nanoparticles assisted by nonequilibrium atmospheric-pressure plasma jets *Chem. Mater.* **21** 3526-35

[12] Sumitani S, Murotani H, Oishi M, Kitano K, Hamaguchi S and Nagasaki Y 2009 Nonequilibrium atmospheric plasma jets assisted stabilization of drug delivery carriers: Preparation and characterization of biodegradable polymeric nano-micelles with Enhanced Stability *J. Photopolym. Sci. Technol.* **22** 467-71

[13] Kong M G, Kroesen G, Morfill G, Nosenko T, Shimizu T, van Dijk J and Zimmermann J L 2009 Plasma medicine: an introductory review *New J. Phys.* **11** 115012

[14] Babaeva N Y and Kushner M J 2013 Reactive fluxes delivered by dielectric barrier discharge filaments to slightly wounded skin *J. Phys. D: Appl. Phys.* **46** 025401

[15] Sato T, Yokoyama M and Johkura K 2011 A key inactivation factor of HeLa cell viability by a plasma flow *J. Phys. D: Appl. Phys.* **44** 372001

[16] Kim K, Choi J D, Hong Y C, Kim G, Noh E J, Lee J-S and Yang S S 2011 Atmospheric-pressure plasma-jet from micronozzle array and its biological effects on living cells for cancer therapy *Appl. Phys. Lett.* **98** 073701

[17] Kim S J, Chung T H, Bae S H and Leem S H 2010 Induction of apoptosis in human breast cancer cells by a pulsed atmospheric pressure plasma jet *Appl. Phys. Lett.* **97** 023702

[18] Kim C H, Kwon S, Bahn J H, Lee K, Jun S I, Rack P D and Baek S J 2010 Effects of atmospheric nonthermal plasma on invasion of colorectal cancer cells *Appl. Phys. Lett.* **96** 243701

[19] Karakas E, Munyanyi A, Greene L and Laroussi M 2010 Destruction of alpha-synuclein based amyloid fibrils by a low temperature plasma jet *Appl. Phys. Lett.* **97** 143702

[20] Fridman G, Peddinghaus M, Balasubramanian M, Ayan H, Fridman A, Gutsol A and Brooks A 2006 Blood coagulation and living tissue sterilization by floating-electrode dielectric barrier discharge in air *Plasma Chem. Plasma Process.* **26** 425-42

[21] Gweon B, Kim D, Kim D B, Jung H, Choe W and Shin J H 2010 Plasma effects on subcellular structures *Appl. Phys. Lett.* **96** 101501

[22] Feng H Q, Wang R X, Sun P, Wu H Y, Liu Q, Fang J, Zhu W D, Li F T and Zhang J 2010 A study of eukaryotic response mechanisms to atmospheric pressure cold plasma by using Saccharomyces cerevisiae single gene mutants *Appl. Phys. Lett.* **97** 131501

[23] Bussiahn R, Brandenburg R, Gerling T, Kindel E, Lange H, Lembke N, Weltmann K D, von Woedtke T and Kocher T 2010 The hairline plasma: An intermittent negative dc-corona discharge at atmospheric pressure for plasma medical applications *Appl. Phys. Lett.* **96** 143701

[24] Perni S, Shama G, Hobman J L, Lund P A, Kershaw C J, Hidalgo-Arroyo G A, Penn C W, Deng X T, Walsh J L and Kong M G 2007 Probing bactericidal mechanisms induced by cold atmospheric plasmas with Escherichia coli mutants *Appl. Phys. Lett.* **90** 073902

[25] Kolb J F, Mohamed A A H, Price R O, Swanson R J, Bowman A, Chiavarini R L, Stacey M and Schoenbach K H 2008 Cold atmospheric pressure air plasma jet for medical applications *Appl. Phys. Lett.* **92** 241501

[26] Zhang X H, Huang J, Liu X D, Peng L, Guo L H, Lv G H, Chen W, Feng K C and Yang S Z 2009 Treatment of Streptococcus mutans bacteria by a plasma needle *J. Appl. Phys.* **105** 063302

[27] Majumdar A, Singh R K, Palm G J and Hippler R 2009 Dielectric barrier discharge plasma treatment on E. coli: Influence of CH4/N-2, O-2, N-2/O-2, N-2, and Ar gases *J. Appl. Phys.* **106** 084701

[28] Lu X, Ye T, Cao Y G, Sun Z Y, Xiong Q, Tang Z Y, Xiong Z L, Hu J, Jiang Z H and Pan Y 2008 The roles of the various plasma agents in the inactivation of bacteria *J. Appl. Phys.* **104** 053309

[29] Burlica R, Grim R G, Shih K Y, Balkwill D and Locke B R 2010 Bacteria inactivation using low power pulsed gliding arc discharges with water spray *Plasma Process. Polym.* **7** 640-9

[30] Yamazaki H, Ohshima T, Tsubota Y, Yamaguchi H, Jayawardena J A and Nishimura Y 2011 Microbicidal activities of low frequency atmospheric pressure plasma jets on oral pathogens *Dent. Mater. J.* **30** 384-91

[31] K. Kitano S I, A. Tani, T. Ohshima, H. Yamaguchi, H. Yamazaki, R. Arakawa, T. Kitamura, and N. Ohnishi,

Innovative plasma disinfection of bacteria in water by the reduced pH method combined with free radicals supplied by non-contact atmospheric plasma *in Proceedings of the 20th International Symposium on Plasma Chemistry (ISPC-20), Philadelphia, USA, 24–29 July 2011, p. 17.*

[32] Tani A, Ono Y, Fukui S, Ikawa S and Kitano K 2012 Free radicals induced in aqueous solution by non-contact atmospheric-pressure cold plasma *Appl. Phys. Lett.* **100** 254103

[33] Bielski B H J, Cabelli D E, Arudi R L and Ross A B 1985 Reactivity of Ho2/O-2 radicals in aqueous-solution *J. Phys. Chem. Ref. Data* **14** 1041-100

[34] D. Behar G C, J. Rabani, Leon M. Dorfman, Harold A. Schwarz 1970 Acid dissociation constant and decay kinetics of the perhydroxyl radical *J. Phys. Chem.* **74** 3209-13

[35] Li G, Li H P, Wang L Y, Wang S, Zhao H X, Sun W T, Xing X H and Bao C Y 2008 Genetic effects of radio-frequency, atmospheric-pressure glow discharges with helium *Appl. Phys. Lett.* **92** 221504

[36] Yan X, Zou F, Lu X P, He G Y, Shi M J, Xiong Q, Gao X, Xiong Z L, Li Y, Ma F Y, Yu M, Wang C D, Wang Y S and Yang G X 2009 Effect of the atmospheric pressure nonequilibrium plasmas on the conformational changes of plasmid DNA *Appl. Phys. Lett.* **95** 083702

[37] Kurita H, Nakajima T, Yasuda H, Takashima K, Mizuno A, Wilson J I B and Cunningham S 2011 Single-molecule measurement of strand breaks on large DNA induced by atmospheric pressure plasma jet *Appl. Phys. Lett.* **99** 191504

[38] Yasuda H, Miura T, Kurita H, Takashima K and Mizuno A 2010 Biological evaluation of DNA damage in bacteriophages inactivated by atmospheric pressure cold plasma *Plasma Process. Polym.* **7** 301-8

[39] Takai E, Kitano K, Kuwabara J and Shiraki K 2012 Protein inactivation by low-temperature atmospheric pressure plasma in aqueous solution *Plasma Process. Polym.* **9** 77-82

[40] Deindoerfer F H 1957 Microbiological process discussion; calculation of heat sterilization times for fermentation media *Appl. Microbiol.* **5** 221-8

[41] Kim A Y and Thayer D W 1995 Radiation-induced cell lethality of Salmonella-Typhimurium Atcc-14028 - Cooperative Effect of Hydroxyl Radical and Oxygen *Radiat. Res.* **144** 36-42

[42] Marklund S 1976 Spectrophotometric study of spontaneous disproportionation of superoxide anion radical and sensitive direct assay for superoxide-dismutase *J. Biol. Chem.* **251** 7504-7

[43] Loesche W J 1986 Role of Streptococcus mutans in human dental decay *Microbiol. Rev.* **50** 353-80

[44] Rams T E, Feik D and Slots J 1993 Campylobacter-Rectus in human periodontitis *Oral Microbiol. Immunol.* **8** 230-5

[45] Mishra R, Sjolander D and Hammarstrom P 2011 Spectroscopic characterization of diverse amyloid fibrils in vitro by the fluorescent dye Nile red *Mol. BioSyst.* **7** 1232-40

[46] Greenspan P and Fowler S D 1985 Spectrofluorometric studies of the lipid probe, Nile Red *J. Lipid Res.* **26** 781-9

[47] Greenspan P, Mayer E P and Fowler S D 1985 Nile Red - a selective fluorescent stain for intracellular lipid

droplets *J. Cell Biol.* **100** 965-73

[48] Cser A, Nagy K and Biczok L 2002 Fluorescence lifetime of Nile Red as a probe for the hydrogen bonding strength with its microenvironment *Chem. Phys. Lett.* **360** 473-8

[49] Krishna M M G 1999 Excited-state kinetics of the hydrophobic probe Nile red in membranes and micelles *J. Phys. Chem. A* **103** 3589-95

[50] Wang Z, Xu D, Chen Y, Hao C and Zhang X 2008 Plasma decoloration of dye using dielectric barrier discharges with earthed spraying water electrodes *J. Electrostatics* **66** 476-81

[51] Chen G, Zhou M, Chen S and Chen W 2009 The different effects of oxygen and air DBD plasma byproducts on the degradation of methyl violet 5BN *J. Hazard. Mater.* **172** 786-91

[52] Kuwahata H, Kimura K and Ohyama R-i 2010 Decolorization of methylene blue aqueous solution by atmospheric-pressure plasma jet *e-J. Surf. Sci. Nanotech.* **8** 381-3

[53] Korshunov S S and Imlay J A 2002 A potential role for periplasmic superoxide dismutase in blocking the penetration of external superoxide into the cytosol of Gram-negative bacteria *Mol. Microbiol.* **43** 95-106

[54] Bussiahn R, Brandenburg R, Gerling T, Kindel E, Lange H, Lembke N, Weltmann K D, von Woedtke T and Kocher T 2010 The hairline plasma: An intermittent negative dc-corona discharge at atmospheric pressure for plasma medical applications *Appl. Phys. Lett.* **96** 143701

[55] Lu X, Ye T, Cao Y, Sun Z, Xiong Q, Tang Z, Xiong Z, Hu J, Jiang Z and Pan Y 2008 The roles of the various plasma agents in the inactivation of bacteria *J. Appl. Phys.* **104** 053309

[56] Kong M G, Kroesen G, Morfill G, Nosenko T, Shimizu T, van Dijk J and Zimmermann J L 2009 Plasma medicine: an introductory review *New J. Phys.* **11** 115012

[57] Liu F X, Sun P, Bai N, Tian Y, Zhou H X, Wei S C, Zhou Y H, Zhang J, Zhu W D, Becker K and Fang J 2010 Inactivation of bacteria in an aqueous environment by a direct-current, cold-atmospheric-pressure air plasma microjet *Plasma Process. Polym.* **7** 231-6

[58] Sun P, Wu H Y, Bai N, Zhou H X, Wang R X, Feng H Q, Zhu W D, Zhang J and Fang J 2012 Inactivation of Bacillus subtilis spores in water by a direct-current, cold atmospheric-pressure air plasma microjet *Plasma Process. Polym.* **9** 157-64

[59] Park G, Ryu Y H, Hong Y J, Choi E H and Uhm H S 2012 Cellular and molecular responses of Neurospora crassa to non-thermal plasma at atmospheric pressure *Appl. Phys. Lett.* **100** 063703

[60] Huang J, Chen W, Li H, Wang X Q, Lv G H, Khosa M L, Guo M, Feng K C, Wang P Y and Yang S Z 2011 Deactivation of A549 cancer cells in vitro by a dielectric barrier discharge plasma needle *J. Appl. Phys.* **109** 053305

[61] Tamba Y and Yamazaki M 2009 Magainin 2-induced pore formation in the lipid membranes depends on its concentration in the membrane iInterface *J. Phys. Chem. B* **113** 4846-52

[62] Tsong T Y 1991 Electroporation of cell-membranes *Biophys. J.* **60** 297-306

[63] Srivastava N and Wang C 2011 Effects of water addition on OH radical generation and plasma properties in an atmospheric argon microwave plasma jet *J. Appl. Phys.* **110** 053304

[64] Sousa J S, Niemi K, Cox L J, Algwari Q T, Gans T and O'Connell D 2011 Cold atmospheric pressure plasma jets as sources of singlet delta oxygen for biomedical applications *J. Appl. Phys.* **109** 123302

[65] Kalghatgi S, Fridman A, Azizkhan-Clifford J and Friedman G 2012 DNA Damage in mammalian cells by non-thermal atmospheric pressure microsecond pulsed dielectric barrier discharge plasma is not mediated by ozone *Plasma Process. Polym.* **9** 726-32

## 2.2 Effects of alkyl chain length of gallate on self-association and membrane-binding

# Introduction

Gallate is a general term used to describe salts and esters of gallic acid with the galloyl group. Some gallate compounds, typically catechin and proanthocyanidin gallates, have been developed for pharmacological applications [1–7]. Among them, alkyl gallates have recently been regarded as affecting microbial cell viability [8–18], virus activity [19–25], and human leukemia cell proliferation [26]. The alkyl gallates' pharmacological activity increases concomitantly with their alkyl chain length. Therefore their activity has been attributed to their surfactant-like effects, which can induce lipid membrane disruption and membrane protein inactivation [11–13]. In fact, alkyl gallates have both a hydrophilic galloyl group and hydrophobic alkyl chain. More hydrophobic species with longer alkyl chains, e.g. dodecyl gallate [8,9] and stearyl gallate [10,11], do not function as antibacterial agents, suggesting an unknown factor that determines the cutoff point for activity [9].

Fluorescence spectra have been used often for analyses of interactions of various aromatic compounds with lipid membranes because fluorescence spectra depend greatly on the solution environment [27]. For example, membrane binding of peptides and low-molecular-weight compounds has been observed through changes in fluorescence intensity [28–34]. Furthermore, fluorescence analyses present the advantage of being quantitative. For that reason, the thermodynamic parameters of the interactions, such as partition constants, can be determined. The membrane binding affinity for catechin derivatives has been measured to investigate their pharmacological activities [35].

Although partition constants of alkyl gallates with lipid membranes might be related to their pharmacological activity, partition constants have not been examined aside from qualitative observations [36]. This study revealed that the partition constant depends on the alkyl chain length of gallate. The constant of the alkyl gallates increased concomitantly with increasing hydrophobicity, except for longer alkyl chain species such as cetyl and stearyl gallates. These two alkyl gallates are exceptional probably because of their self-association detected by dynamic light scattering measurements. Moreover, the membrane-binding of alkyl gallates was found to be correlated with the pharmacological activity of a series of alkyl gallates. Consequently, our findings are useful for

understanding not only the physicochemical properties of alkyl gallates, but also for elucidating their pharmacological activity.

# Materials and methods

## Chemicals

All alkyl gallates were obtained from Tokyo Kasei Kogyo Co. Ltd. (Tokyo, Japan). Dioleoylphosphatidylcholine (DOPC), dipalmitoylphosphatidylcholine (DPPC), dioleoylphosphatidylglycerol (DOPG), and cholesterol were obtained from NOF Corp. (Tokyo, Japan) along with sodium dihydrogen phosphate (Nacalai Tesque Inc., Kyoto, Japan) and ethanol (Kanto Chemical Co. Inc., Tokyo, Japan). All compounds were of the highest commercially available grade.

## Solubility measurement of alkyl gallates

The respective solubilities of alkyl gallates in 10 mM phosphate buffer (pH 7.4) were measured as follows [38]. An appropriate amount of alkyl gallate powder was transferred into a test tube, to which 1.5 ml of 10 mM phosphate buffer (pH 7.4) was added. The suspension was heated at 40 °C for 1 h with frequent vortexing for complete dissolution of alkyl gallate powders. The solution was then incubated at 25 °C for 3 days with frequent vortexing. Subsequently, the suspension was centrifuged at 25 °C and 16,000 × g for 20 min to obtain a supernatant saturated with the alkyl gallates. After appropriate dilution of the supernatant with water, the supernatant absorbance was determined spectrophotometrically at 271 nm using a UV–VIS spectrophotometer (ND-1000; NanoDrop Technologies, Inc.., Wilmington, DE, USA). The absorbance value was converted to the concentration based on the standard curve determined for methyl gallate. Solubility was determined in triplicate, from which the averages and standard errors were obtained.

## Observation of self-association of alkyl gallates

To verify the self-association of the alkyl gallates, dynamic light scattering (DLS) measurements of them at 3 μM were conducted at 25 °C using a light-scattering spectrometer (DLS-7000; Ostuka Electronics Co., Ltd. Osaka, Japan) equipped with an argon ion laser at scattering angles of 90° [46]. Samples that did not pass the instrument's internal quality criteria were omitted.

## Preparation of lipid membranes

Large unilamellar vesicles (LUV) composed of DOPC, DOPG, DPPC, and cholesterol (Chol) were

used as model lipid membranes, prepared using the extrusion method with 200 nm pore size polycarbonate membranes. The appropriate amounts of 5 mM lipids were mixed in chloroform. Subsequently, the solvent was removed completely in a vacuum desiccator connected to a rotary vacuum pump for 12 h. To this dry lipid film, 1 ml of 10 mM phosphate buffer (pH 7.4) was added; then the 1.5 mM lipid suspension was vortexed for several seconds above the phase-transition temperature (25 °C for DOPC and DOPG, and 40 °C for DPPC). Subsequently, the solutions were extruded through 200-nm-pore-size polycarbonate membranes (Avanti Mini-Extruder; Avanti Polar Lipids, Inc., Alabaster, AL) at a temperature higher than the phase-transition temperature.

### Fluorescence analysis of the binding of alkyl gallates to phospholipid membranes

Fluorescence spectra of 3 μM alkyl gallate in 10 μM lipids with 10 mM phosphate buffer (pH 7.4) were recorded at 25 °C. Only for **C8**–**18** were they presolubilized in ethanol before mixing with the lipid solution to determine the alkyl gallate concentration. Thereby, the final component of the solution was 3 μM alkyl gallate, 10 μM lipids, 0.6% ethanol, and 10 mM phosphate buffer (pH 7.4), where the residual ethanol did not affect their fluorescence spectra. Finally, the fluorescence intensity of each reference solution without the alkyl gallate was subtracted from the intensity of the sample solutions. The determined intensities were averages of triplicate experiments. Thereby, the average and standard error were obtained. These spectra were measured using a spectrofluorometer (FP6500; Jasco Corp., Tokyo, Japan). The emission fluorescence spectra were recorded for 200–500 nm, using the excitation wavelength of 271 nm.

### Measurement of the partition constant of alkyl gallates to the membranes

To determine the partition constant of the alkyl gallates (**C8**–**C16**) to the membranes, the changes in fluorescence intensity of the alkyl gallate on the membrane-binding were monitored using a spectrofluorometer. The prepared sample solutions contained various concentrations of the lipids comprising DOPC, DPPC/DOPC or DPPC/Chol, 60 nM alkyl gallates, 0.6% ethanol, and 10 mM phosphate buffer (pH 7.4). The fluorescence intensity of each reference solution without the alkyl gallates was subtracted from the intensity of the sample solutions. The determined intensities were averages of triplicate experiments: the average and standard error were obtained.

# Results

## Solubility and hydrodynamic radius of alkyl gallates

The alkyl gallates used for this study are shown in Scheme 2.2.1, where they are termed **C1–C18** according to the carbon number of the alkyl chain. The solubility of the alkyl gallates in 10 mM phosphate buffer solution was measured for physicochemical characterization of the alkyl gallates. As shown in Table 2.2.1, the solubility of **C2** is higher than that of **C1**, which is consistent with our previous study [37, 38]. The solubility of **C12** is lower than that of **C16**, which is not surprising when considering the dynamic light scattering measurements as follows. Results show that **C16** and **C18** tend to self-associate in the solution (Fig. 2.2.1). The solutions of **C16** and **C18** respectively exhibit a unimodal size distribution with mean diameters of 84.6 ± 4.6 nm and 130.6 ± 17.6 nm. In contrast, **C8** and **C12** were not detected using the same apparatus. It can be concluded that the self-association of **C16** and **C18** increases their apparent solubilities.

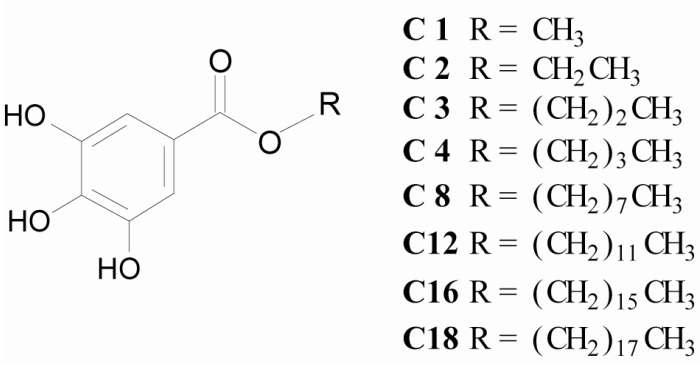


**Scheme 1.** Chemical structures of the alkyl gallates.

**Table 2.2.1.** Solubility of the alkyl gallates in 10 mM phosphate buffer (pH 7.4) at 25 °C

| Gallate | Solubility (M) |
|---|---|
| Metyl (**C1**) | $6.46 \pm 0.11\times10^{-2}$ |
| Ethyl (**C2**) | $8.19 \pm 0.05\times10^{-2}$ |
| Propyl (**C3**) | $1.92 \pm 0.01\times10^{-2}$ |
| Butyl (**C4**) | $1.21 \pm 0.02\times10^{-2}$ |
| Octyl (**C8**) | $5.7 \pm 0.6\times10^{-4}$ |
| Dodecyl (**C12**) | $6.4 \pm 0.8\times10^{-5}$ |
| Cetyl (**C16**) | $9.1 \pm 0.7\times10^{-5}$ |
| Stearyl (**C18**) | $3.9 \pm 0.7\times10^{-5}$ |

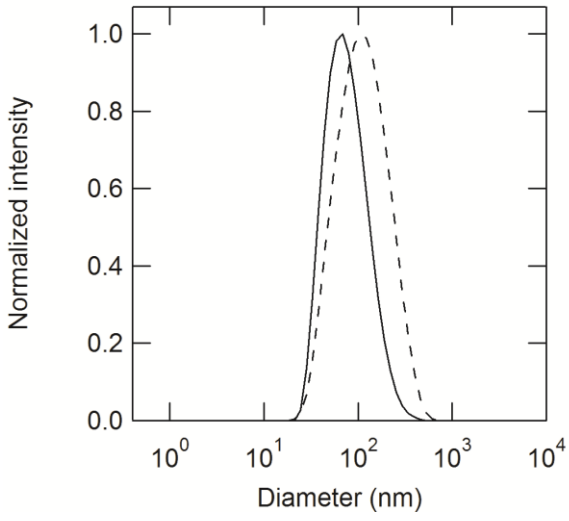


**Figure 2.2.1.** DLS measurements for 3 μM cetyl gallate (**C16**) (solid line) and stearyl gallate (**C18**) (broken line) in water.

## Binding of alkyl gallates to phospholipid membranes

Binding of the alkyl gallates to the membranes was observed through the change of fluorescent intensities of their aromatic moiety. Figure 2.2.2 presents fluorescence spectra of **C4** in the presence or absence of DOPG or DOPC. As expected, the fluorescence spectrum of **C4** differed in the presence of positively charged DOPG or amphoteric DOPC. Accordingly, results suggest that the binding of **C4** to the membranes is mainly attributable to the hydrophobic interaction between DOPC and the alkyl chains of the alkyl gallates. Similar data were obtained for **C1**, **C2**, and **C3**. To support

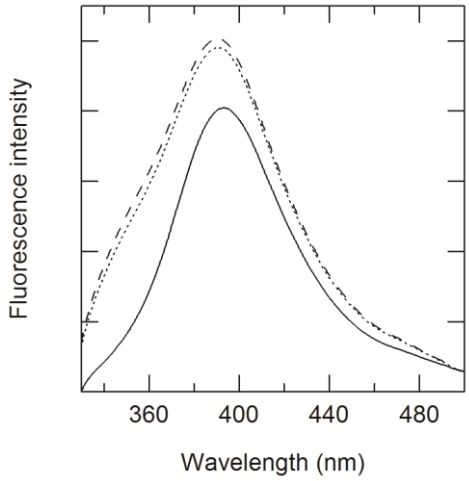


**Figure 2.2.2.** Fluorescence spectra of 3 μM butyl gallate (**C4**) in the presence and absence of 10 μM DOPC or DOPG: no lipid, solid line; DOPC, broken line; DOPG, dotted line. The excitation wavelength of the fluorescence spectra is 271 nm.

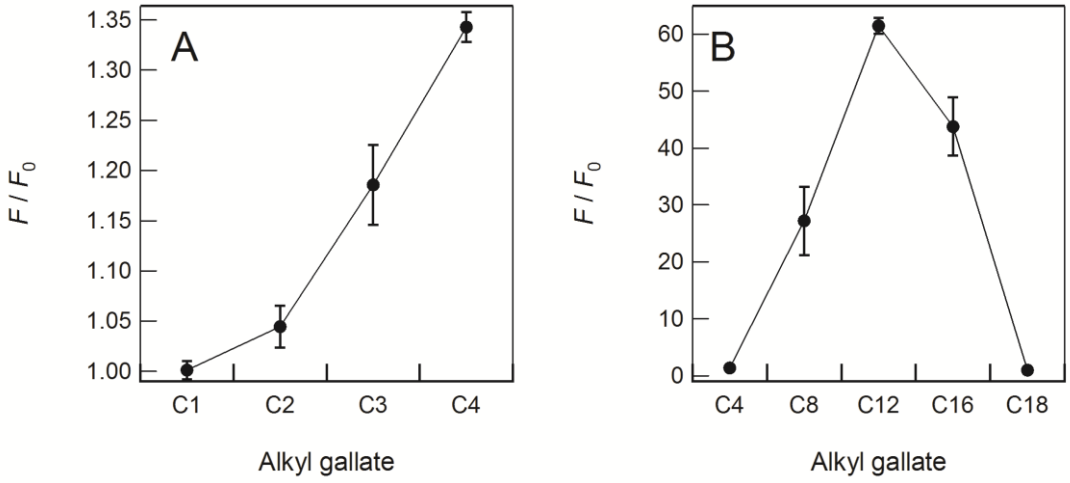


**Figure 2.2.3.** Ratios of the fluorescence intensity of the respective 3 μM alkyl gallates (A) **C1–C4** and (B) **C4–C18** in the presence of 10 μM DOPC to those in the buffer solution.

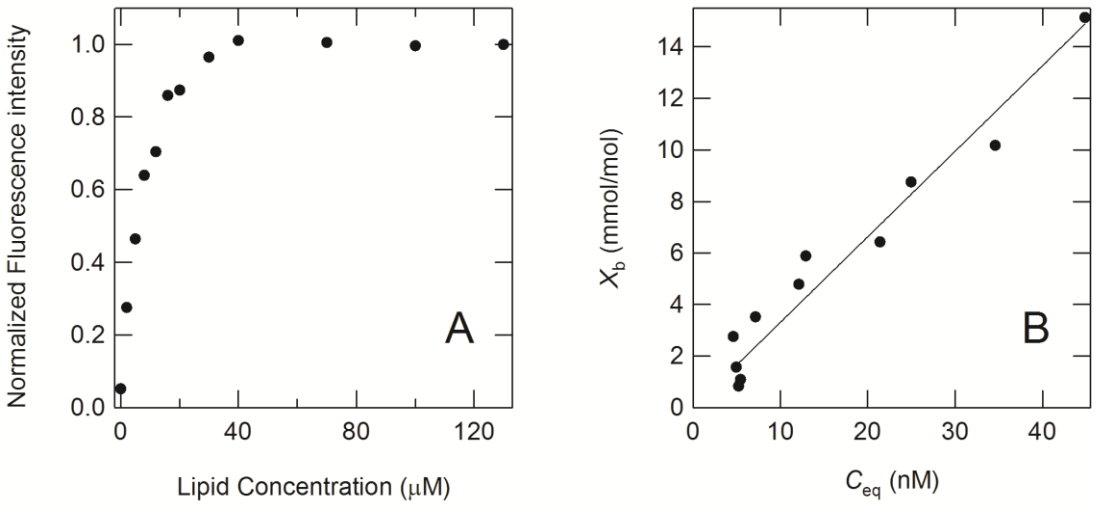


**Figure 2.2.4.** (A) Normalized fluorescent intensity of 60 nM octyl gallate (**C8**) at 350 nm in various concentrations of DOPC, normalized by the maximum value. (B) Binding isotherms of octyl gallate (**C8**) to the lipid membrane of DOPC at 25 ℃.

the suggestion presented above, we investigated the dependence of the alkyl chain length of the binding to DOPC. Ratios of the fluorescence intensity in the presence of DOPC to that in the absence of DOPC increased with elongation of the alkyl chain length (Fig. 2.2.3A). The ratios for **C1**–**C12** increased with the alkyl chain length (Fig. 2.2.3). The changes in fluorescence intensities of their aromatic moiety are caused by the polarity of the solution environment [31]. In contrast, the fluorescence intensity of **C16**, despite its longer alkyl chain, was weaker than that of **C12**. Additionally, the intensity of **C18** did not change according to the presence of the lipid membrane.

## Estimation of the partition constant of alkyl gallates to phospholipid membranes

Partition constants of the alkyl gallates to the membranes were estimated from the binding isotherms as follows. Figure 2.2.4A shows representative data for the peak intensity of the fluorescence spectra of **C8** in various concentrations of DOPC, as normalized by the maximum value. The normalized intensity in Fig. 2.2.4A increased by the addition of DOPC and subsequently reached a plateau at which all **C8** molecules bind to the membrane. Here, a two-state transition was presumed: binding or non-binding states of the alkyl gallates to the membrane. Additionally, it was assumed that the alkyl gallates bind to both the internal and external monolayer. Consequently, the equilibrium concentration of the alkyl gallate in the bulk solutions, as denoted by $C_{eq}$, was obtained as [28]

$$C_{eq} = C_T - C_M = C_T(1 - F_N), \quad (1)$$

**Table 2.2.2.** Intrinsic partition constant ($K_{int}$) of octyl (**C8**), dodecyl (**C12**) and cetyl (**C16**) gallates to the lipid membrane of DOPC

| Gallate | $K_{int}$ (1/M) |
|---|---|
| Octyl (**C8**) | $1.5 \pm 0.1 \times 10^5$ |
| Dodecyl (**C12**) | $8.2 \pm 0.7 \times 10^5$ |
| Cetyl (**C16**) | $8.4 \pm 0.6 \times 10^5$ |

where $C_T$ and $C_M$ respectively denote the total concentration of the alkyl gallate in solution and its concentration in the lipid membranes. Therein, $F_N$ denotes the normalized fluorescence intensity corresponding to the vertical axis in Fig. 2.2.4A. The molar ratio of the alkyl gallate molecules in the membranes to total lipid molecules, denoted by $X_b$, is given as

$$X_b = C_T F_N / C_L , \quad (2)$$

where $C_L$ is the lipid concentration in solution. Finally, because the ratio of the concentration of the alkyl gallate to that of the lipid membrane in the solution is low, $X_b$ can be expressed as [29]

$$X_b = K_{int} C_{eq} , \quad (3)$$

where $K_{int}$ is the intrinsic partition constant of the alkyl gallate to the lipid membrane. According to these analyses, $X_b$ and $C_{eq}$ are actually mutually proportional (Fig. 2.2.4B). These calculations are applicable to the other alkyl gallates, except for **C1**–**C4** and **C18**: because of their weak binding affinity to the membrane, their binding curves were not obtained. The partition constants for **C8**, **C12** and **C16** are presented in Table 2.2.2; the partition constants for **C12** and **C16** were of the same order and an order of magnitude higher than that for **C8**. These results reflect that the partition constant for **C16** might be affected by self-association of **C16**, as described above (Fig. 2.2.1).

## Effect of membrane components on the binding of alkyl gallate to phospholipid membranes

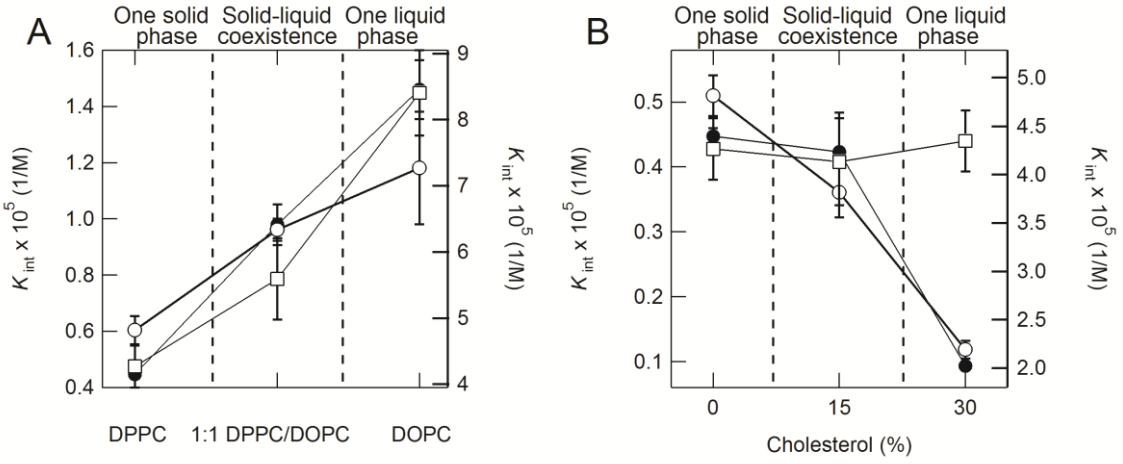


**Figure 2.2.5.** Binding constants ($K_{int}$) of 60 nM octyl gallate (**C8**) (closed circles, left axes), dodecyl gallate (**C12)** (open circles, right axes) and cetyl gallate (**C16**) (open squares, right axes) in the presence of DPPC/DOPC (A) and DPPC/Chol (B).

The membrane liquid–solid phase differs according to its components [39]. They can be expected to affect the binding affinity of the alkyl gallates. Figure 2.2.5A exhibits the partition constants for **C8**, **C12**, and **C16** to the lipid membranes composed of various ratios of DPPC/DOPC. The partition constants for these alkyl gallates increased concomitantly with the increasing ratio of DOPC to DPPC; the value for DOPC was twice that for DPPC. Figure 2.2.5B shows alteration of the partition constants for these alkyl gallates to the membranes containing cholesterol. The partition constants for **C8** and **C12** decreased concomitantly with increasing concentration of cholesterol, although that for **C16** was maintained.

# Discussion

Alkyl gallates are anticipated for use as antibacterial and antiviral agents because various studies have already shown their pharmacological activity in vitro [8–25]. Therefore, their biophysical properties should be clarified in advance of their application. Nevertheless, quantitative studies such as thermodynamic studies of the binding interaction of the alkyl gallates to lipid membranes have not been reported. Additionally, it has not been established why highly hydrophobic alkyl gallates with a longer alkyl chain did not function as antibacterial agents [8–11]. Regarding the binding interaction of the alkyl gallates to lipid membranes, only qualitative observations have been performed [36]. In this study, we quantitatively examined the binding ability of alkyl gallates with different alkyl chain lengths to various lipid membranes. It is worth mentioning that this is the first report of a partition

**Table 2.2.3.** Calculated correlation coefficients between ratios of the fluorescence intensity ($F/F_0$) and the pharmacological activity of the alkyl gallates against bacteria and viruses

| Targets | $r$[a] | Ref. |
|---|---|---|
| *Propionibacterium acnes* | 0.949 | [13] |
| *Brevibacterium ammoniagenes* | 0.892 | [13] |
| *Staphylococcus aureus (MRSA)* | 0.892 | [13] |
| *Micrococcus luteus* | 0.824 | [13] |
| *Bacillus subtilis* | 0.824 | [13] |
| *Streptococcus mutans* | 0.593 | [13] |
| *Trichophyton mentagrophytes* | 0.409 | [16] |
| *Trichophyton rubrum* | 0.135 | [16] |
| *Microsporum gypseum* | 0.129 | [16] |
| Targets | $r$[b] | Ref |
| *Herpes simplex virus type-1* | 0.745 | [19] |
| *Lenzites betulina* | 0.785 | [14] |
| *Gloeophyllum trabeum* | 0.729 | [14] |
| *Chaetomium globosum* | 0.716 | [14] |
| *Trametes versicolor* | 0.683 | [14] |

[a]: Correlation coefficients between ratios of the fluorescence intensity ($F/F_0$) determined in this paper and antibacterial activities of the alkyl gallates (log(1/MIC)), where MIC is the minimum inhibitory concentration, as described in reports of previous studies [13,16]. [b]: Correlation coefficients between $F/F_0$ and the yield of antiviral effects [19] and antifungal fractions [14]. The calculated correlation coefficients are the Pearson product-moment correlation coefficients [45].

constant between the alkyl gallates and phospholipid membrane. Ratios of fluorescence intensity of **C1**–**C12** have increased concomitantly with increasing alkyl chain length (Fig. 2.2.3). The ratios for **C1**–**C12** increased with the logarithm of the octanol–water partition coefficient (log *P*) of the alkyl gallates. Therefore, it was suggested that the membrane-binding ability of **C1**–**C12** depends on their hydrophobicity derived from the alkyl chain. However, for more hydrophobic species with a longer alkyl chain (**C16**, **C18**), the intensity decreased. Here, recall that DLS measurements for **C8**–**C18** indicated self-association of **C16** and **C18**, even at concentrations below solubility (Fig. 2.2.1, Table 2.2.1). Assuming that the self-associated forms have no ability to interact with the lipid membrane, the observed reduction of the membrane-binding ability for **C16** and **C18** can be ascribed to the promotion of self-association with increasing alkyl chain length. The result, that **C16** but not **C18**

interacted with the membranes (Fig. 2.2.3B), presents the possibility that the self-association state of **C16** is an equilibrium, with the soluble monomeric state binding to the lipid membranes.

Reportedly, antibacterial and antiviral activities of the alkyl gallates decrease as their alkyl chain length increases beyond a certain length [8–11], indicating a cutoff point for the activity of the alkyl gallates [9]. Reduction of the activity will be reasonable according to our observations. The reduction can be attributed to the promotion of the self-association with increasing alkyl chain length. In other words, such self-associated species cannot interact with the bacterial cell membranes or envelopes of viruses. Therefore, their activities would be reduced. Consequently, the pharmacological activity of the alkyl gallates can be expected to be associated closely with their physicochemical properties such as hydrophobicity and the monomeric solubility. To assess the relation between the physicochemical properties and the pharmacological activity, we investigated the correlation between the membrane binding ability and pharmacological activity (Table 2.2.3), where the binding ability was evaluated using the ratios of the fluorescence intensity of the alkyl gallates ($F/F_0$). Most correlation coefficients were positive and greater than 0.7. Therefore, the membrane-binding ability of the alkyl gallates will probably account for the results obtained for the pharmacological activity. It is noteworthy that the correlation coefficients for *Trichophyton rubrum* and *Microsporum gypseum* were lower than the others. Consequently, the pharmacological activity of the alkyl gallates might be partly accounted for by other functions including disruption of lipid membranes, inactivation of membrane proteins and their downstream activities.

The alkyl gallate‘s interaction with cholesterol and with phospholipids also constitutes important information. Lipid membranes composed of DPPC, DOPC, and cholesterol are often used as cell membrane models with phase changes depending on the composition ratio [39–44]. The results presented in Fig. 2.2.5 indicate that the alkyl gallates are more stable in the liquid phase of DPPC/DOPC than in the solid phase, although they are less stable in the liquid phase of DPPC/Chol than in the solid phase. Consequently, the stability of alkyl gallates in lipid membranes depends substantially on the membrane components rather than the membrane phase. The direct interaction of the alkyl gallates with the lipid components might be related with various pharmacological effects toward bacterial cells [12,14] and viruses [19,21].

Finally, the stability of the alkyl gallate in aqueous solution depends on the co-existing solutes, as shown in our previous study [37,38]. Alteration of the stability in the solution by the solutes can affect the partition constants and thereby affect their activity toward bacterial cells and viruses. Such effects of solutes are potentially applicable to prevent self-association and to enhance their bioavailability as drugs and food additives. We are carrying out systematic investigations of the solute effects to elucidate their potential benefits.

# References


[1] Kuo, P.L., Hsu, Y.L., Lin, T.C., Lin, C.C. (2005) The antiproliferative activity of prodelphinidin B-2 3'-O-gallate from green tea leaf is through cell cycle arrest and Fas-mediated apoptotic pathway in A549 cells. *Food. Chem. Toxicol.* **43**,315-323.

[2] Ahmad, N., Feyes, D.K., Nieminen, A.L., Agarwal, R., Mukhtar, H. (1997) Green tea constituent epigallocatechin-3-gallate and induction of apoptosis and cell cycle arrest in human carcinoma cells *J. Natl. Cancer Inst.* 89,1881-1886.

[3] Tsukiyama, F., Nakai, Y., Yoshida, M., Tokuhara, T., Hirota, K., Sakai, A., Hayashi, H., Katsumata, T. (2006) Gallate, the component of HIF-inducing catechins, inhibits HIF prolyl hydroxylase. *Biochem. Biophys. Res. Commun.* **351**,234-239.

[4] Fang, M.Z., Wang, Y.M., Ai, N., Hou, Z., Sun, Y., Lu, H., Welsh, W., Yang, C.S. (2003) Tea polyphenol (-)-epigallocatechin-3-gallate inhibits DNA methyltransferase and reactivates methylation-silenced genes in cancer cell lines *Cancer Res.* **63**, 7563-7570.

[5] Lin, Y.L., Lin, J.K. (1997) (-)-epigallocatechin-3-gallate blocks the induction of nitric oxide synthase by down-regulating lipopolysaccharide-induced activity of transcription factor nuclear factor-kappa B *Molecular Pharmacology* **52**,465-472.

[6] Yokoyama, M., Noguchi, M., Nakao, Y., Pater, A., Iwasaka, T. (2004) The tea polyphenol, (-)-epigallocatechin gallate effects on growth, apoptosis, and telomerase activity in cervical cell lines *Gynecologic Oncology* **92**,197-204.

[7] Kubo, I., Xiao, P., Nihei, K., Fujita, K., Yamagiwa, Y., Kamikawa, T. (2002) Molecular design of antifungal agents. *J. Agric. Food. Chem*. **50**,3992-3998.

[8] Fujita, K., Kubo, I. (2002) Antifungal activity of octyl gallate International Journal of Food Microbiology 79,193-201.

[9] Fujita, K., Kubo, I. (2002) Plasma membrane injury induced by nonyl gallate in Saccharomyces cerevisiae *Journal of Applied Microbiology* **92**,1035-1042.

[10] Leal, P.C., Mascarello, A., Derita, M., Zuljan, F., Nunes, R.J., Zacchino, S., Yunes, R.A. (2009) Relation between lipophilicity of alkyl gallates and antifungal activity against yeasts and filamentous fungi. Bioorg. *Med. Chem. Lett.* **19**,1793-1796.

[11] Hsu, F.L., Chen, P.S., Chang, H.T., Chang, S.T. (2009) Effects of alkyl chain length of gallates on their antifungal property and potency as an environmentally benign preservative against wood-decay fungi *International Biodeterioration and Biodegradation* **63**,543-547.

[12] Kubo, I., Xiao, P., Fujita, K. (2001) Antifungal activity of octyl gallate, Structural criteria and mode of action

*Bioorganic & Medicinal Chemistry Letters* **11**,347-350.

[13] Kubo, I., Fujita, K., Nihei, K. (2003) Molecular design of multifunctional antibacterial agents against methicillin resistant Staphylococcus aureus (MRSA) *Bioorganic & Medicinal Chemistry* **11**,4255-4262.

[14] Strippoli, V., D'Auria, F.D., Tecca, M., Callari, A., Simonetti, G. (2000) Propyl gallate increases in vitro antifungal imidazole activity against Candida albicans *International Journal of Antimicrobial Agents* **16**,73-76.

[15] Nihei, K., Nihei, A., Kubo, I. (2003) Rational design of antimicrobial agents, Antifungal activity of alk(en)yl dihydroxybenzoates and dihydroxyphenyl alkanoates *Bioorganic & Medicinal Chemistry Letters* **13**,3993-3996.

[16] Hsu, F.L., Chang, H.T., Chang, S.T. (2007) Evaluation of antifungal properties of octyl gallate and its synergy with cinnamaldehyde. *Bioresour. Technol.* **98**,734-738.

[17] Kubo, I., Fujita, K., Nihei, K., Nihei, A. (2004) Antibacterial activity of akyl gallates against Bacillus subtilis. *J. Agric. Food. Chem.* **52**,1072-1076.

[18] Sierra-Campos, E., Valdez-Solana, M.A., Matuz-Mares, D., Velazquez, I., Pardo, J.P. (2009) Induction of morphological changes in Ustilago maydis cells by octyl gallate *Microbiology* **155**,604-611.

[19] Uozaki, M., Yamasaki, H., Katsuyama, Y., Higuchi, M., Higuti, T., Koyama, A.H. (2007) Antiviral effect of octyl gallate against DNA and RNA viruses. *Antiviral. Res.* **73**,85-91.

[20] Hurtado, C., Bustos, M.J., Sabina, P., Nogal, M.L., Granja, A.G., Gonzalez, M.E., Gonzalez-Porque, P., Revilla, Y., Carracosa, A.L. (2008) Antiviral activity of lauryl gallate against animal viruses *Antiviral Therapy* **13**,909-917.

[21] Yamasaki, H., Uozaki, M., Katsuyama, Y., Utsunomiya, H., Arakawa, T., Higuchi, M., Higuti, T., Koyama, A.H. (2007) Antiviral effect of octyl gallate against influenza and other RNA viruses International *Journal of Molecular Medicine* **19**,685-688.

[22] C.J.M. Kane, J.H. Menna, C.-C. Sung, Y.-C., Yeh (1988) Methyl Gallate, Methyl-3,4,5-trihydoxybenzoate, is a Potent and Highly Specific Inhibitor of Herpes Simplex Virus in vitro. II. Antiviral Activity of Methyl Gallate and its Derivatives *Bioscience. Reports*, **8**, 1.

[23] Kratz, J.M., Andrighetti-Frohner, C.R., Kolling, D.J., Leal, P.C., Cirne-Santos, C.C., Yunes, R.A., Nunes, R.J., Trybala, E., Bergstrom, T., Frugulhetti, I.C., Barardi, C.R., Simoes, C.M. (2008) Anti-HSV-1 and anti-HIV-1 activity of gallic acid and pentyl gallate. *Mem. Inst. Oswaldo. Cruz.* **103**,437-442.

[24] Jadel Müller KRATZ, Carla Regina ANDRIGHETTI-FRÖHNER, Paulo César LEAL, Ricardo José NUNES, Rosendo Augusto YUNES, Edward TRYBALA, Tomas BERGSTRÖM, Célia Regina Monte BARARDI, and Cláudia Maria Oliveira SIMÕES (2008) Evaluation of Anti-HSV-2 Activity of Gallic Acid and Pentyl Gallate *Biol. Pharm. Bull*. **31**(5.). 903—907.

[25] Chavez, J.H., Leal, P.C., Yunes, R.A., Nunes, R.J., Barardi, C.R., Pinto, A.R., Simoes, C.M., Zanetti, C.R. (2006) Evaluation of antiviral activity of phenolic compounds and derivatives against rabies virus. *Vet. Microbiol*. **116**,53-59.

[26] Dodo, K., Minato, T., Noguchi-Yachide, T., Suganuma, M., Hashimoto, Y. (2008) Antiproliferative and

apoptosis-inducing activities of alkyl gallate and gallamide derivatives related to (-)-epigallocatechin gallate. *Bioorg. Med. Chem.* **16**, 7975-7982.

[27] Robert, W. Cowgill (1967) Fluorescence and protein structure, X. Reappraisal of solvent and structural effects *Biochimica et Biophysica Acta - Protein Structure* **133**, 6-18.

[28] Tamba, Y., Yamazaki, M. (2009) Magainin 2-induced pore formation in the lipid membranes depends on its concentration in the membrane interface. *J. Phys. Chem. B.* **113**, 4846-4852.

[29] Wieprecht, T., Apostolov, O., Beyermann, M., Seelig, J. (2000) Membrane binding and pore formation of the antibacterial peptide PGLa, thermodynamic and mechanistic aspects. *Biochemistry*. **39**,442-452.

[30] Lampio, A., Kilpelainen, I., Pesonen, S., Karhi, K., Auvinen, P., Somerharju, P., Kaariainen, L. (2000) Membrane binding mechanism of an RNA virus-capping enzyme. *J. Biol. Chem.* **275**, 37853-37859.

[31] Kraft, C.A., Garrido, J.L., Leiva-Vega, L., Romero, G. (2009) Quantitative analysis of protein-lipid interactions using tryptophan fluorescence. *Sci. Signal*. **2**,pl4.

[32] Witold, K. Surewicz, Richard, M. Epand (1984) Role of Peptide Structure in Lipid-Peptide Interactions, A Fluorescence Study of the Binding of Pentagastrin-Related Pentapeptides to Phospholipid Vesicles *Biochemistry* **23**, 6072-6077.

[33] Chaudhuri, S., Pahari, B., Sengupta, P.K. (2009) Ground and excited state proton transfer and antioxidant activity of 7-hydroxyflavone in model membranes, absorption and fluorescence spectroscopic studies. *Biophys. Chem.* **139**, 29-36.

[34] Klymchenko, A.S., Duportail, G., Ozturk, T., Pivovarenko, V.G., Mely, Y., Demchenko, A.P. (2002) Novel two-band ratiometric fluorescence probes with different location and orientation in phospholipid membranes *Chemistry & Biology* **9**,1199-1208.

[35] Kajiya, K., Hojo, H., Suzuki, M., Nanjo, F., Kumazawa, S., Nakayama, T. (2004) Relationship between antibacterial activity of (+)-catechin derivatives and their interaction with a model membrane. *J. Agric. Food. Chem.* **52**,1514-1519.

[36] Shibata, H., Nakano, T., Parvez, M.A., Furukawa, Y., Tomoishi, A., Niimi, S., Arakaki, N., Higuti, T. (2009) Triple combinations of lower and longer alkyl gallates and oxacillin improve antibiotic synergy against methicillin-resistant Staphylococcus aureus. *Antimicrob. Agents. Chemother.* **53**,2218-2220.

[37] Hirano, A., Kameda, T., Arakawa, T., Shiraki, K. (2010) Arginine-assisted solubilization system for drug substances, solubility experiment and simulation. *J. Phys. Chem. B.* **114**,13455-13462.

[38] Ariki, R., Hirano, A., Arakawa, T., Shiraki, K. (2011) Arginine increases the solubility of alkyl gallates through interaction with the aromatic ring. *J. Biochem.* **149** 389-394

[39] Veatch, S.L., Keller, S.L. (2003) Separation of liquid phases in giant vesicles of ternary mixtures of phospholipids and cholesterol *Biophysical Journal* **85**, 3074-3083.

[40] Veatch, S.L., Keller, S.L. (2002) Organization in lipid membranes containing cholesterol *Physical Review Letters* **89** 268101

[41] Veatch, S.L., Keller, S.L. (2005) Seeing spots, complex phase behavior in simple membranes. *Biochim. Biophys. Acta* **1746**,172-185.

[42] Veatch, S.L., Keller, S.L. (2005) Miscibility phase diagrams of giant vesicles containing sphingomyelin *Physical Review Letters* **94** 148101

[43] Cicuta, P., Keller, S.L., Veatch, S.L. (2007) Diffusion of liquid domains in lipid bilayer membranes. *J. Phys. Chem. B.* **111**, 3328-3331.

[44] Veatch, S.L., Soubias, O., Keller, S.L., Gawrisch, K. (2007) Critical fluctuations in domain-forming lipid mixtures. *Proc. Natl. Acad. Sci. USA* **104**, 17650-17655.

[45] Zou, K.H., Tuncali, K., Silverman, S.G. (2003) Correlation and simple linear regression. *Radiology* **227**, 617-622.

[46] Georgalis Y, Kierzek AM, Saenger W (2000) Cluster formation in aqueous electrolyte solutions observed by dynamic light scattering *J. Phys. Chem. B.* **104**,3405-3406

# Chapter 3

# Chemical Modification of Amino Acids

## 3.1 Chemical Modification of Amino Acids by Atmospheric-Pressure Cold Plasma in Aqueous Solution

# Introduction

Atmospheric-pressure cold plasma (APCP) has been used for various applications and has many advantages: (i) inexpensive operation costs in vacuum-free systems; (ii) use of a moderate gas temperature; (iii) facilitation of delicate and flexible operations; and (iv) generation of reactive oxygen species (ROS)[1], typically hydroxyl radicals (OH•)[2-6], superoxide anion radicals ($O_2^-$•)[7], hydroperoxy radicals (HOO•)[8], singlet oxygen ($^1O_2$), and atomic oxygen (O)[9]. These features of APCP enable the exploitation of a novel field of chemical reactions both in solution [10-12] and under dry conditions. Recent pioneering applications of APCP include ionisation for use in mass spectrometry[13, 14], elimination of organic materials[15], tooth bleaching[16], and plasma medicines [17-19] for cancer[20-24], glioma[25], dental applications[26], blood coagulation[27], disruption of the human hepatocyte cytoskeleton[28], sterilisation[29-38], Parkinson's disease[39], and Alzheimer's disease[40].

The mechanism of action of plasma medicine involving the chemical reactions that occur in solution with the ROS may proceed as follows: (Step 1) the ROS generated by APCP diffuses in solution (body fluid); (Step 2) the ROS reacts with and inactivates biologically functional biomolecules, such as proteins; (Step 3) this inactivation induces some medically relevant physiological response through cell death or activation. To elucidate the mechanism of action of plasma medicine, studies of the effect of APCP on biologically functional biomolecules, i.e., biomacromolecules, in aqueous solution are necessary. Atmospheric-pressure plasma destroys the tertiary structure of DNA[41, 42] and inactivates infectious prion protein[43], recombinant green fluorescent protein[44], and the enzyme lysozyme[45] in aqueous solution.

Proteins are the most abundant compound and are composed of 20 naturally occurring amino acids joined by peptide bonds. Proteins dominate biological functions in the body. We previously reported that APCP inactivates lysozyme in aqueous solution accompanied by a conformational change, bleaching of the intrinsic tryptophan fluorescence, and increased the molecular weight, indicating that the amino acid side chains of the protein were chemically modified

by APCP[45]. However, the details of the reaction of each amino acid during plasma application remain unclear. Hydroxylation of phenylalanine[46] and the formation of disulphide linkages between the thiol groups of cysteines[47, 48] by plasma treatment have been reported. The elucidation of the chemical reaction of each amino acid with the ROS generated by APCP would help establish the mechanism of action of plasma medicine, particularly Step 2.

In this study, we report the chemical modification of 20 amino acids in solution by low-frequency (LF) plasma jet, an APCP system. The side chains of 14 amino acids were oxidised and sulphur-containing and aromatic amino acids were preferentially modified in the amino acids. This paper provides fundamental data on the effects of plasma medicine on protein structure and function.

# Materials and methods

## Materials

Ultra-pure water was obtained from a Milli-Q SP TOC system water purifier (Millipore Corp., Bedford, Mass., USA). Acetonitrile was from Wako Pure Chemical Industries, Ltd. (Osaka, Japan). L-alanine (Ala), L-asparagine (Asn), L-aspartic acid (Asp), L-arginine hydrochloride (Arg), L-cysteine (Cys), L-glutamic acid (Glu), L-glutamine (Gln), glycine (Gly), L-histidine (His), L-isoleucine (Ile), L-leucine (Leu), L-lysine hydrochloride (Lys), L-methionine (Met), L-phenylalanine (Phe), L-proline (Pro), L-threonine (Thr), L-tryptophan (Trp), L-tyrosine (Tyr), L-serine (Ser), and L-valine (Val) were from Sigma-Aldrich Corp. (St. Louis, Mo., USA).

## System of low-frequency (LF) plasma jet

The LF plasma jet was used in a manner similar to that described previously[8, 37, 40, 45]. The experimental system comprising the plasma generator and amino acid solution in the vessel is shown in Fig. 3.1.1. The LF plasma jet was ejected from the end of a quartz glass tube in which helium (He) gas was flowed by the application of a high-voltage alternating current (AC) (from -3.5 kV to +5.0 kV with a frequency of 13.9 kHz) to the electrode, which was a small metal sheet wound around the tube. The He plasma with low gas temperature was generated as an elongated shape. The flow rate of the He gas was 2.0 l/min. The various ROS produced by the He plasma were supplied to the solution. A 1.0 ml sample of 1.0 mM amino acid solution was applied to the solution in the vessel. The distance between the end of the glass tube and the surface of the amino acid solution was 20 mm.

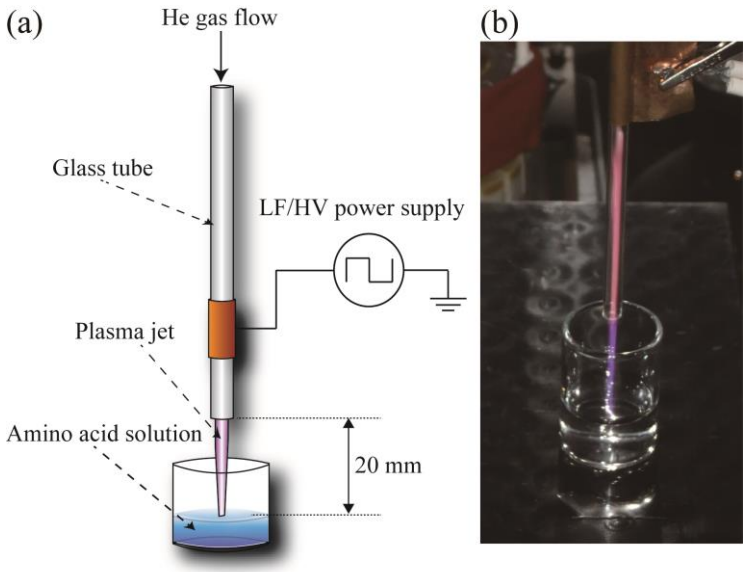


**Figure. 3.1.1.** Schematic diagram of the plasma generation system. (a) LF/HV pulses are applied to the electrode, which is wound around the glass tube. The distance between end of the quartz glass tube and surface of the amino acid solution is 20 mm. Plasma is generated in He gas flowing (2.0 l/min) in the glass tube. A plume-like structure of the plasma ('plasma jet') is extended toward the surface of a liquid. The discharge power of the plasma is 3 W. The volume of amino acid solution is 1 ml. (b) Photograph of the plasma jet.

## High-resolution mass spectrometry

Mass spectra were obtained in the electrospray ionisation (ESI) positive-ion mode using an Orbitrap mass spectrometer (Exactive, Thermo Fisher Scientific, CA). The ESI-MS operating conditions were as follows: electrospray potential 4.80 kV, capillary voltage 25 V, capillary temperature 250°C, tube lens voltage 140 V, skimmer voltage 38V, and m/z scan range 50–500. The plasma-exposed amino acid solutions were diluted with water (50-fold by volume) followed by acetonitrile (2-fold by volume), and the diluted solutions were electrosprayed at a flow rate of 30 µl/min.

## Amino acid analysis

The amino acid analysis was performed on an amino acid analyser (JLC-500/V2, Japan Electron Optics Laboratory). High-pressure liquid chromatography was performed on a cation ion-exchange column. The amino acids were detected by reaction with ninhydrin.

# Results and Discussion

## Plasma treatment of amino acids

The chemical modification of 20 naturally occurring amino acids by plasma treatment in aqueous solution was investigated by high-resolution mass spectrometry[49]. Table 3.1.1 summarises the results of the oxidation of 14 amino acids after the plasma treatment. No oxidation of Gly, Ala, Ser, Thr, Asn, and Asp was observed. The data were consistent with a previous report that the molecular weights of proteins are increased by plasma treatment[45] due to the oxidation of free radicals on the side chains of the amino acids[50]. These results indicate that electron-rich groups in amino acids were modified by the free radicals generated by the plasma treatment.

**Table 3.1.1.** Oxidation of 14 amino acids by plasma treatment.

| Amino acid | Side chain | [M+nO] | [M−nH] | [M+nO−H+N] | [2M−2H] | Amino acid | Side chain | [M+nO] | [M−nH] | [M+nO−H+N] | [2M−2H] |
|---|---|---|---|---|---|---|---|---|---|---|---|
| Tyr | 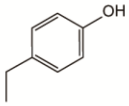 | ○ | | ○ | | Lys | 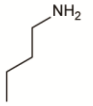 | ○ | ○ | | |
| Phe |  | ○ | | ○ | | Arg | 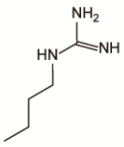 | ○ | ○ | | |
| Trp | 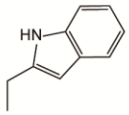 | ○ | | | | Gln | 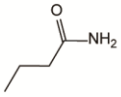 | ○ | | | |
| Cys |  | ○ | | | ○ | Glu | 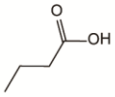 | ○ | | | |
| Met | 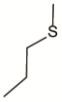 | ○ | | | | Val |  | ○ | ○ | ○ | |
| Pro | 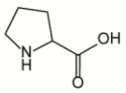 | ○ | | | | Leu |  | ○ | ○ | ○ | |
| His |  | ○ | | | | Ile |  | ○ | ○ | ○ | |

## Aromatic amino acids: Tyr, Phe, and Trp

Figure 3.1.2 shows the mass spectra of Tyr, Phe, and Trp after plasma treatment for 0-10 min. Before plasma treatment, $(Tyr)H^+$ of *m/z* 182.08 was detected in a solution of Tyr (Fig. 3.1.2a). After plasma treatment, four oxidation products corresponding to $(Tyr+O)H^+$ at *m/z* 198.08, $(Tyr+2O)H^+$ at *m/z* 214.07, $(Tyr-H+2O+N)H^+$ at *m/z* 227.07, and $(Tyr-H+3O+N)H^+$ at *m/z* 243.06 (Fig. 3.1.2b,c) were observed in the mass spectrum of Tyr. The aromatic ring of Tyr has been reported to be easily hydroxylated[50-53] and nitrated[54-56]. Thus, these oxidations likely occurred in the aromatic ring

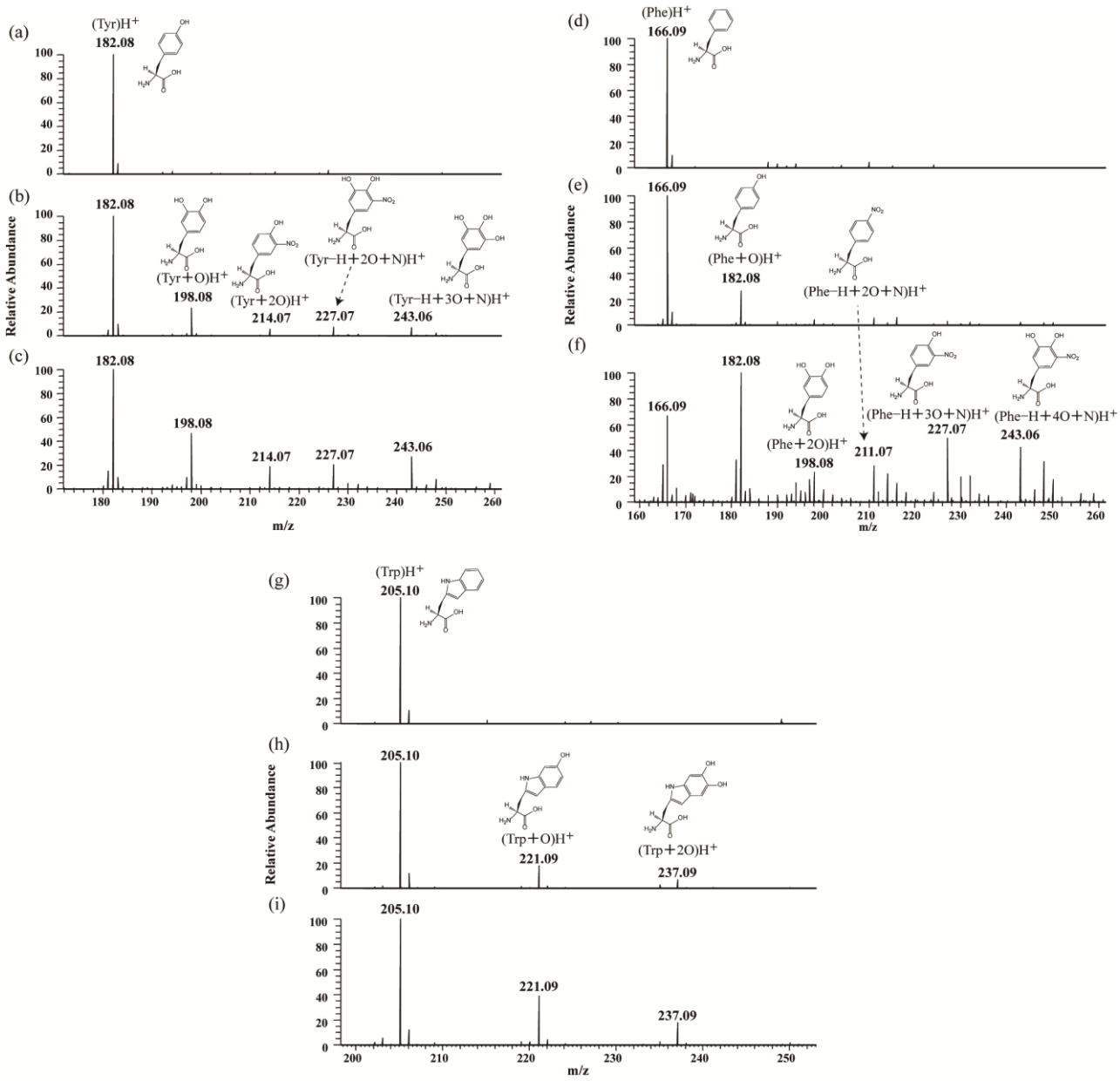


**Figure. 3.1.2.** Mass spectra of Tyr (a-c), Phe (d-f), and Trp (g-i) treated with plasma for 0 min (a,d,g), 5 min (b,e,h), and 10 min (c,f,i). A molecular structure of the proposed product is shown for each peak.

of Tyr and correspond to DOPA at *m/z* 198.08, hydroxyl DOPA at *m/z* 214.07, nitro Tyr at *m/z* 227.07, and nitro DOPA at *m/z* 243.06 (as shown in Fig. 3.1.2b).

$(Phe)H^+$ was detected at *m/z* 166.09 from a solution of Phe before the plasma treatment (Fig. 3.1.2d). After plasma treatment, the mass spectrum of Phe revealed five oxidation products corresponding to $(Phe+O)H^+$ at *m/z* 182.08, $(Phe+2O)H^+$ at *m/z* 198.08, $(Phe-H+2O+N)H^+$ at *m/z* 211.07, $(Phe-H+3O+N)H^+$ at *m/z* 227.07, and $(Phe-H+4O+N)H^+$ at *m/z* 243.06 (Fig. 3.1.2e,f). These products likely correspond to oxidation of the aromatic ring of Phe and $(Phe+O)H^+$ at *m/z* 182.08, likely due to Tyr. The peak intensity ratios $(Tyr+X)H^+/(Tyr)H^+$ and $(Phe+X)H^+/(Phe)H^+$ increased monotonously with increasing plasma treatment time. These results suggest that $(Tyr-H+3O+N)H^+$

and $(Phe-H+4O+N)H^+$ were the final products in the respective chemical processes.

$(Trp)H^+$ was detected at *m/z* 205.10 from a solution of Trp before the plasma treatment (Fig. 3.1.2g). The mass spectrum of the plasma-treated Trp showed two oxidation products corresponding to $(Trp+O)H^+$ at *m/z* 221.09 and $(Trp+2O)H^+$ at *m/z* 237.09 (Fig. 3.1.2h,i). In contrast to the other aromatic amino acids (Tyr and Phe), nitration of Trp was not observed. This result suggests that Trp has low reactivity to reactive nitrogen species, such as NO, $NO_2$, and $ONOO^-$.

## Sulphur-containing amino acids: Cys and Met

$(Cys)H^+$ was detected at *m/z* 122.03 from a solution of Cys before the plasma treatment (Fig. 3.1.3a). The mass spectrum of the plasma-treated Cys showed two oxidation products corresponding to $(Cys+3O)H^+$ at *m/z* 170.01 and $(2Cys-2H)H^+$ at *m/z* 241.03 (Fig. 3.1.3b,c). $(Cys+3O)H^+$ at *m/z* 170.01 and $(2Cys-2H)H^+$ at *m/z* 241.03 likely correspond to sulphonated Cys and the disulphide-bonded Cys dimer cystine, respectively, because the thiol group of the Cys side chain is highly reactive[57-59]. The peak intensity ratio $(Cys+3O)H^+/(Cys)H^+$ increased with plasma treatment time, while the $(2Cys-2H)H^+/(Cys)H^+$ ratio increased at 5 min of plasma treatment and then decreased at 10 min. These results suggest that sulphonated Cys is the final product of the plasma treatment, consistent with a previous report that disulphide-bonded Cys in glutathione (a tripeptide containing Cys) was irreversibly sulphonated by exposure to ROS[59].

From a solution of Met before plasma treatment, $(Met)H^+$ at *m/z* 150.06 and other peaks of *m/z* 104.05 and 133.03 were detected (Fig. 3.1.3d). Considering the transformation of Met during ESI-MS analysis[52], the peaks at *m/z* 104.05 and 133.03 are $(Met-CO-H_2O)H^+$ and $(Met-NH_3)H^+$, respectively. The mass spectrum of Met after plasma treatment for 5 min showed three products of *m/z* 74.02, 102.03, and 166.05 (Fig. 3.1.3e). The mass spectrum of Met after plasma treatment for 10 min showed seven products of *m/z* 184.03, 136.06, 134.04, 118.05, 122.55, 102.03, and 74.02 (Fig. 3.1.3f). Considering the transformation of oxidised Met during ESI-MS analysis[52], it is plausible that three oxidation compounds, (Met+O), (Met+2O), and (Met-2H+3O-C), were produced by plasma treatment: [i] Met sulphoxide[60, 61] $(Met+O)H^+$ at *m/z* 166.05 and some $(Met+O)H^+$ transformed into $(Met+O-CH_3SOH)H^+$ at *m/z* 102.03 and $(Met+O-C_3H_8SO)H^+$ at *m/z* 74.02 during ESI-MS analysis; [ii] $MetO_2$[57], which transforms into $(Met+2O-CO-H_2O)H^+$ at *m/z* 136.06 and $(Met+2O-CH_3SOH)H^+$ at *m/z* 118.05 during ESI-MS analysis; and [iii] $(Met-2H+3O-C)H^+$ at *m/z* 184.03. The products at *m/z* 122.55 and 134.04 could not be assigned. Intriguingly, the original Met peaks at *m/z* 150.06, 133.03, and 104.05 were not observed in the mass spectrum after plasma treatment for 5 min (Fig. 3.1.3e). This result indicates that Met is rapidly oxidised by plasma treatment. This feature of Met was also evident in the competitive plasma treatment experiment discussed later.

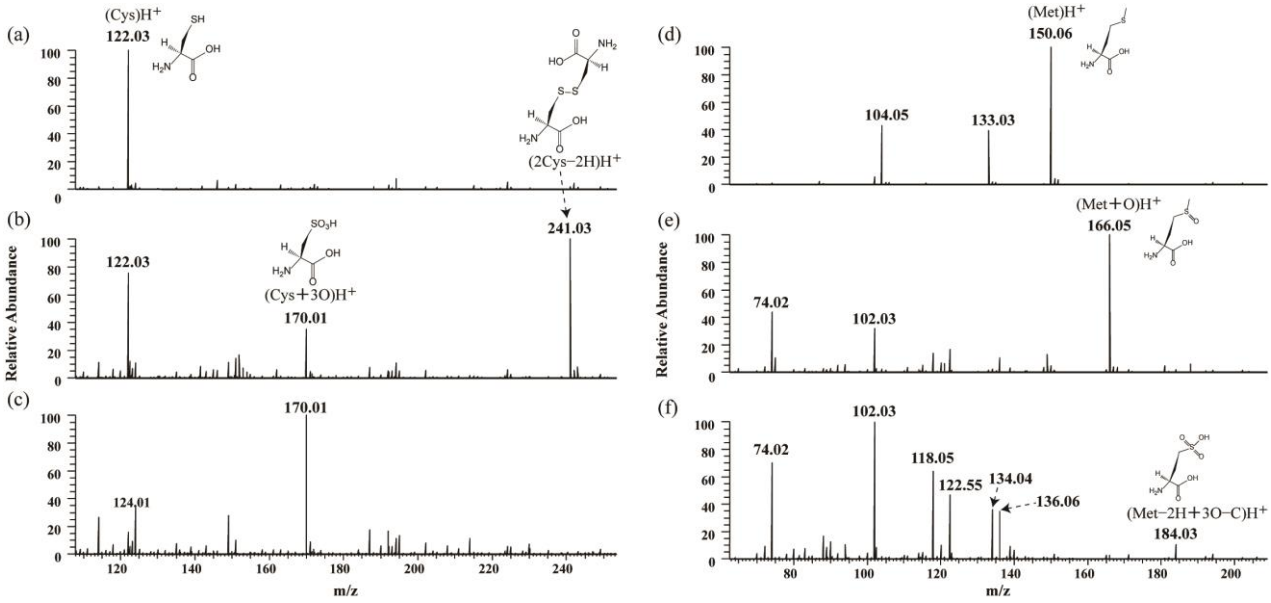


**Figure. 3.1.3.** Mass spectra of Cys (a-c) and Met (d-f) treated with plasma for 0 min (a,d), 5 min (b,e), and 10 min (c,f). A molecular structure of the proposed product is shown for each peak.

## Pyrrolidine- and imidazole-containing amino acids: Pro and His

$(Pro)H^+$ was detected at *m/z* 116.07 from a solution of Pro before the plasma treatment (Fig. 3.1.4a). The mass spectrum of Pro after plasma treatment showed three oxidation products corresponding to $(Pro\text{-}2H+O)H^+$ at *m/z* 130.05, $(Pro+O)H^+$ at *m/z* 132.07, and $(Pro+2O)H^+$ at *m/z* 148.06 (Fig. 3.1.4b,c). These oxidation reactions likely occurred in the pyrrolidine ring of Pro and were assigned as pyrrolidone carboxylic acid[50, 62] at *m/z* 130.05, hydroxyl aminovaleric acid[63] at *m/z* 132.07, and glutamic acid at *m/z* 148.06 (as shown in Fig. 3.1.4b,c). The conversion of Pro into glutamic acid via pyrrolidone carboxylic acid occurs during proline metabolism[64].

$(His)H^+$ was detected at *m/z* 156.08 from a solution of His before the plasma treatment (Fig. 3.1.4d). The mass spectrum of His after the plasma treatment showed two products, $(His+2O)H^+$ at *m/z* 188.07 and $(His+3O)H^+$ at m/z 204.06 (Fig. 3.1.4e,f). Oxidised His has been reported to transform during ESI-MS analysis[52], and thus some of the $(His+3O)H^+$ may transform to $(His+3O\text{-}NHCO)H^+$ at *m/z* 161.06 during ESI-MS analysis. $(His+O)H^+$ was not observed in plasma-treated His (Fig. 3.1.4e,f), but 2-oxohistidine (His+O) is known to occur during oxidation of His[50, 51, 65]. Therefore, it is plausible that (His+O) was formed by plasma treatment and then further oxidised to $(His+2O)H^+$ at *m/z* 188.07. $(His+3O)H^+$ at m/z 204.06 could be assigned to a ring-opened structure (as shown in Fig. 3.1.4f). Ring-opened His was previously reported to be formed as an oxidation product of His reacted with ozone[52].

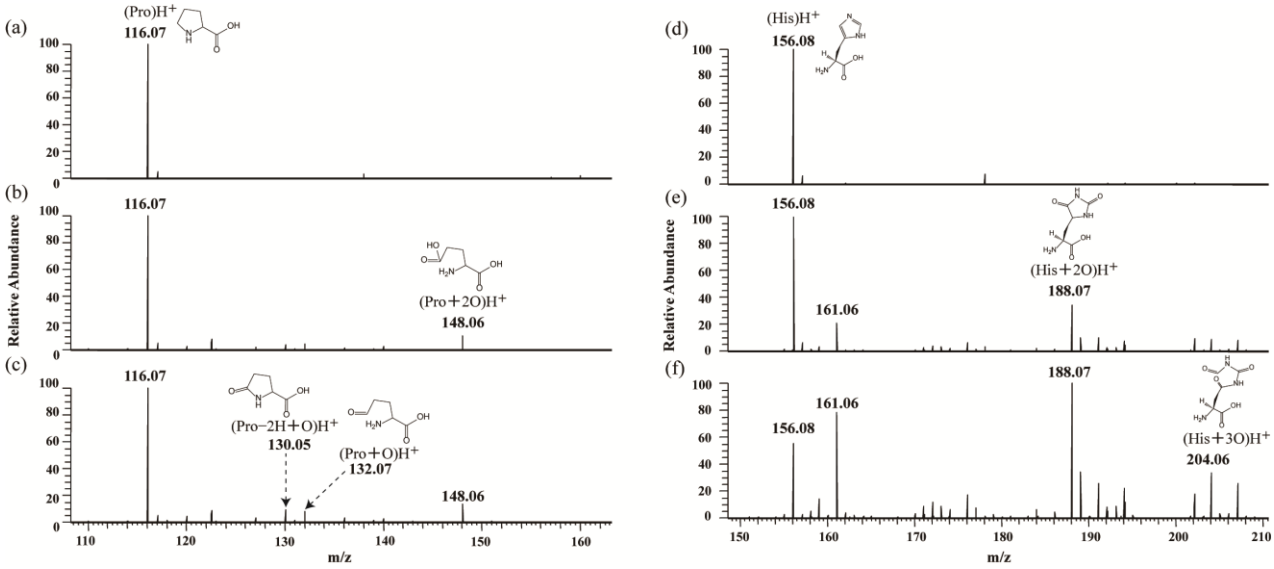


**Figure. 3.1.4.** Mass spectra of Pro (a-c) and His (d-f) treated with plasma for 0 min (a,d), 5 min (b,e), and 10 min (c,f). A molecular structure of the proposed product is shown for each peak.

## Basic amino acids: Lys and Arg

$(Lys)H^+$ was detected at *m/z* 147.11 from a solution of Lys before plasma treatment (Fig. 3.1.5a). The mass spectrum of Lys after plasma treatment showed three oxidation products corresponding to $(Lys\text{-}4H)H^+$ at *m/z* 143.08, $(Lys\text{-}5H+O\text{-}N)H^+$ at *m/z* 144.07, and $(Lys\text{-}2H+O)H^+$ at *m/z* 161.09 (Fig. 3.1.4b,c). As shown in Fig. 5b, the proposed structures of (Lys-4H), (Lys-5H+O-N), and (Lys-2H+O) are an imine with conjugated olefin, aldehyde, and amide, respectively. The major final product is likely the aldehyde (Lys-5H+O-N), which forms from the imine with conjugated olefin (Lys-4H) by hydrolysis. The peak intensity ratio $(Lys\text{-}2H+O)H^+/(Lys)H^+$ was lower than that of $(Lys\text{-}4H)H^+$ and $(Lys\text{-}5H+O\text{-}N)H^+$, indicating that the amide (Lys-2H+O) is a minor product.

$(Arg)H^+$ was detected at *m/z* 175.12 from a solution of Arg before plasma treatment (Fig. 3.1.5d). The mass spectrum of Arg after plasma treatment showed two oxidation products corresponding to $(Arg\text{-}4H)H^+$ at *m/z* 171.09 and $(Arg+2O)H^+$ at *m/z* 207.11 (Fig. 3.1.5e,f). As shown in Fig. 3.1.5e, the proposed structures of $(Arg\text{-}4H)H^+$ and $(Arg+2O)H^+$ are conjugated diene and di-hydroxylated Arg, respectively. Hydroxylation of Arg was previously reported in metal-catalysed oxidation reactions[63].

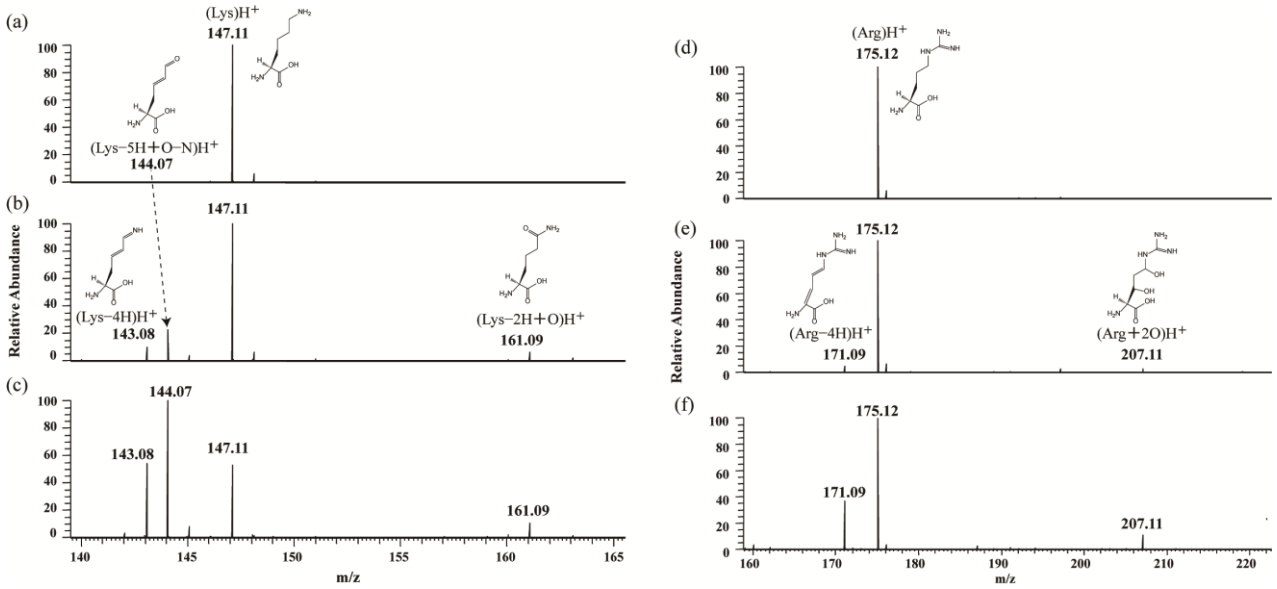


**Figure. 3.1.5.** Mass spectra of Lys (a-c) and Arg (d-f) treated with plasma for 0 min (a,d), 5 min (b,e), and 10 min (c,f). A molecular structure of the proposed product is shown for each peak.

## Amido- and carboxyl-containing amino acids: Gln and Glu

$(Gln)H^+$ and (Glu)H+ were detected at *m/z* 147.08 and *m/z* 148.06, respectively (Fig. 3.1.6a,d). The mass spectrum of the plasma-treated Gln showed one oxidation product corresponding to $(Gln\text{-}2H+O)H^+$ at m/z 161.06 (Fig. 3.1.6b,c). The mass spectrum of the plasma-treated Glu showed two oxidation products corresponding to $(Glu+O)H^+$ of m/z 164.06 and $(Glu+2O)H^+$ of m/z 180.05

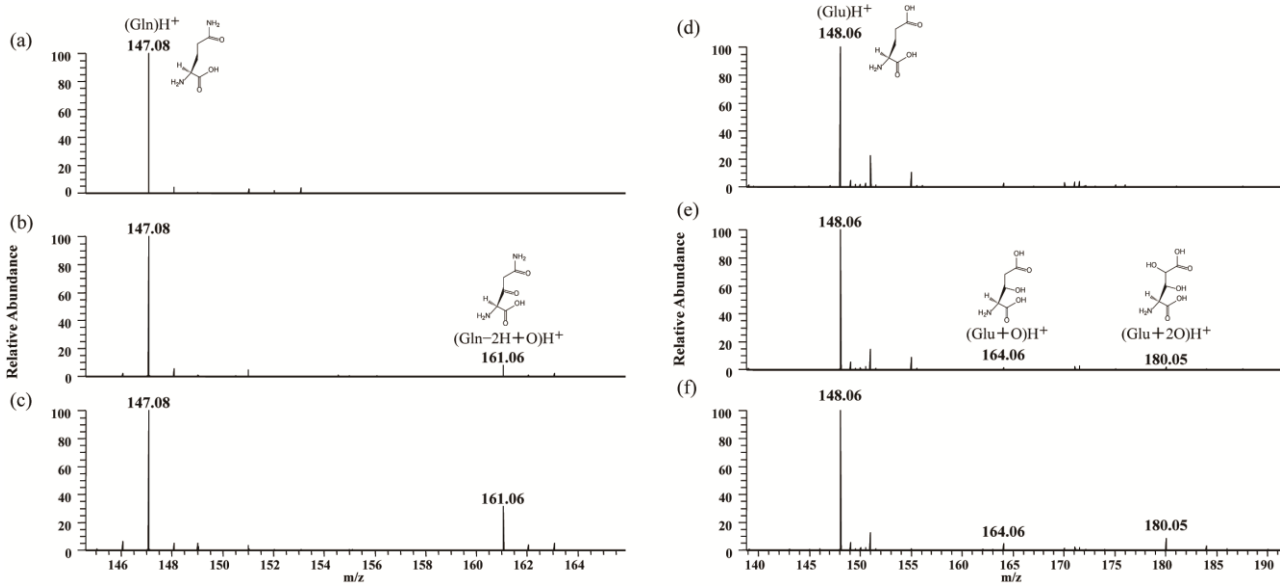


**Figure. 3.1.6.** Mass spectra of Gln (a-c) and Glu (d-f) treated with plasma for 0 min (a,d), 5 min (b,e), and 10 min (c,f). A molecular structure of the proposed product is shown for each peak.

(Fig. 3.1.6e,f). By contrast, oxidation of Asn and Asp by plasma treatment was not observed (data not shown). Compared to Glu and Asp, Gln and Asn contain an additional methylene group, respectively. The hydroxylations of Gln and Asn likely occurred at these methylene groups, yielding ketonised Gln at m/z 161.06 and hydroxylated Glu at m/z 164.06 as products, respectively (as shown in Fig. 3.1.6b,e). The chemical structure of $(Glu+2O)H^+$ at m/z 180.05 is proposed to be the diol (as shown in Fig. 3.1.6e) formed from the hydroxylated Glu.

## Branched-chain amino acids: Val, Leu, and Ile

$(Val)H^+$ was detected at *m/z* 118.09 from a solution of Val before plasma treatment (Fig. 3.1.7a). The mass spectrum of Val after plasma treatment showed seven oxidation products corresponding to $(Val-2H)H^+$ at *m/z* 116.07, $(Val-2H+O)H^+$ at *m/z* 132.07, $(Val+O)H^+$ at *m/z* 134.08, $(Val-2H+2O)H^+$ at *m/z* 148.06, $(Val+2O)H^+$ at *m/z* 150.08, $(Val+3O)H^+$ at *m/z* 166.07, and $(Val-H+3O+N)H^+$ at *m/z* 179.07 (Fig. 3.1.7b,c). As shown in Fig. 3.1.7b,c, the proposed structures of (Val-2H), (Val-2H+O), (Val+O), (Val-2H+2O), (Val+2O), (Val+3O), and (Val-H+3O+N) are dehydroxylated, formylated, hydroxylated, carboxylated, dihydroxylated, hydroxylated/carboxylated, and hydroxylated/nitrated Val, respectively.

$(Leu)H^+$ was detected at *m/z* 132.10 from a solution of Leu before plasma treatment (Fig. 3.1.7d). The mass spectrum of Leu after plasma treatment showed nine oxidation products corresponding to $(Leu-4H)H^+$ at *m/z* 128.07, $(Leu-2H)H^+$ at *m/z* 130.09, $(Leu-2H+O)H^+$ at *m/z* 146.08, $(Leu+O)H^+$ at *m/z* 148.10, $(Leu-2H+2O)H^+$ at *m/z* 162.08, $(Leu+2O)H^+$ at *m/z* 164.09, $(Leu-2H+3O)H^+$ at *m/z* 178.07, $(Leu+3O)H^+$ at *m/z* 180.09, and $(Leu-H+3O+N)H^+$ at *m/z* 193.08 (Fig. 3.1.7e,f). As shown in Fig. 3.1.7e,f, the proposed structures of (Leu-4H), (Leu-2H), (Leu-2H+O), (Leu+O), (Leu-2H+2O), (Leu+2O), (Leu+3O), and (Leu-H+3O+N) are didehydroxylated, dehydroxylated, formylated, hydroxylated, carboxylated, di-hydroxylated, hydroxylated/carboxylated, tri-hydroxylated, and hydroxylated/nitrated Leu, respectively.

$(Ile)H^+$ was detected at *m/z* 132.10 from a solution of Ile before plasma treatment (Fig. 3.1.7g). The mass spectrum of Ile after plasma treatment showed eight oxidation products corresponding to $(Ile-4H)H^+$ at *m/z* 128.07, $(Ile-2H)H^+$ at *m/z* 130.09, $(Ile-2H+O)H^+$ at *m/z* 146.08, $(Ile+O)H^+$ at *m/z* 148.10, $(Ile-2H+2O)H^+$ at *m/z* 162.08, $(Ile+2O)H^+$ at *m/z* 164.09, $(Ile-2H+3O)H^+$ at *m/z* 178.07, and $(Ile-H+3O+N)H^+$ at *m/z* 193.08 (Fig. 3.1.7h,i). As shown in Fig. 3.1.7h,i, the proposed structures of (Leu-4H), (Leu-2H), (Leu-2H+O), (Leu+O), (Leu-2H+2O), (Leu+2O), (Ile-2H+3O), and (Leu-H+3O+N) are didehydroxylated, dehydroxylated, formylated, hydroxylated, carboxylated, di-hydroxylated, hydroxylated/carboxylated, and hydroxylated/nitrated Ile, respectively.

Various products were observed after plasma treatment of branched-chain amino acids (Fig. 3.1.7). Unsaturated Val, Leu, and Ile were detected (Fig. 3.1.7c,e,h). Unsaturated fatty acids have

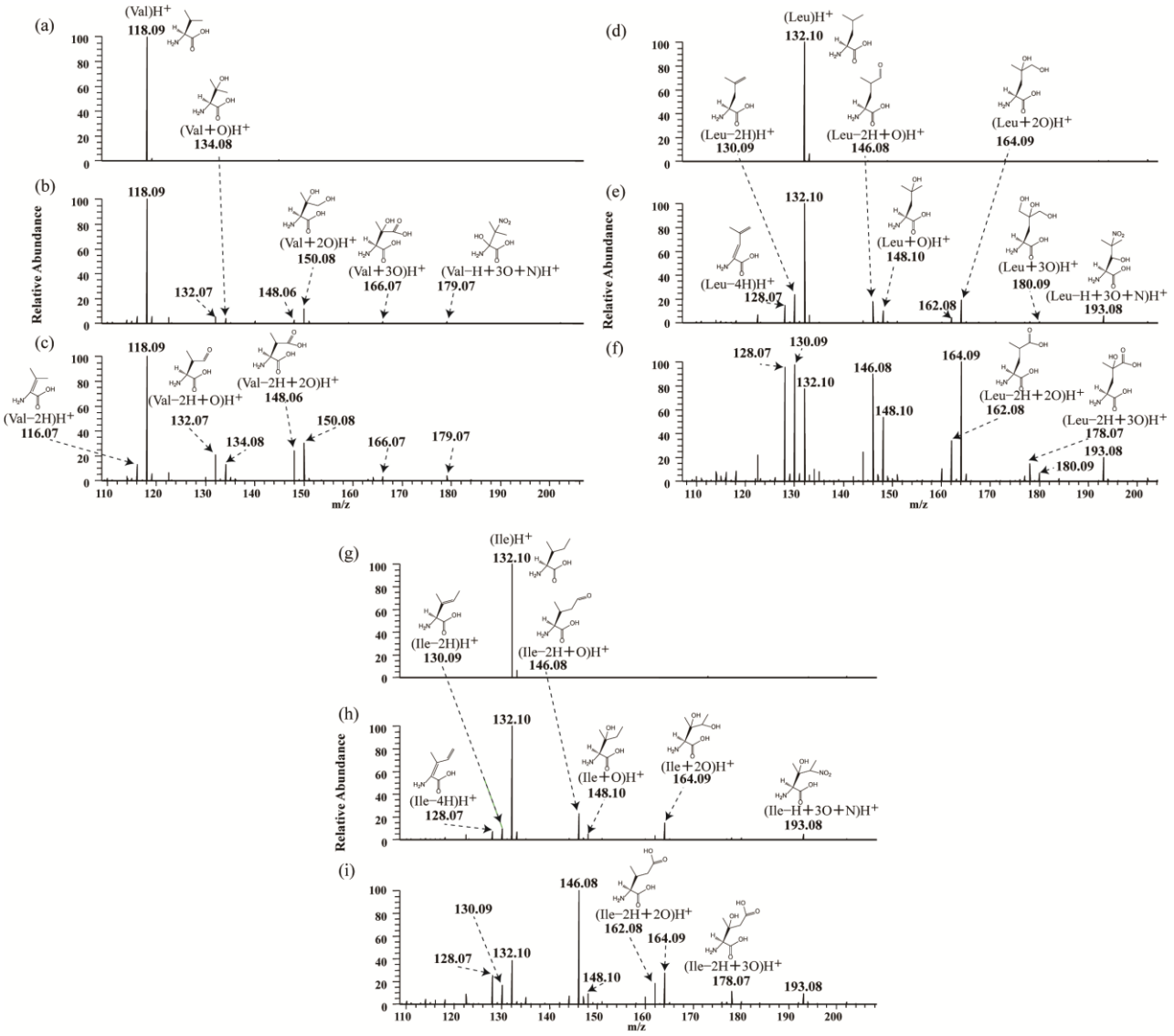


**Figure. 3.1.7.** Mass spectra of Val (a-c), Leu (d-f), and Ile (g-i) treated with plasma for 0 min (a,d,g), 5 min (b,e,h), and 10 min (c,f,i). A molecular structure of the proposed product is shown for each peak.

been reported to form a variety of oxidised products[66]. Therefore, the various products observed upon plasma treatment may be due to amino acids with unsaturated side chains.

## Relative reactivity of amino acids to plasma treatment

The relative reactivity of the 20 amino acids was estimated from a competitive plasma treatment experiment (Fig. 3.1.8). A solution containing the 20 amino acids was subjected to plasma treatment for the indicated time, and then the concentration of the amino acids was measured by conventional amino-acid analysis. Figure 8 shows that the reactivity of the 20 amino acids was Met > Cys > Trp > Phe > Tyr > His > others. Notably, Met was completely degraded by plasma treatment for 10 min. This result is consistent with the MS data, in which the original Met peaks were not observed in the

mass spectra after plasma treatment for 10 min (Fig. 3.1.3f). These results indicate that the Met residues in a protein are most readily modified by plasma treatment.

The concentration of the disulphide-bonded Cys dimer cystine was also measured by the amino acid analyser (Fig. 3.1.8). Cystine and sulphonated Cys were the products of plasma-treated Cys (Fig. 3.1.3b and 3.1.3c). Therefore, the concentration of sulphonated Cys was calculated from those of Cys and cystine (as shown in Fig. 3.1.8). The concentrations of cystine and sulphonated Cys increased with plasma treatment time. These results indicate that disulphide-bond formation and sulphonation occur simultaneously. Cys plays an important role in protein folding and stability[67]. Thus, degradation of Cys is a key aspect of protein inactivation by plasma treatment.

Interestingly, plasma treatment decreased Trp more rapidly than Phe and Tyr (Fig. 3.1.8), but in contrast to Tyr and Phe, Trp was hydroxylated but not nitrated (Fig. 3.1.2). These results indicate that hydroxylation of Trp residues in proteins is a major reaction during plasma treatment. These data are supported by our previous report that the intrinsic fluorescence of Tyr residues in a protein decreases rapidly upon plasma treatment[45].

Finally, sulphur-containing and aromatic amino acids were preferentially decreased by plasma treatment of the 20 amino acids under competitive conditions (Fig. 3.1.8). We previously reported that hen egg-white lysozyme, a model enzyme with active-site Glu and Asp residues[68], was slowly inactivated by the same plasma treatment[45]. Taken together, these results lead us to predict that an enzyme will be rapidly inactivated by plasma treatment if the enzyme has sulphur-containing and aromatic amino acids in its active site. This information is important for understanding the mechanism of action of plasma medicine.

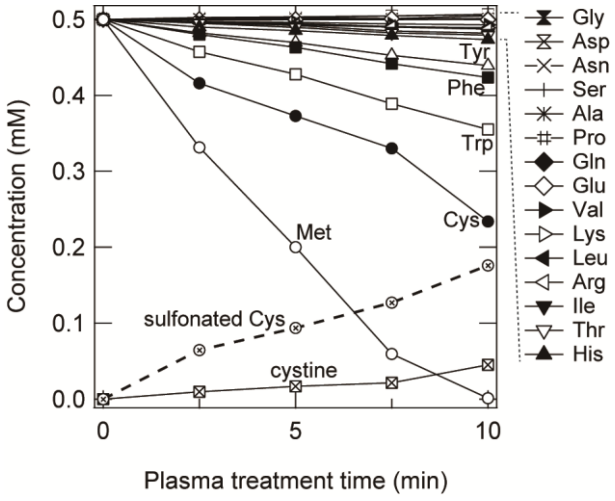


**Figure. 3.1.8.** Competitive plasma treatment of 20 amino acids. The prepared concentration of the amino acids was 0.5 mM; the concentration of amino acids in the plasma-treated sample was determined by amino-acid analysis. The concentration of cystine was also measured, and the concentration of sulphonated Cys was calculated from those of Cys and cystine.

# Conclusion

In summary, we examined the chemical effects of plasma treatment in aqueous solution of 20 amino acids that comprise proteins. The side chains of 14 amino acids were oxidised to form various products, and sulphur-containing and aromatic amino acids were preferentially decreased in a competitive plasma treatment experiment. The oxidation reactions of amino acid side chains are well-known in organic chemistry[69]. Cysteine residues of proteins often play critical roles in enzyme catalysis as part of metabolism and signalling[70]. Proteins are a major target of ROS [71]. Therefore, this study is of fundamental importance for elucidating the mechanism of protein inactivation to facilitate the development of biomedical plasma applications.

An LF plasma jet was used as the APCP system to examine the chemical effects of plasma treatment on 20 amino acids. The LF plasma jet is a simple APCP system. Threfore, some of the chemical reactions reported in this study may occur when other APCP systems are used. The information presented in this paper represents a crucial first step for understanding the mechanism of action of plasma medicine.

# References


[1] Bruggeman P, Iza F, Lauwers D and Gonzalvo Y A 2010 Mass spectrometry study of positive and negative ions in a capacitively coupled atmospheric pressure RF excited glow discharge in He-water mixtures *Journal of Physics D-Applied Physics* **43** 012003

[2] Locke B R, Sato M, Sunka P, Hoffmann M R and Chang J S 2006 Electrohydraulic discharge and nonthermal plasma for water treatment *Ind. Eng. Chem. Res.* **45** 882-905

[3] Sahni M and Locke B R 2006 The effects of reaction conditions on liquid-phase hydroxyl radical production in gas-liquid pulsed-electrical-discharge reactors *Plasma Processes and Polymers* **3** 668-81

[4] Sahni M and Locke B R 2006 Quantification of hydroxyl radicals produced in aqueous phase pulsed electrical discharge reactors *Ind. Eng. Chem. Res.* **45** 5819-25

[5] Bruggeman P and Leys C 2009 Non-thermal plasmas in and in contact with liquids *Journal of Physics D-Applied Physics* **42** 053001

[6] Burlica R, Shih K Y and Locke B R 2010 Formation of H-2 and H2O2 in a Water-Spray Gliding Arc Nonthermal Plasma Reactor *Ind. Eng. Chem. Res.* **49** 6342-9

[7] Tani A, Ono Y, Fukui S, Ikawa S and Kitano K 2012 Free radicals induced in aqueous solution by non-contact atmospheric-pressure cold plasma *Appl. Phys. Lett.* **100** 254103

[8] Ikawa S, Kitano K and Hamaguchi S 2010 Effects of pH on Bacterial Inactivation in Aqueous Solutions due to Low-Temperature Atmospheric Pressure Plasma Application *Plasma Processes and Polymers* **7** 33-42

[9] Liu D X, Rong M Z, Wang X H, Iza F, Kong M G and Bruggeman P 2010 Main Species and Physicochemical Processes in Cold Atmospheric-pressure He + O-2 Plasmas *Plasma Processes and Polymers* **7** 846-65

[10] Furusho H, Miyamoto D, Nagasaki Y, Kitano K and Hamaguchi S 2007 Synthesis of uniformly dispersed metal nanoparticles with dispersion stability by nonequilibrium atmospheric plasma jets *J. Photopolym. Sci. Technol.* **20** 229-33

[11] Furusho H, Kitano K, Hamaguchi S and Nagasaki Y 2009 Preparation of Stable Water-Dispersible PEGylated Gold Nanoparticles Assisted by Nonequilibrium Atmospheric-Pressure Plasma Jets *Chem. Mater.* **21** 3526-35

[12] Sumitani S, Murotani H, Oishi M, Kitano K, Hamaguchi S and Nagasaki Y 2009 Nonequilibrium Atmospheric Plasma Jets Assisted Stabilization of Drug Delivery Carriers: Preparation and Characterization of Biodegradable Polymeric Nano-Micelles with Enhanced Stability *J. Photopolym. Sci. Technol.* **22** 467-71

[13] Garcia-Reyes J F, Mazzotti F, Harper J D, Charipar N A, Oradu S, Ouyang Z, Sindona G and Cooks R G 2009 Direct olive oil analysis by low-temperature plasma (LTP) ambient ionization mass spectrometry *Rapid Commun. Mass Spectrom.* **23** 3057-62

[14] Harper J D, Charipar N A, Mulligan C C, Zhang X R, Cooks R G and Ouyang Z 2008 Low-Temperature Plasma Probe for Ambient Desorption Ionization *Anal. Chem.* **80** 9097-104

[15] Kylián O, Rauscher H, Denis B, Ceriotti L and Rossi F 2009 Elimination of Homo-polypeptides of Amino Acids from Surfaces by means of Low Pressure Inductively Coupled Plasma Discharge *Plasma Processes and Polymers* **6** 848–54

[16] Lee H W, Nam S H, Mohamed A-A H, Kim G C and Lee J K 2010 Atmospheric Pressure Plasma Jet Composed of Three Electrodes: Application to Tooth Bleaching *Plasma Processes and Polymers* **7** 274-80

[17] Kong M G, Kroesen G, Morfill G, Nosenko T, Shimizu T, van Dijk J and Zimmermann J L 2009 Plasma medicine: an introductory review *New Journal of Physics* **11** 115012

[18] Babaeva N Y and Kushner M J 2013 Reactive fluxes delivered by dielectric barrier discharge filaments to slightly wounded skin *J. Phys. D: Appl. Phys.* **46** 025401

[19] Fridman G, Friedman G, Gutsol A, Shekhter A B, Vasilets V N and Fridman A 2008 Applied plasma medicine *Plasma Processes and Polymers* **5** 503-33

[20] Sato T, Yokoyama M and Johkura K 2011 A key inactivation factor of HeLa cell viability by a plasma flow *J. Phys. D: Appl. Phys.* **44** 372001

[21] Kim K, Choi J D, Hong Y C, Kim G, Noh E J, Lee J-S and Yang S S 2011 Atmospheric-pressure plasma-jet from micronozzle array and its biological effects on living cells for cancer therapy *Appl. Phys. Lett.* **98** 073701

[22] Kim S J, Chung T H, Bae S H and Leem S H 2010 Induction of apoptosis in human breast cancer cells by a pulsed atmospheric pressure plasma jet *Appl. Phys. Lett.* **97** 023702

[23] Kim C H, Kwon S, Bahn J H, Lee K, Jun S I, Rack P D and Baek S J 2010 Effects of atmospheric nonthermal plasma on invasion of colorectal cancer cells *Appl. Phys. Lett.* **96** 243701

[24] Barekzi N and Laroussi M 2013 Effects of Low Temperature Plasmas on Cancer Cells *Plasma Processes and Polymers* **10** 1039-50

[25] Vandamme M, Robert E, Pesnel S, Barbosa E, Dozias S, Sobilo J, Lerondel S, Le Pape A and Pouvesle J M 2010 Antitumor Effect of Plasma Treatment on U87 Glioma Xenografts: Preliminary Results *Plasma Processes and*

*Polymers* **7** 264-73

[26] Yamazaki H, Ohshima T, Tsubota Y, Yamaguchi H, Jayawardena J A and Nishimura Y 2011 Microbicidal activities of low frequency atmospheric pressure plasma jets on oral pathogens *Dent. Mater. J.* **30** 384-91

[27] Fridman G, Peddinghaus M, Balasubramanian M, Ayan H, Fridman A, Gutsol A and Brooks A 2006 Blood Coagulation and Living Tissue Sterilization by Floating-Electrode Dielectric Barrier Discharge in Air *Plasma Chem. Plasma Process.* **26** 425-42

[28] Gweon B, Kim D, Kim D B, Jung H, Choe W and Shin J H 2010 Plasma effects on subcellular structures *Appl. Phys. Lett.* **96** 101501

[29] Perni S, Shama G, Hobman J L, Lund P A, Kershaw C J, Hidalgo-Arroyo G A, Penn C W, Deng X T, Walsh J L and Kong M G 2007 Probing bactericidal mechanisms induced by cold atmospheric plasmas with Escherichia coli mutants *Appl. Phys. Lett.* **90** 073902

[30] Feng H Q, Wang R X, Sun P, Wu H Y, Liu Q, Fang J, Zhu W D, Li F T and Zhang J 2010 A study of eukaryotic response mechanisms to atmospheric pressure cold plasma by using Saccharomyces cerevisiae single gene mutants *Appl. Phys. Lett.* **97** 131501

[31] Bussiahn R, Brandenburg R, Gerling T, Kindel E, Lange H, Lembke N, Weltmann K D, von Woedtke T and Kocher T 2010 The hairline plasma: An intermittent negative dc-corona discharge at atmospheric pressure for plasma medical applications *Appl. Phys. Lett.* **96** 143701

[32] Kolb J F, Mohamed A A H, Price R O, Swanson R J, Bowman A, Chiavarini R L, Stacey M and Schoenbach K H 2008 Cold atmospheric pressure air plasma jet for medical applications *Appl. Phys. Lett.* **92** 241501

[33] Zhang X, Huang J, Liu X, Peng L, Guo L, Lv G, Chen W, Feng K and Yang S-z 2009 Treatment of Streptococcus mutans bacteria by a plasma needle *J. Appl. Phys.* **105** 063302

[34] Lu X, Ye T, Cao Y, Sun Z, Xiong Q, Tang Z, Xiong Z, Hu J, Jiang Z and Pan Y 2008 The roles of the various plasma agents in the inactivation of bacteria *J. Appl. Phys.* **104** 053309

[35] Majumdar A, Singh R K, Palm G J and Hippler R 2009 Dielectric barrier discharge plasma treatment on E. coli: Influence of CH[sub 4]/N[sub 2], O[sub 2], N[sub 2]/O[sub 2], N[sub 2], and Ar gases *J. Appl. Phys.* **106** 084701

[36] Burlica R, Grim R G, Shih K Y, Balkwill D and Locke B R 2010 Bacteria Inactivation Using Low Power Pulsed Gliding Arc Discharges with Water Spray *Plasma Processes and Polymers* **7** 640-9

[37] Takai E, Ikawa S, Kitano K, Kuwabara J and Shiraki K 2013 Molecular mechanism of plasma sterilization in solution with the reduced pH method: importance of permeation of HOO radicals into the cell membrane *Journal of Physics D-Applied Physics* **46** 295402

[38] Nagatsu M, Zhao Y, Motrescu I, Mizutani R, Fujioka Y and Ogino A 2012 Sterilization Method for Medical Container Using Microwave-Excited Volume-Wave Plasma *Plasma Processes and Polymers* **9** 590-6

[39] Karakas E, Munyanyi A, Greene L and Laroussi M 2010 Destruction of alpha-synuclein based amyloid fibrils by a low temperature plasma jet *Appl. Phys. Lett.* **97** 143702

[40] Takai E, Ohashi G, Yoshida T, Sörgjerd K M, Zako T, Maeda M, Kitano K and Shiraki K 2014 Degeneration of Amyloid-ß Fibrils Caused by Exposure to Low-Temperature Atmospheric-Pressure Plasma in Aqueous Solution *Appl. Phys. Lett.* DOI: 10.1063/1.4861842

[41] Yan X, Zou F, Lu X P, He G Y, Shi M J, Xiong Q, Gao X, Xiong Z L, Li Y, Ma F Y, Yu M, Wang C D, Wang Y

S and Yang G X 2009 Effect of the atmospheric pressure nonequilibrium plasmas on the conformational changes of plasmid DNA *Appl. Phys. Lett.* **95** 083702

[42] Li G, Li H P, Wang L Y, Wang S, Zhao H X, Sun W T, Xing X H and Bao C Y 2008 Genetic effects of radio-frequency, atmospheric-pressure glow discharges with helium *Appl. Phys. Lett.* **92**

[43] Julák J, Janoušková O, Scholtz V and Holada K 2011 Inactivation of Prions Using Electrical DC Discharges at Atmospheric Pressure and Ambient Temperature *Plasma Processes and Polymers* **8** 316-23

[44] Yasuda H, Hashimoto M, Rahman M M, Takashima K and Mizuno A 2008 States of Biological Components in Bacteria and Bacteriophages during Inactivation by Atmospheric Dielectric Barrier Discharges *Plasma Processes and Polymers* **5** 615-21

[45] Takai E, Kitano K, Kuwabara J and Shiraki K 2012 Protein Inactivation by Low-temperature Atmospheric Pressure Plasma in Aqueous Solution *Plasma Processes and Polymers* **9** 77-82

[46] Ke Z G, Huang Q, Su X, Jiang J, Wang X Q and Yu Z L 2010 A paradigm study for assessment of phenylalanine's damage under arc-discharge irradiation *Nuclear Instruments & Methods in Physics Research Section B-Beam Interactions with Materials and Atoms* **268** 1618-25

[47] Ke Z G, Huang Q, Dang B R, Lu Y L, Yuan H, Zhang S Q and Yu Z L 2010 A study of low-energy ion induced radiolysis of thiol-containing amino acid cysteine in the solid and aqueous solution states *Nuclear Instruments & Methods in Physics Research Section B-Beam Interactions with Materials and Atoms* **268** 2729-34

[48] Ke Z G, Yu Z L and Huang Q 2013 Assessment of Damage of Glutathione by Glow Discharge Plasma at the GasSolution Interface through Raman Spectroscopy *Plasma Processes and Polymers* **10** 181-8

[49] Xian F, Hendrickson C L and Marshall A G 2012 High Resolution Mass Spectrometry *Anal. Chem.* **84** 708-19

[50] Stadtman E R and Levine R L 2003 Free radical-mediated oxidation of free amino acids and amino acid residues in proteins *Amino Acids* **25** 207-18

[51] Roeser J, Bischoff R, Bruins A P and Permentier H P 2010 Oxidative protein labeling in mass-spectrometry-based proteomics *Anal. Bioanal. Chem.* **397** 3441-55

[52] Kotiaho T, Eberlin M N, Vainiotalo P and Kostiainen R 2000 Electrospray mass and tandem mass spectrometry identification of ozone oxidation products of amino acids and small peptides *J. Am. Soc. Mass Spectrom.* **11** 526-35

[53] Lloyd J A, Spraggins J M, Johnston M V and Laskin J 2006 Peptide ozonolysis: Product structures and relative reactivities for oxidation of tyrosine and histidine residues *J. Am. Soc. Mass Spectrom.* **17** 1289-98

[54] Lin J K, Chen K J, Liu G Y, Chu Y R and Lin-Shiau S Y 2000 Nitration and hydoxylation of aromatic amino acid and guanine by the air pollutant peroxyacetyl nitrate *Chem.-Biol. Interact.* **127** 219-36

[55] Beckman J S, Ischiropoulos H, Zhu L, Vanderwoerd M, Smith C, Chen J, Harrison J, Martin J C and Tsai M 1992 Kinetics of Superoxide Dismutase-Catalyzed and Iron-Catalyzed Nitration of Phenolics by Peroxynitrite *Arch. Biochem. Biophys.* **298** 438-45

[56] Vandervliet A, Oneill C A, Halliwell B, Cross C E and Kaur H 1994 Aromatic Hydroxylation and Nitration of Phenylalanine and Tyrosine by Peroxynitrite - Evidence for Hydroxyl Radical Production from Peroxynitrite *FEBS Lett.* **339** 89-92

[57] Matthiesen R, Bauw G and Welinder K G 2004 Use of performic acid oxidation to expand the mass distribution of tryptic peptides *Anal. Chem.* **76** 6848-52

[58] Samgina T Y, Artemenko K A, Gorshkov V A, Poljakov N B and Lebedev A T 2008 Oxidation versus carboxamidomethylation of S-S bond in Ranid frog peptides: Pro and contra for de novo MALDI-MS sequencing *J. Am. Soc. Mass Spectrom.* **19** 479-87

[59] Deutsch J C, Santhosh-Kumar C R and Kolhouse J F 1999 Glutathione oxidation in real time by thermospray liquid chromatography-mass spectrometry *J. Chromatogr.* **862** 161-8

[60] Schoneich C 2005 Methionine oxidation by reactive oxygen species: reaction mechanisms and relevance to Alzheimer's disease *Biochimica Et Biophysica Acta-Proteins and Proteomics* **1703** 111-9

[61] Nomoto S, Shimoyama A and Shiraishi S 1998 Flame-induced reactions of sulfur-containing amino acids in an aqueous solution *Tetrahedron Lett.* **39** 1009-12

[62] Uchida K, Kato Y and Kawakishi S 1990 A Novel Mechanism for Oxidative Cleavage of Prolyl Peptides Induced by the Hydroxyl Radical *Biochem. Biophys. Res. Commun.* **169** 265-71

[63] Amici A, Levine R L, Tsai L and Stadtman E R 1989 Conversion of Amino-Acid Residues in Proteins and Amino-Acid Homopolymers to Carbonyl Derivatives by Metal-Catalyzed Oxidation Reactions *J. Biol. Chem.* **264** 3341-6

[64] Hans Weil-Malherbe H A K 1935 Metabolism of amino-acids: The conversion of proline into glutamic acid in kidney *Biochem J.* **29** 2077-81

[65] Schoneich C 2000 Mechanisms of metal-catalyzed oxidation of histidine to 2-oxo-histidine in peptides and proteins *J. Pharm. Biomed. Anal.* **21** 1093-7

[66] Trostchansky A and Rubbo H 2008 Nitrated fatty acids: Mechanisms of formation, chemical characterization, and biological properties *Free Radic. Biol. Med.* **44** 1887-96

[67] Hogg P J 2003 Disulfide bonds as switches for protein function *Trends Biochem. Sci.* **28** 210-4

[68] Vocadlo D J, Davies G J, Laine R and Withers S G 2001 Catalysis by hen egg-white lysozyme proceeds via a covalent intermediate *Nature* **412** 835-8

[69] Xu G H and Chance M R 2007 Hydroxyl radical-mediated modification of proteins as probes for structural proteomics *Chem. Rev.* **107** 3514-43

[70] Klomsiri C, Karplus P A and Poole L B 2011 Cysteine-Based Redox Switches in Enzymes *Antioxidants & Redox Signaling* **14** 1065-77

[71] Davies M J 2005 The oxidative environment and protein damage *Biochim. Biophys. Acta* **1703** 93-109

# Chapter 4

# Chemical Effects on Enzyme

## 4.1 Protein Inactivation by Low-Temperature Atmospheric Pressure Plasma in Aqueous Solution

# Introduction

Plasma processing at atmospheric pressure has attracted a great deal of attention because of its advantageous features, such as its obviation of complicated and expensive vacuum systems, its capacity for adequate and controllable gas temperature, its high concentrations of chemically reactive species, and its flexible operation [1]. Such attributes of atmospheric pressure plasma have been applied as ionization for use in mass spectrometry [2,3], elimination of organic materials [4], tooth bleaching [5], and sterilization [6–23].

Although various biomedical applications of the atmospheric pressure plasma have been developed over the past decade, fundamental understanding of interaction between plasma and biomacromoledules has remained insufficient. Few experiments have examined the atmospheric pressure plasma destructed the tertiary structure of DNA in aqueous solution [24,25] and degradation of protein in dry conditions [26,27]. Recently, it has been reported that the LTAP plasma degrades proteins in aqueous solution. For example, LTAP plasma inactivates infectious prion protein [28], activates lipase in solution after treated within one minute [29] , and inactivates recombinant green fluorescent protein (GFP) in *E. coli* cells [14] . Although these effects of plasma on protein have been reported, molecular mechanisms of the plasma on enzymatic activity have remained unclear.

Our plasma system, using a low-frequency (LF) high-voltage (HV) power supply and a single-HV electrode, which is designated as a LF plasma jet, can easily generate LTAP plasma at low cost. The advantage of the LF plasma jet is the sterilization of bacteria in acidic solution without heat load, current, and ultraviolet rays (UV) [8]. To apply our LF plasma jet to biology and medical applications, this paper investigated enzymatic activity, secondary structure, intrinsic tryptophan fluorescence, and molecular weight. This report is the first of inactivation protein in aqueous solution by the plasma.

# Materials and methods

## Materials

Hen egg white lysozyme was obtained from Sigma Chemical Co. (St. Louis, MO). Sodium dihydrogen phosphate, glycine, and *Micrococcus lysodeikticus* were obtained from Wako Pure Chemical Industries Ltd. (Osaka, Japan). All compounds were of the highest commercially available grade.

## System of LF plasma jet

The experimental system, comprising the plasma generator and sample chamber, is shown in Fig. 4.1.1. The LF plasma jet was ejected from the end of the quartz glass tube, in which helium (He) gas flowed, by the application of a alternating current (AC) high voltage (from -3.5 to +5.0 kV with the frequency of 13.9 kHz) to the electrode, which was a small metal sheet wound around the tube [8] . The He plasma with low gas temperature was generated as an elongated shape. This LF plasma jet was generated inside the airtight chamber from its center port. The ambient gas of the chamber can

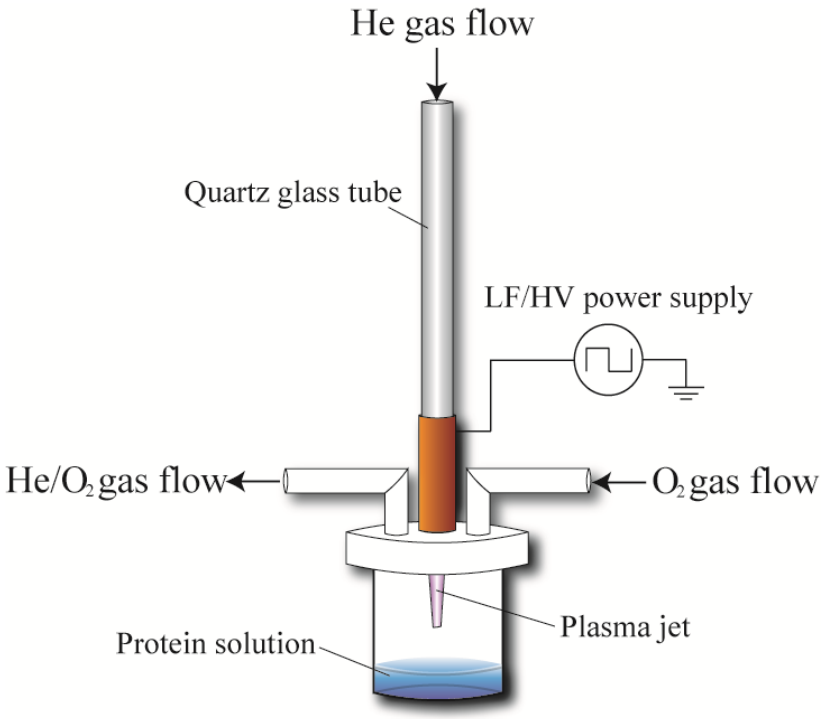


**Figure 4.1.1.** Schematic diagram of the plasma generation system. LF/HV pulses are applied to the electrode, which is wound around the quartz glass tube. The device is He-based low-temperature atmospheric plasma. Plasma is generated in He gas flowing (500 ml/min) in the quartz glass tube. A plume-like structure of the plasma (’plasma jet’) is extended toward the surface of a liquid. Flow of $O_2$ gas of 150 ml/min to the chamber maintains the $O_2$ concentration in the chamber atmosphere.

be controlled with the other oxygen ($O_2$) gas supply port connected to the side of the plasma jet port. The flow rates of He and $O_2$ gas were, respectively, 0.50 and 0.15 l/min. Various active oxygen species produced from $O_2$ gas by He plasma were supplied to the solution in the chamber. The sample of 0.3 ml containing 0.1 mg/ml lysozyme in 10 mM phosphate buffer (pH 7.4) was applied to the solution in the vessel. To exchange the ambient gas, He and $O_2$ gas were preflowed in the chamber for 3 min. After the plasma treatment, samples were corrected with pure water to compensate for evaporation .

## Enzyme assay

Enzymatic activity of lysozyme was determined as follows. In all, 1.5 ml of 0.5 mg/ml *M. lysodeikticus* solution in 10 mM sodium -phosphate buffer (pH 7.4) was mixed with 15 µl of the protein solution. The decrease in the light-scattering intensity of the solution was monitored by measuring the absorbance at 600 nm for 100 s at 25 °C using a spectrophotometer (V-630; Japan Spectroscopic Co. Ltd., Tokyo). The decreasing absorbance between 40 to 90 s was fitted to a linear extrapolation; then the enzymatic activity was estimated from the slope of the line, as described previously [30].

## Circular dichroism

Circular dichroism (CD) spectroscopy was performed in a 1 mm pathlength quartz cuvette using a spectropolarimeter (J-720 W; Jasco Corp.). The CD spectra were recorded for 195–260 nm at 25 °C. The Far-UV CD spectra of the samples were corrected by subtracting the corresponding spectra of buffers in the absence of lysozyme.

## Fluorescence measurement

Fluorescence spectra of intrinsic Trp residues of lysozyme were recorded using a spectrofluorometer (FP6500; Jasco Corp., Tokyo, Japan) with excitation wavelength of 295 nm recorded for 315–400 nm at 25 °C. The fluorescence spectra of respective reference solutions with the absence of lysozyme were subtracted from the intensity of the sample solutions. The determined intensities were averages of triplicate experiments.

## Molecular weight measurement

Mass spectra were obtained using MALDI–TOF MS (UltrafleXtreme MALDI-TOF/TOF; Bruker Daltonics Inc., Billerica, USA). Samples were prepared using the uniform submicrometer crystal formation method [31]. The α-cyano-4-hydroxycinnamic acid (CHCA) was saturated in methanol.

The CHCA solution of 1.0 μl was applied to the polished steel probe. The matrix solution used for these measurements was the saturated CHCA solution in water/acetonitrile 1:1 (v/v), diluted by a factor of 2 in the same solvent mixture. The sample, loaded on MALDI–TOF MS, was prepared by mixing 1.0 μl of the protein solution with 1.0 μl of the matrix solution directly on the sample probe and allowing the solution to dry at room temperature.

## SDS–PAGE

After exposure of the plasma jet, the sample was resolved in loading buffer containing 2% (w/v) SDS, 10% glycerol, 0.04 M DTT, 0.01% (w/v) bromophenol blue, and 62.5 mM Tris–HCl (pH 6.8). Samples were boiled for 5 min; then the samples and the standard ladder marker were loaded on 15% polyacrylamide gel. Gel electrophoresis and staining were described previously. The standard marker for SDS–PAGE was obtained from Apro Life Science Institute Inc. (Tokushima, Japan).

# Results

To elucidate the fundamental reactions between atmospheric pressure plasmas and biomacromolecules, protein in aqueous solutions treated by LF plasma jet (Fig. 4.1.1) was studied using lysozyme as a model. The bacteriolysis activity of lysozyme was monitored by the decreasing in absorbance at 600 nm as described previously [32]. Figure 4.1.2 presents the time course of residual activity of lysozyme after treatment of the LF plasma jet for the respective periods. The residual activity decreased with time, about one-third after the plasma treatment for 30 min. To

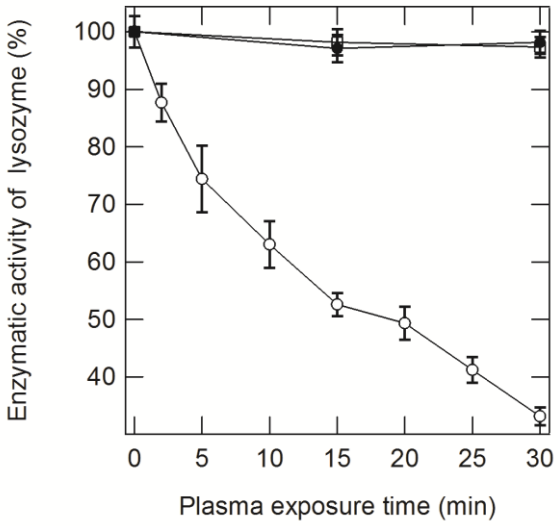


**Figure 4.1.2.** Residual activity of lysozyme in 10 mM phosphate buffer (pH 7) treated by a LF plasma jet in respective periods (open circles), hot air treatment with heat (closed circles), and plasma treatment through a quartz glass plate with UV (open squares).

confirm the cause of inactivation, two control experiments were performed: hot-air treatment and plasma jet treatment through the quartz glass plate [25]. Briefly, hot-air treatment was performed as the control experiment with air at 80 °C instead of LF plasma jet blown on the samples. The plasma treatment through a quartz glass plate was performed as the control experiment that LF plasma jet irradiated on the samples through a UV-permeability glass vial to confirm the effect of UV alone. As expected, the enzymatic activity of lysozyme did not change in these control experiments (Fig. 4.1.2). Moreover, the concentration of lysozyme did not change (data not shown). These data indicate that the decrease in the residual activity results from chemical modification and/or unfavorable denaturation of the enzymes by treatment of LF plasma jet. This report is the first describing that atmospheric plasma decreases the enzymatic activity of protein.

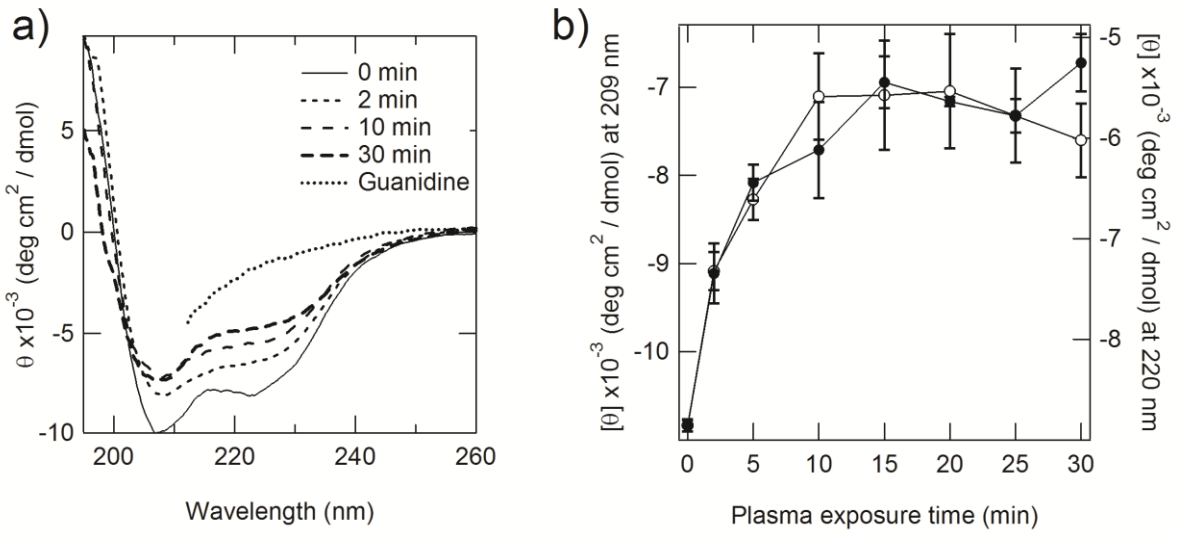


**Figure 4.1.3.** (a) Circular dichroism spectra of lysozyme treated in 10 mM phosphate buffer (pH 7) by LF plasma jet at the respective periods and in 6.0 M Guanidine HCl 10 mM phosphate buffer (pH 7) (untreated by LF plasma jet). (b) Changes in the molar ellipticity at 209 nm (open circles, left axes) and 220 nm (closed circles, right axes) as a function of the plasma exposure time.

To clarify the mechanism of the inactivation of lysozyme by a LF plasma jet, circular dichroism (CD) and fluorescence spectroscopy were conducted, which yielded information about the protein molecular structures. Far-UV CD spectrum is a well-used technique to determine the secondary structure of proteins in solution [33]. Figure 4.1.3 presents far-UV CD spectra of lysozyme. The secondary structure of lysozyme changed slightly upon treatment with the LF plasma jet. The CD spectrum of lysozyme treated of LF plasma jet for 30 min was similar to that of the random coil structure in 6.0 M Guanidine HCl **(**Fig. 4.1.3a). The far-UV ellipticity of lysozyme decreased steeply with time for the plasma treatment and then reached a plateau for 10 min (Fig. 4.1.3b). It is noteworthy that the far-UV CD spectra did not change in the control experiments of hot air (heat) and plasma jet treated through the quartz glass plate (UV) (data not shown). The results indicate that lysozyme is denatured by the plasma treatment. Consequently, the inactivation of

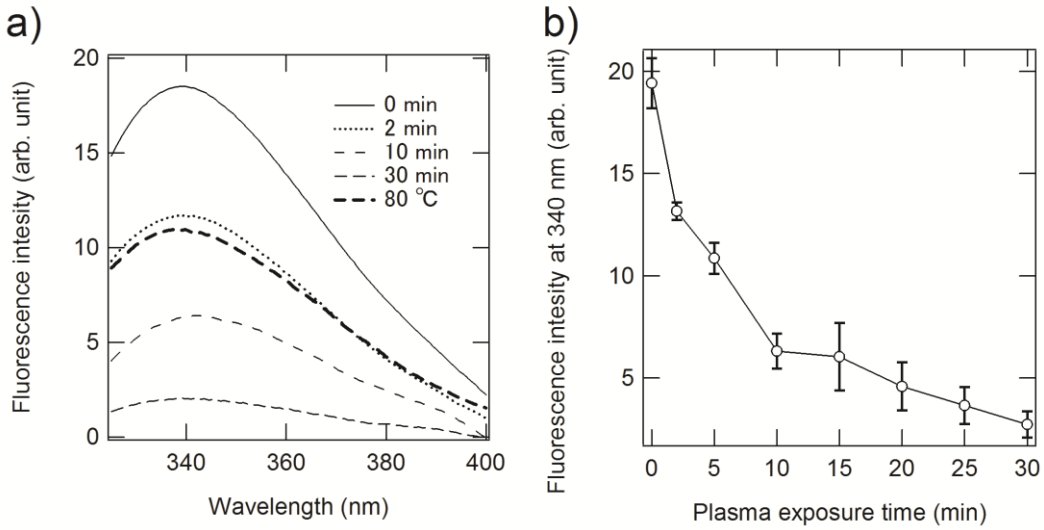


**Figure 4.1.4.** (a) Fluorescence spectra of lysozyme in 10 mM phosphate buffer (pH 7) treated by LF plasma jet at the respective periods and at 80 °C (untreated by LF plasma jet). (b) Changes in the fluorescence intensity at 340 nm in the fluorescence spectra of lysozyme as a function of exposure time.

lysozyme by LF plasma jet results from the structural change of lysozyme.

Figure 4.1.4 shows the intrinsic tryptophan fluorescence of lysozyme after the plasma treatment. Lysozyme from hen egg white shows an intrinsic fluorescence by tryptophan residues with excitation at 295 nm. The fluorescence intensity of lysozyme at 340 nm decreased with the plasma treatment, although the maximum wavelength of the fluorescence spectra did not change. It was also confirmed that the control experiments of both hot air (heat) and plasma treated through quartz glass plate (UV) did not affect the fluorescence spectra (data not shown). It should be noted that the fluorescence intensity at 340 nm with the plasma treatment decreased more than at 80 °C, which is denaturation temperature of lysozyme (Fig. 4.1.4). Because the fluorescence intensity of tryptophan is unaltered in the range of 25-95 °C [34], the decrease in the fluorescence intensity may result from the change of chemical structure of tryptophan by the LF plasma jet.

To investigate the change of chemical structure of lysozyme, mass spectroscopy was performed. Figure 4.1.5a shows data of MALDI–TOF MS of the samples after plasma treatment for 0 or 30 min. The most abundant peak of native lysozyme was m/z 7153, which corresponds to the doubly protonated molecule; the singly protonated molecule shows a peak at a maximum of m/z 14306. A minor species at m/z 28612 was detected, which corresponds to the dimer with one protonation. These MS spectra of lysozyme were coincident with those reported previously [35]. However, the peaks of the MS spectrum after the plasma treatment for 30 min were shifted to high molecular weight (Fig. 4.1.5); plasma-treated lysozyme increased the mass of about 90. These results indicate that the LF plasma jet modifies some amino acid side chains in lysozyme. Further analyses, such as identification of the modified sites, will be performed in future studies.

Reportedly, *E. coli* and *L. citreum* are disinfected effectively by the LF plasma jet in acidic

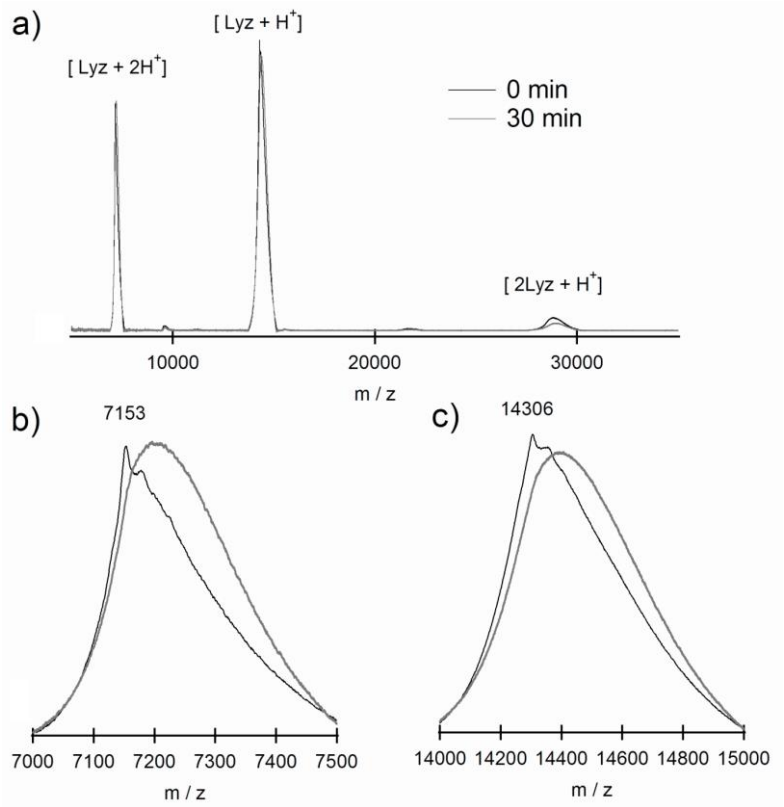


**Figure 4.1.5.** MALDI–TOF MS spectrum of lysozyme treated by a LF plasma jet for 0, 30 min between m/z (a) 5000–35000, (b) 7000–7500, and (c) 14000–15000.

conditions [8]. Consequently, it is interesting to know whether LF plasma jet can inactivate lysozyme at different pH. We investigated the effect of LF jet plasma on the activity and structure of lysozyme as a function of pH. Figure 4.1.6a presents the pH dependence of the inactivation of lysozyme by LF plasma jet for the respective periods in glycine–phosphate buffer at pH 2, 7, and 10. Inactivation was observed while the rates of the inactivation varied with the order of pH 10 > pH 2 > pH 7. Figure 6b,c,d portrays far-UV CD spectra of lysozyme after plasma treatment at pH 2, 7, and 10. As the figures show, the secondary structure was decreased immediately at high pH. It is noteworthy that the isoelectric point of lysozyme is at around pH 10; the condition at pH 10 is prone to aggregate lysozyme[36]. Consequently, the inactivation of the alkaline condition might be related to the aggregation. However, the rate of inactivation and structural change at pH 2 was higher than that at pH 7. The results indicate that the inactivation in acidic conditions might be predominantly attributable to chemical modification of the amino acid side chains of lysozyme.

# Discussion

As described in this paper, LF plasma jet, an LTAP plasma, was applied to lysozyme as a model enzyme in aqueous solution (Fig. 4.1.1). The following experimentally obtained results were

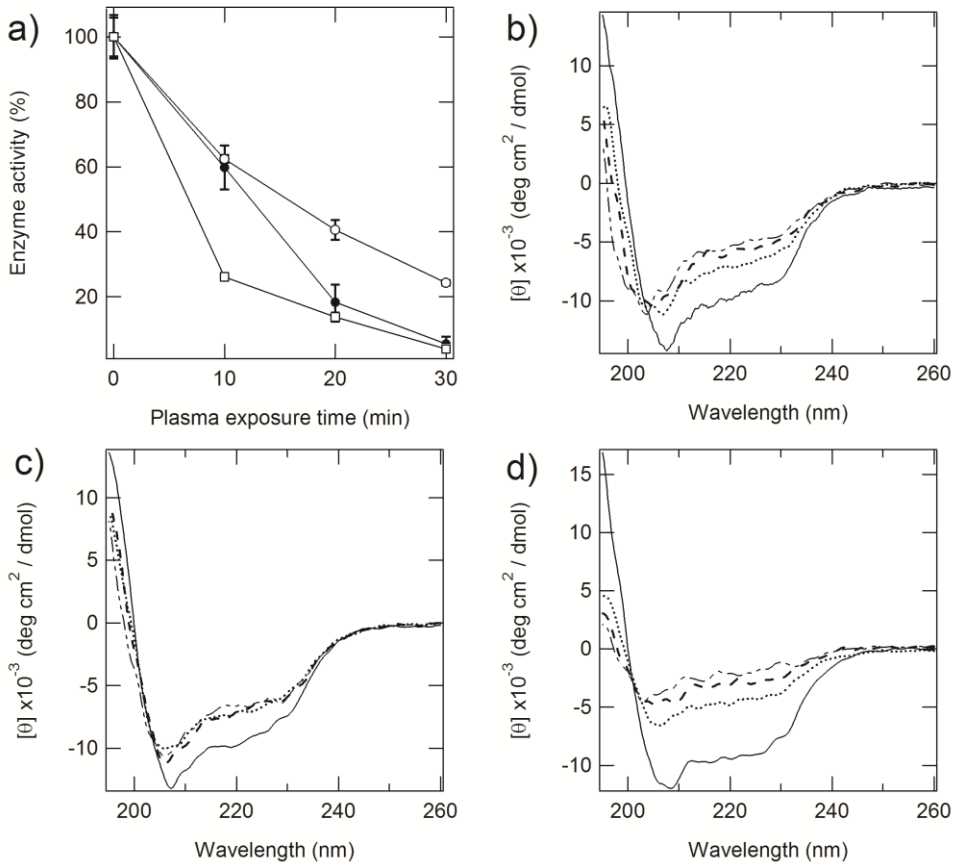


**Figure 4.1.6.** (a) Residual activities of lysozyme treated by a LF plasma jet in 10 mM glycine-phosphate buffer at pH 2 (closed circles), pH 7 (open circles), or pH 10 (open squares). Circular dichroism spectra of lysozyme treated by a LF plasma jet for 0 min (continuous line), 10 min (dotted line), 20 min (broken line), or 30 min (dot-broken line) at pH 2 (b), pH 7 (c), or pH 10 (d).

observed from plasma treatment: (i) decreased enzymatic activity (Fig. 4.1.2), (ii) change in the secondary structure (Fig. 4.1.3), (iii) decrease of the tryptophan fluorescence intensity (Fig. 4.1.4), and (iv) increased molecular weight (Fig. 4.1.5). Inactivation and structural change of lysozyme were affected by the pH value of the solution (Fig. 4.1.6). These effects of LF plasma jet on lysozyme are caused neither by UV light nor heat from plasma, suggesting that the reactive species generated by LF plasma jet affect lysozyme. One possible mechanism of LF plasma jet on protein is that hydroxyl radicals (OH·), superoxide anion radicals (O2-·), hydroperoxy radicals (HOO·), and nitric oxide (NO·) result in the chemical modifications of chemically-reactive side-chain of the amino acids, such as cysteine, aromatic rings of phenylalanine, tyrosine, and tryptophan. Further experiments should be performed to clarify the chemical and physiological influences of LF plasma jet on biological molecules.

Inactivation of lysozyme by LF plasma jet was observed in this paper. It is noteworthy that these data apparently differ from those obtained by He-Ping and co-workers using lipase; the enzymatic activity of lipase increased by LTAP plasma within one minute[29]. This is not surprising because the activity of lipase is enhanced in the presence of low concentrations of organic solvents;

the percentages of activity are 150 % in 1.25 % butanol and 130 % in 0.25 % butyric acid[37]. Consequently, the structural artifacts affect the enzymatic activity of lipase by the plasma. We believe that LTAP plasma generally decreases the enzymatic activity of soluble proteins because lysozyme is a typical enzyme with a small and monomeric structure in water-soluble form. The hypothesis is consistent with the other two facts that LTAP plasma inactivates infectious prion proteins [28] and recombinant GFP without affecting peptide bonds [14].

The molecular mechanism of the lysozyme inactivation can be described as follows. It is noteworthy that enzymatic activity and denaturation depend on pH (Fig. 4.1.6). Inactivation at pH 10 results from aggregation at around net charges of lysozyme in the solution [35]. However, the cause of inactivation at acidic pH is not elusive: it is not intermolecular aggregation, but chemical modification of lysozyme. Ikawa et al. recently reported that LF plasma jet sterilizes bacteria effectively at pH less than 4.8, resulting from hydroperoxy radical and superoxide anion radical[8]. This is true because p*K*a of the equilibrium reaction between the superoxide anion radical and hydroperoxy radicals is known to occur at approximately pH 4.8 [38]. Consequently, inactivation at acidic pH might be different from that at alkaline pHs because of their radical species.

In summary, this paper revealed that LTAP plasma decreases the enzymatic activity of lysozyme and increases the molecular weight of the protein. This study is a first report to elucidating chemical reaction and structural change of protein by the plasma in aqueous solution. These data imply the interesting application that LF plasma jet solubilizes aggregates of protein, typically amyloid fibrils. Actually, it was recently reported that atmospheric pressure plasma dissolved amyloid fibrils in dry condition [39,40]. It is noteworthy that LF plasma jet dissolved amyloid fibrils of lysozyme (data not shown); details of this effect will be described in future reports.

# References


[1] Mariotti D, Sankaran RM 2010 Microplasmas for nanomaterials synthesis *J. Phys. D: Appl. Phys.* **43** 323001

[2] Garcia-Reyes JF, Mazzoti F, Harper JD, Charipar NA, Oradu S, Ouyang Z, Sindona G, Cooks RG 2009 Direct olive oil analysis by low‐temperature plasma (LTP) ambient ionization mass spectrometry *Rapid Commun. Mass Spectrom.* **23** 3057–3062.

[3] Harper JD, Charipar NA, Mulligan CC, Zhang X, Cooks RG, Ouyang R 2008 Low-temperature plasma probe for ambient desorption ionization *Anal. Chem.* **80** 9097–9104.

[4] Kylian O, Rauscher H, Denis B, Ceriotti L, Rossi F 2009 Elimination of Homo‐polypeptides of Amino Acids from Surfaces by means of Low Pressure Inductively Coupled Plasma Discharge *Plasma Process. Polym.* **6** 848–854.

[5] Lee HW, Nam SH, Mohamed A-AH, Kim GC, Lee JK 2010 Atmospheric pressure plasma jet composed of three electrodes: Application to tooth bleaching *Plasma Process. Polym.* **7** 274–280.

[6] Feng H, Wang R, Sun P, Wu H, Liu Q, Fang J, Zhu W, Li F, Zhan J 2010 A study of eukaryotic response mechanisms to atmospheric pressure cold plasma by using Saccharomyces cerevisiae single gene mutants *Appl. Phys.*

*Lett.* **97** 131501.

[7] Ehlbeck J, Schnabel U, Polak M, Winter J, Woedtke T, Brandenburg R, Hagen T, Weltmann K-D 2011 Low temperature atmospheric pressure plasma sources for microbial decontamination *J. Phys. D: Appl. Phys.* **44** 013002.

[8] Ikawa S, Kitano K and Hamaguchi S 2010 Effects of pH on Bacterial Inactivation in Aqueous Solutions due to Low-Temperature Atmospheric Pressure Plasma Application *Plasma Processes and Polymers* B 33-42

[9] Bussiahn R, Brandenburg R, Gerling T, Kindel E, Lange H, Lembke N, Weltmann K D, von Woedtke T and Kocher T 2010 The hairline plasma: An intermittent negative dc-corona discharge at atmospheric pressure for plasma medical applications *Appl. Phys. Lett.* **96** 143701

[10] Perni S, Shama G, Hobman J L, Lund P A, Kershaw C J, Hidalgo-Arroyo G A, Penn C W, Deng X T, Walsh J L and Kong M G 2007 Probing bactericidal mechanisms induced by cold atmospheric plasmas with Escherichia coli mutants *Appl. Phys. Lett.* **90** 073902

[11] Kolb J F, Mohamed A A H, Price R O, Swanson R J, Bowman A, Chiavarini R L, Stacey M and Schoenbach K H 2008 Cold atmospheric pressure air plasma jet for medical applications *Appl. Phys. Lett.* **92** 241501

[12] Laroussi M, Leipold F 2004 Evaluation of the roles of reactive species, heat, and UV radiation in the inactivation of bacterial cells by air plasmas at atmospheric pressure *Int. J. Mass Spectrom.* **233** 81–86.

[13] Muranyi P, Wunderlich J, Heise M 2007 Sterilization efficiency of a cascaded dielectric barrier discharge *J. Appl. Microbiol.* **103** 1535-1544.

[14] Yasuda H, Hashimoto M, Rahman MM, Takashima K, Mizuno A 2008 States of biological components in bacteria and bacteriophages during inactivation by atmospheric dielectric barrier discharges *Plasma. Process. Polym.* **5** 615–621.

[15] Kim SJ, Chung TH, Bae SH, Leem SH 2009 Characterization of atmospheric pressure microplasma jet source and its application to bacterial inactivation *Plasma. Process. Polym.* **6** 676–685.

[16] Scholtz V, Julak J, Kriha V 2010 The Microbicidal Effect of Low-Temperature Plasma Generated by Corona Discharge: Comparison of Various Microorganisms on an Agar Surface or in Aqueous Suspension *Plasma. Process. Polym.* **7** 237–243.

[17] Daeschlein G, Woedtke T, E. Kindel, Brandenburg R, Weltmann KD, Junger M 2010 Antibacterial activity of an atmospheric pressure plasma jet against relevant wound pathogens in vitro on a simulated wound environment *Plasma. Process. Polym.* **7** 224–230.

[18] Liu F, Sun P, Bai N, Tian Y, Zhou H, Wei S, Zhou Y, Zhang J, Zhu W, Becker K, Fang J 2010 Inactivation of Bacteria in an Aqueous Environment by a Direct‐Current, Cold‐Atmospheric‐Pressure Air Plasma Microjet *Plasma. Process. Polym.* **7** 231–236.

[19] Lim JP, Uhm HS, Li SZ 2007 Influence of oxygen in atmospheric-pressure argon plasma jet on sterilization of Bacillus atrophaeous spores *Phys. Plasmas.* **14** 093504.

[20] Ohkawa H, Akitsu T, Tsuji M, Kimura H, Kogoma M, Fukushima K 2006 Pulse-modulated, high-frequency plasma sterilization at atmospheric-pressure *Surf. Coat. Technol.* **200** 5829–5835.

[21] Ekem N, Akan T, Akgun Y, Kiremitci A, Pat S, Musa G. 2006 Sterilization of Staphylococcus aureus by atmospheric pressure pulsed plasma *Surf. Coat. Technol.* **2001** 993–997.

[22] Akitsu T, Ohkawa H, Tsuji M, Kimura H, Kogoma M 2006 Pulse-modulated, high-frequency plasma

sterilization at atmospheric-pressure *Surf. Coat. Technol.* **193** 5829–5835.

[23] Yu H, Perni S, Shi JJ, Wang DZ, Kong MG, Shama G 2006 Effects of cell surface loading and phase of growth in cold atmospheric gas plasma inactivation of Escherichia coli K12 *J. Appl. Microbiol.* **101** 1323–1330.

[24] Yan X, Zou F, Lu X P, He G Y, Shi M J, Xiong Q, Gao X, Xiong Z L, Li Y, Ma F Y, Yu M, Wang C D, Wang Y S and Yang G X 2009 Effect of the atmospheric pressure nonequilibrium plasmas on the conformational changes of plasmid DNA *Appl. Phys. Lett.* **95** 083702

[25] Li G, Li H P, Wang L Y, Wang S, Zhao H X, Sun W T, Xing X H and Bao C Y 2008 Genetic effects of radio-frequency, atmospheric-pressure glow discharges with helium *Appl. Phys. Lett.* **92** 221504.

[26] Deng XT, Shi JJ, Kong MG 2008 Protein destruction by a helium atmospheric pressure glow discharge: Capability and mechanisms *J. Appl. Phys.* **101** 074701.

[27] Deng XT, Shi JJ, Chen HL, Kong MG 2007 Protein destruction by atmospheric pressure glow discharges *Appl. Phys. Lett.* **90** 013903.

[28] Julák J, Janoušková O, Scholtz V, Holada K 2011 Inactivation of Prions Using Electrical DC Discharges at Atmospheric Pressure and Ambient Temperature *Plasma. Process. Polym.* **8** 316-323

[29] Li HP, Wang LY, Li G, Jin LH, Le PS, Zhao HX, Xing XH, Bao CY 2011 Manipulation of Lipase Activity by the Helium Radio‐Frequency, Atmospheric‐Pressure Glow Discharge Plasma Jet *Plasma. Process. Polym.* **8** 224–229.

[30] Matsuoka T, Tomita S, Hamada H, Shiraki K 2007 Amidated amino acids are prominent additives for preventing heat-induced aggregation of lysozyme *J. Biosci. Bioeng.* **103** 440–443.

[31] Dai YQ, Whittal RM, Li L 1996 Two-layer sample preparation: a method for MALDI-MS analysis of complex peptide and protein mixtures *Anal. Chem.* **68** 2494–2500.

[32] Ibrahim HR, Higashiguchi S, Juneja LR, Kim M, Yamamoto T 1996 A structural phase of heat-denatured lysozyme with novel antimicrobial action *J. Agric. Food Chem.* **44** 1416-1423.

[33] Johnson Jr WC 1988 Secondary structure of proteins through circular dichroism spectroscopy *Ann. Rev. of Biophys. Biophys. Chem.*, **17** 145-166

[34] Gallya JA, Edelmana GM 1962 The effect of temperature on the fluorescence of some aromatic amino acids and proteins *Biochimica. et. Biophysica. Acta*,. **60** 499-509.

[35] Lapolla A, Fedele D, Aronica R, Baldo L, D'Alpaos M, Seraglia R, Traldi P 1996 The in vitro glycation of lysozyme and the influence of buffer concentration investigated by mass spectrometry *Rapid Commun. Mass Spectrom* **10** 1512–1518.

[36] Tomita S, Yoshikawa H, Shiraki K 2011 Arginine controls heat‐induced cluster‐cluster aggregation of lysozyme at around the isoelectric point *Biopolymers* **95** 695-701

[37] Otero C, Ballesteros A, Guisan JM 1988 Immobilization/stabilization of lipase fromCandida rugosa *Appl. Biochem. Biotechnol* **19** 163–175.

[38] Winterbourn CC, Hampton MB, Livesey JH, Kettle AJ 2006 Modeling the Reactions of Superoxide and Myeloperoxidase in the Neutrophil Phagosome *J. Biol. Chem.* **281** 39860–39869.

[39] Karakas E, Munyanyi A, Greene L and Laroussi M 2010 Destruction of alpha-synuclein based amyloid fibrils by a low temperature plasma jet *Appl. Phys. Lett.* **97** 143702

[40] Bayliss D L, Walsh J L, Shama G, Iza F and Kong M G 2009 Reduction and degradation of amyloid aggregates

by a pulsed radio-frequency cold atmospheric plasma jet *New Journal of Physics* **11** 115024

## 4.2 Synergistic Solubilization of Porcine Myosin in Physiological Salt Solution by Arginine

# Introduction

Meat is rich in high-quality proteins and contains all of the essential amino acids for humans [1]. However, meat has not been fully utilized as a protein supplement to the same extent that milk or soybean products have been utilized because of the low solubility of myosin, which constitutes approximately 50 % of myofibrillar proteins. The low solubility of myosin results from the spontaneous formation of filaments that occur in vivo [2–4]. Myosin is practically insoluble in aqueous solution at low ionic strength but is increasingly soluble at high salt concentrations [5–9].

Solubilization of insoluble myosin has been achieved by adding 5 mM histidine in low ionic strength solutions (1-5 mM KCl, pH 7.5) [10–12]. The mechanism by which histidine solubilizes myosin appears to involve structural changes in monomeric myosin and the resulting inhibition of native myosin filament formation [11]. When the salt concentration is increased to a physiological level (0.15 M), 5 mM histidine no longer shows such effects [12]. Considering the observed structural changes caused by histidine, which may limit myosin application, it would be advantageous to achieve high myosin solubility without structural changes even in physiological salt solutions. We have investigated several additives, including histidine and arginine, for their effects on myosin solubility as a function of salt concentration and on the myosin structure.

Arginine is one of the most common solvent additive that suppress protein aggregation without altering or destabilizing the tertiary structure of the proteins [13,14]. Arginine has been used in various applications, including suppression of reductant- or heat-induced aggregation [15–18], enhancement of protein refolding [17–22], crystallization [23], and improved performance of column chromatography [24–27]. The molecular mechanisms by which arginine suppresses protein aggregation have been proposed: (i) the guanidinium group of arginine interacts with aromatic residues by cation-π interactions [28–31], which has been observed in the enhanced solubility of aromatic compounds [32,33], and (ii) weak preferential exclusion of arginine from the protein surface, which is associated with its weak binding to the proteins and increases the activation energy toward aggregation [34,35]. Thus, we have focused on the solubilization effects of arginine and its influence on myosin structure.

# Materials and methods

## Materials

Sodium chloride (NaCl) and sodium phosphate were obtained from Nacalai Tesque Inc. (Tokyo, Japan). L-arginine hydrochloride (Arg), glycine (Gly), L-histidine (His), L-lysine hydrochloride (Lys) and guanidine hydrochloride (Gdn) were obtained from Wako Pure Chemical Ind., Ltd. (Osaka, Japan). All chemicals used were of reagent grade and were used as received.

## Purification of myosin

Porcine myosin extract was prepared as follows: myosin was extracted from 120 g of lean porcine meat from the inner thigh (semitendinosus) with 450 ml of buffer containing 100 mM pyrophosphate and 5.0 mM MgCl2 (pH 7.0) using a homogenizer at 5 °C for 60 min. The myosin extract was stored at -25 °C. After thawing at room temperature, the myosin extract was dialyzed against 1.0 mM KCl and 2.0 mM Na-phosphate buffer (pH 7.0). The precipitates of the dialyzed solution were washed with 1.0 mM KCl and 2.0 mM Na-phosphate buffer (pH 7.0) and were used as the source of myosin. SDS-PAGE analysis of the prepared myosin was shown in Figure 4.2.1.


**Figure. 4.2.1.** SDS-PAGE analysis of the prepared myosin. Lane 1: The standard ladder. Lane 2: The myosin dissolved with 50 mM NaCl and 20 mM sodium phosphate buffer (pH 7.5). The filament formed and monomeric myosin is indicated by the red and black arrows, respectively.

## Preparation of myosin solution

The frozen myosin extract (72 mg) was dissolved with 20 mM sodium phosphate buffer containing 1 M NaCl (pH 7.5). After incubation for 1 hour at 25 °C, the myosin solution was centrifuged at 18,800 ×$g$ for 20 min. After centrifugation, the supernatant containing 1 M NaCl was used as the stock myosin solution. As previously reported, myosin was highly soluble and stable in this solvent,

which was largely in the monomeric structure [5,6].

## Measurement of myosin solubility

The stock myosin solution was diluted from 20 mM sodium phosphate buffer and 1 M NaCl (pH 7.5) into the test solvents for a final concentration of 50 mM additives (Arg, Lys, NaCl, His, Gly and Gdn) in the presence of 0.05-0.3 M NaCl in the same buffer. The sample solution was incubated for 1 hour at 25 °C and centrifuged at 18,800 ×*g* for 20 min. The supernatant was diluted 10-fold with the respective buffer to reduce the myosin concentration for the fluorescence measurements. The myosin concentration in the supernatant, which corresponds to the solubility, was measured using a fluorescence spectrofluorometer (FP-6500, Jasco Corp.; Tokyo, Japan) with a 1-cm path-length quartz cuvette. The solution was excited at 280 nm (3 nm slit-width), and the emission spectrum (5 nm slit-width) was collected at 25 °C.

## Circular dichroism (CD) spectra

Far-UV circular dichroism (CD) measurements were performed on a spectropolarimeter (J-720W; Jasco Corp.) using a 1-mm path-length quartz cuvette. The CD spectra of the sample myosin solutions were measured at 25 °C. The CD spectra of the samples were corrected by subtracting the spectra of the respective solvents.

## SDS–PAGE

The prepared myosin sample was resolved in loading buffer containing 2% (w/v) SDS, 10% (w/v) glycerol, 0.04 M DTT, 0.01% (w/v) bromophenol blue, and 62.5 mM Tris–HCl (pH 6.8). The samples were boiled for 5 min; then the samples and the standard ladder marker were loaded on 15% polyacrylamide gel. The standard marker for SDS–PAGE was obtained from Apro Life Science Institute Inc. (Tokushima, Japan).

# Results

## Measurement of myosin concentration by fluorescence intensity

The concentration of myosin in the test solvents was determined by the intrinsic tryptophan fluorescence of myosin as opposed to the absorbance at 280 nm. This approach was used because the formation of filamentous structures causes significant light scattering and makes UV absorbance unreliable for concentration determination. Figure 4.2.2 demonstrates the reliability of fluorescence

for myosin concentration measurements. Figure 4.2.2A shows the fluorescence emission spectra of a serially diluted myosin stock solution of known protein concentration. The spectral shape was independent of dilution with a peak at 334 nm, which indicated no effects of dilution and protein concentration on the tryptophan environments of myosin; note that this fluorescence peak position indicates that the fluorescent tryptophans are at least partially buried inside the tertiary structure of myosin. The fluorescence intensity at 334 nm of these myosin samples were plotted against the concentration of myosin. As shown in Fig. 4.2.2B, the fluorescence intensity linearly increased with the sample concentration. The straight line corresponds to a linear regression with a correlation coefficient of 0.999. Thus, the myosin concentration can be reliably determined from the fluorescence intensity at 334 nm. Furthermore, the fluorescence spectra of myosin were not affected by the additives tested and NaCl concentrations (date not shown).

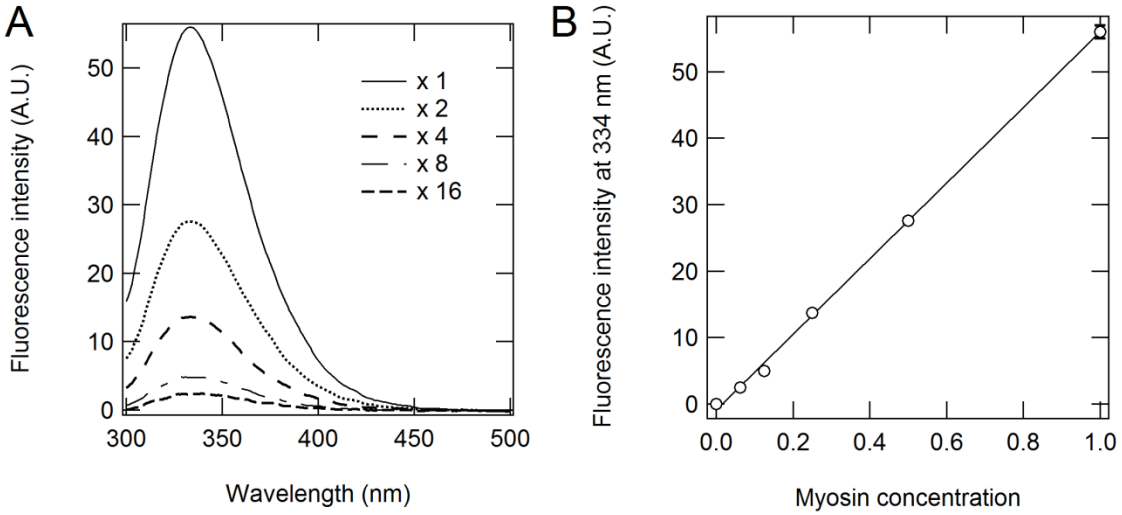


**Figure. 4.2.2.** (A) The intrinsic emission fluorescence spectra of myosin at different protein concentrations. The stock sample solution was serially diluted (1- to 16-fold) with 20 mM sodium phosphate (pH 7.5). The fluorescence emission spectra were collected at 25 °C with an excitation wavelength of 280 nm. (B) The fluorescence intensity at 334 nm against myosin concentrations. Data are taken from Fig. 1A. The plot was fit by linear regression with a correlation coefficient of 0.999. The measurements were performed three times, and the error bars depict the standard deviation of the mean.

## Effect of arginine on myosin solubility

Figure 4.2.2 shows the effects of 50 mM Arg, Lys, NaCl, His, Gly and Gdn on the solubility of myosin in the presence of NaCl concentrations (50, 100, 150, 200, 250 and 300 mM); note that an additional 50 mM NaCl was present over the basal NaCl concentration (a total of 100 mM NaCl for the first column, which corresponds to the 50 mM basal NaCl concentration). The myosin solubility in the absence of an additional 50 mM NaCl (at the basal salt concentration) is shown as “none” in

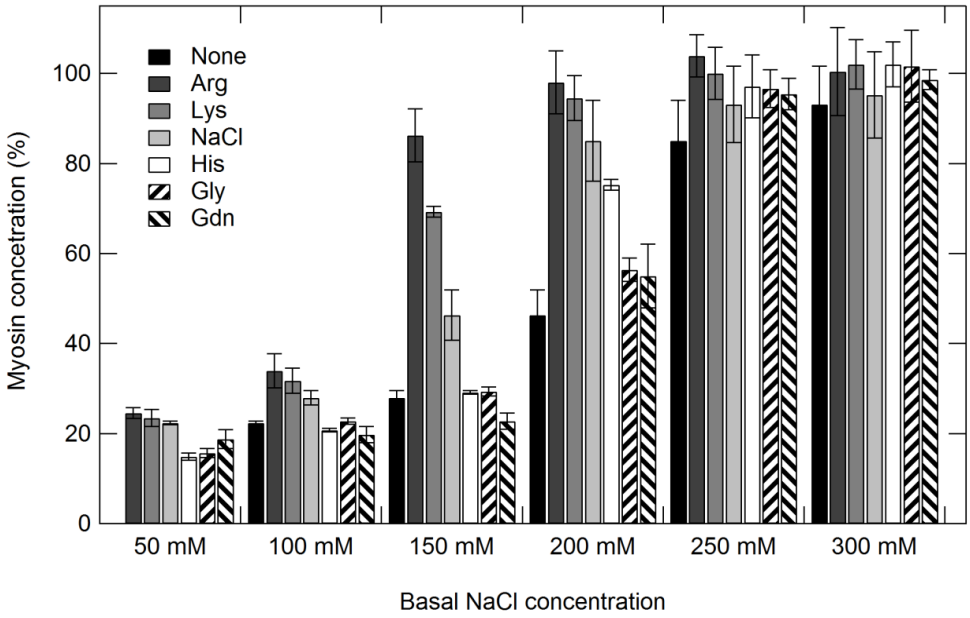


**Figure. 4.2.3.** Myosin solubility in 50 mM additives or "None" indicated in the figure as a function of basal NaCl concentration. A stock myosin solution in 1 M NaCl was diluted into the test solvents and incubated for 1 h. The concentration of myosin in 50 mM additives or "None" in the presence of 50-300 mM NaCl was determined by measuring the intrinsic fluorescence intensity at 334 nm. The myosin solubility in test solvents was normalized to the value in 50 mM Arg and 300 mM NaCl, which was set as 100 %. The measurements were performed three times, and the error bars depict the standard deviation of the mean.

Fig. 4.2.3. As described in the methods section, the myosin solubility was determined in the test solvents by diluting the stock myosin solution in 1 M NaCl, where myosin is largely monomeric, into the test solvents. Thus, myosin filament formation may vary depending on the salt concentration, which suggests that more filaments may be present at lower salt concentrations. The solubility shown in Fig. 4.2.3 is the value at 1 hour after dilution and may not be the final equilibrium value, particularly in the presence of 50 mM Arg (for reasons described later).

At the 50 mM basal NaCl concentration (first column in Fig. 4.2.3), 50 mM Arg and Lys showed insignificant effects on myosin solubility compared with 50 mM NaCl (total 100 mM NaCl), whereas 50 mM His and Gly slightly reduced myosin solubility compared with the three additives. It is interesting that 50 mM Gdn showed reduced myosin solubility, although only slightly. Thus, the effects of these five additives (i.e., Arg, Lys, His, Gly and Gdn) were marginal at this low basal salt concentration. A small but significant effect of 50 mM Arg was observed at a 100 mM NaCl concentration (second column in Fig. 4.2.3). Arg and Lys increased the myosin solubility compared to NaCl alone, and Arg was more effective; 50 mM NaCl was slightly effective when compared with its absence (see "none"). At this NaCl concentration (second column in Fig. 4.2.3), 50 mM His, Gly and Gdn were essentially ineffective as myosin solubility in these solvents was nearly identical to the solubility in 100 mM NaCl alone ("none"). At a 150 mM NaCl concentration (third column in

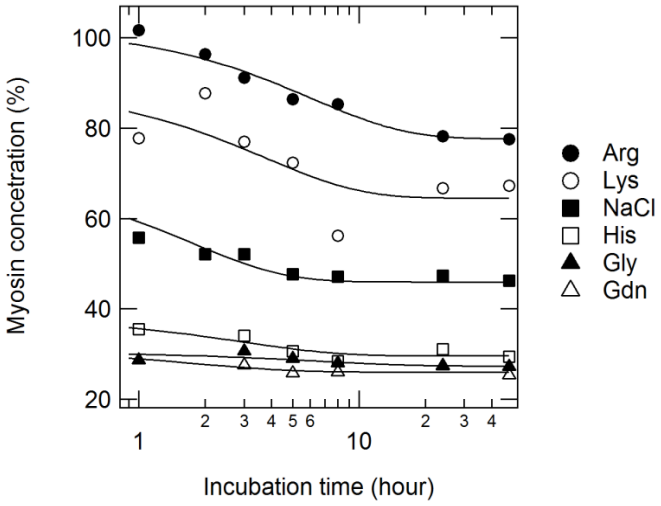


**Figure. 4.2.4.** Time course of concentration changes of myosin. The concentration of myosin in 50 mM additives in the presence of 150 mM NaCl was followed with incubation for 1 hour after dilution into the test solvents. The continuous line though the data points is a fit with a double exponential with offset.

Fig. 4.2.3), a much stronger effect of Arg was observed. At this NaCl concentration, 50 mM Arg increased the myosin solubility by more than twofold over the level achieved by 50 mM NaCl (200 mM total NaCl) and almost threefold over the value at 150 mM NaCl (see first black bar, "none"). Lys was also effective; however, its effect was greatly reduced when compared to Arg. At 150 mM NaCl, 50 mM His, Gly and Gdn were much weaker than NaCl in solubilizing myosin and nearly identical to the value in the absence of 50 mM salt (but in the presence of 150 mM salt). The lack of solubilization effects of His at 150 mM NaCl is consistent with previous reports [12]. When the basal salt concentration was increased to 200 mM (fourth column in Fig. 4.2.3), the solubilization effect of 50 mM NaCl (total 250 mM NaCl) overwhelmed the additive effects, which is seen as the large difference between 200 mM salt (first black bar, "none") and 250 mM salt (fourth dotted bar). The solubility of myosin at 250 mM total NaCl was only slightly less than Arg and Lys. At 200 mM NaCl, 50 mM His was as effective as 50 mM NaCl, whereas Gly and Gdn were significantly less effective. At 250 and 300 mM NaCl (fifth and sixth column in Fig. 4.2.3), the high salt concentration essentially determined the myosin solubility, which became independent of the additives tested.

The solubility experiments were performed by diluting a myosin stock solution in 1 M NaCl. Upon dilution into the test solvents, the myosin should spontaneously form filaments depending on the NaCl concentration and presence of additives until reaching a monomer/filament equilibrium, i.e., equilibrium solubility. Immediately after dilution, the myosin solubility may be much higher in the test solvents than the final equilibrium solubility. Namely, the initial myosin solution is supersaturated with myosin monomer. Thus, the time course of myosin solubility was followed immediately after dilution of the stock solution. Figure 4.2.4 shows the myosin solubility

changes with time in the presence of 50 mM additive and a NaCl concentration of 150 mM. There appeared to be no significant differences in myosin solubility at 1 hour or 45 hours after dilution in the presence of 50 mM Gly and Gdn, which indicates the establishment of solubility equilibrium within 1 hour. Thus, myosin filaments were rapidly formed in these solvents. There appeared to be a slight time dependence of myosin solubility in 50 mM His, which reached equilibrium approximately 5 hours after dilution. The initial solubility of ~35 % reached a plateau value of ~30 % at approximately 5 hours. Although the solubility was greater in 50 mM NaCl (total 200 mM) than in 50 mM His, the time to reach equilibrium was similar, which was determined to be 5 hours by double exponential fitting (initial solubility of 60 % to ~55 % after 5 hours). Compared to the above test solvents, an increased delay in reaching equilibrium was observed in 50 mM Arg and Lys. The myosin solubility in 50 mM Arg decreased after 9 hours of incubation from 85 % to a plateau value of 78 %. It appeared that the solubility equilibrium was attained after approximately 24 hours, which was determined by curve fitting. Because of large data scattering for 50 mM Lys, there was ambiguity in the data fitting, and approximately 10 hours was estimated for the solution to reach equilibrium.

## Effect of arginine on myosin structure

Previously, His has been shown to increase the myosin solubility in low ionic strength solutions by altering the structure of myosin [11]. Thus, we examined whether such structural changes occur in

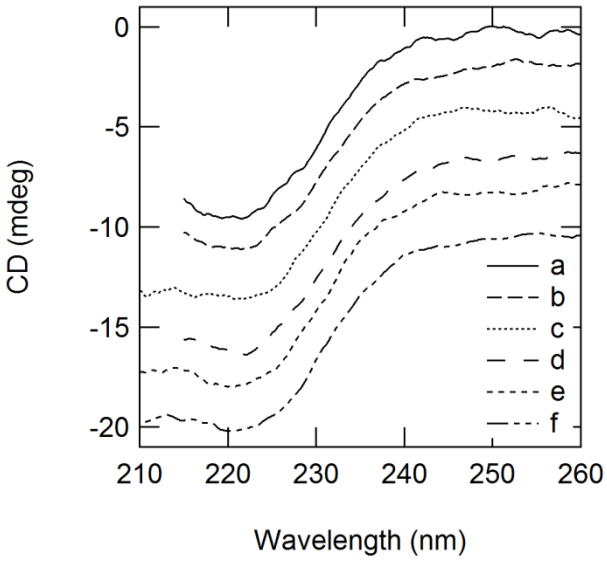


**Figure. 4.2.5.** Far-UV CD spectra of myosin in the presence of Arg or Lys as a function of NaCl concentration. The far-UV CD spectra were measured in 50 mM additives (Arg, Lys and NaCl) in the presence of 150-300 mM NaCl. Each CD spectrum was shifted downward by 2 mdeg for visual comparison. a: 50 mM Arg/150 mM NaCl; b: 50 mM Arg/200 mM NaCl; c: 50 mM Lys/200 mM NaCl; d: 50 mM Arg/300 mM NaCl; e: 50 mM Lys/300 mM NaCl; f: 350 mM NaCl.

Arg and Lys, which clearly enhanced the myosin solubility at 150 mM NaCl. We examined the secondary structure of myosin in 50 mM Arg or Lys at 150-300 mM NaCl. Figure 5 shows the CD spectra of myosin solubilized in 50 mM Arg or Lys at 0.15-0.30 M NaCl. As a control, the CD spectrum was collected in 350 mM NaCl. All CD spectra of myosin were identical within experimental errors, which indicate that an identical myosin structure in the presence of 50 mM Arg or Lys with 50-300 mM NaCl or in the presence of 350 mM NaCl was present, and suggests a different solubilization mechanism for Arg and Lys compared to His.

# Discussion

Myosin forms filamentous structures at low salt concentrations, which makes it practically insoluble in water or dilute salt solutions [5]. His at 5 mM has been shown to increase myosin solubility in low salt solutions and is accompanied by structural changes [11]. Here, we tested the effects of 50 mM Arg, Lys, NaCl, His, Gly and Gdn on myosin solubility in the presence of NaCl at different concentrations (50 to 300 mM). The solubility experiments were performed by diluting a stock myosin solution in 1 M NaCl, in which myosin is largely monomeric [5,6], which we confirmed. Assuming that the monomeric myosin is soluble at low and high salt concentrations, it is the formation of filaments that determine the myosin solubility; thus, the protein precipitates are composed wholly of filaments and not the monomers. This finding indicates that the effects of the test solvents on myosin solubility are the results of their effects on the monomer-filament equilibrium. Marginal solubilization effects of all additives tested were observed in the presence of 50 and 100 mM NaCl, unlike the observed solubilization of His in dilute salt solutions, which suggest that the effects of Arg, Lys and other additives are mechanistically different from those of His. Marginal solubilization effects of Arg and Lys at 50-100 mM NaCl may be because of the strong tendency of myosin to self-associate into the filaments at low salt concentrations. When the tendency for self-association becomes weaker at increasing salt concentrations (150-200 mM), the solubilization effects of Arg and Lys are more apparent. Further increases in the salt concentration (250-300 mM) highly favor monomeric myosin, and the effects of the additives are overwhelmed by salt effects on self-association. Thus, the interaction of these additives with myosin (most likely monomeric myosin) that affects myosin solubility may be altered by the presence of salt and may depend on the salt concentration.

Regardless of the solubilization mechanism, two basic amino acids, Arg and Lys, are more effective than His and Gly. As His and Gly are neutral in net charge at the experimental pH of 7.5, a net positive charge (or positively charged side chain) appears to play a role in their interaction with myosin and effects myosin solubility. Electrostatic interactions have been shown to be involved in myosin-myosin interactions in the formation of the filamentous structures [36]. It is expected that high salt concentrations disrupt electrostatic interactions and prevents filament formation, which is

observed by the high myosin solubility. A specific interaction of the Arg or Lys cation with myosin may also disrupt the electrostatic interactions more effectively than NaCl, which increases the myosin solubility over the solubility achieved by salt alone. Arg was always more effective than Lys, which indicates that the positive charge and structure of the side chain play a role. The critical role of the guanidinium group has been implicated in the effectiveness of Arg in the suppression of protein aggregation [17,18]. The guanidinium group alone was insufficient in myosin solubilization, which was shown by the lack of increased solubilization effects because of Gdn. Under the experimental conditions, His displayed no or marginal solubilization effects, which differed from previously reported results [10–12] . Such His effects were attributed to the structural changes of myosin conferred by His [11], which indicates that His has no effect on myosin structure under the present experimental conditions. Further, the effects of Arg and Lys are mediated by their interaction with native myosin, which was indicated by the lack of structural changes.

Interestingly, the equilibrium solubility was attained extremely slowly in the presence of 50 mM Arg with 150 mM NaCl, which took more than 20 hours after dilution of the stock myosin solution in this solvent. Namely, self-association of the myosin monomer to the filaments was slow in this solvent system. The rate of this transition from monomer to filament becomes faster in Lys and further in NaCl. In Gly and Gdn, the transition appeared to occur within one hour. Myosin is in a monomeric structure in 1 M NaCl [5,6]. Upon dilution into 50 mM Gly or Gdn in 150 mM NaCl, the solubility of myosin rapidly reaches equilibrium, which means a low activation energy of the monomer-filament transition. In the presence of 50 mM Arg, the initial solubility is much higher than the equilibrium solubility (~100 % vs. < 80 %). Arg increases the activation energy. Because of this high energy barrier, the supersaturated myosin solution is kinetically stabilized by Arg. The binding of Arg to monomeric myosin may be involved in the stabilization of the monomer as the free energy to dissociate the bound Arg should increase the energy barrier.

In conclusion, Arg increased the equilibrium solubility and activation energy of self-association of monomeric myosin in a physiological salt solution (Fig. 4.2.6). This stabilization

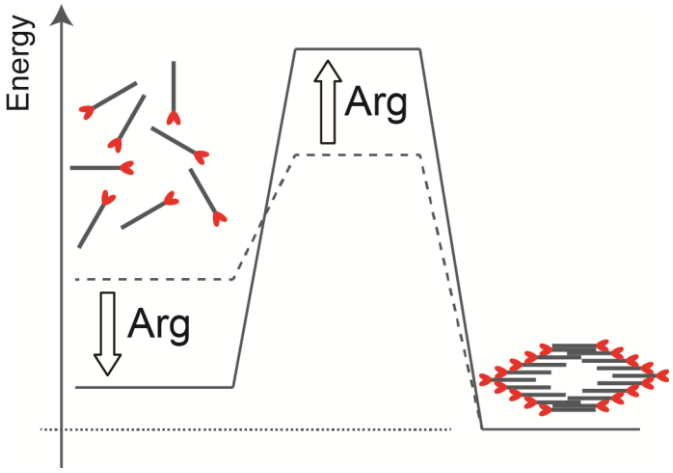


**Figure. 4.2.6.** Schematic representation of the energy sates of solubilized and aggregates of myosin.

of the myosin monomer by Arg occurred without altering the structure of myosin. It would be of great interest to test the utility of arginine in processing meat products containing myosin based on its ability to increase the solubility of monomeric myosin.

# References


[1] Friedman M Food browning and its prevention: an overview 1996 *J. Agric. Food Chem*. **44** 631–653

[2] Craig R, Woodhead JL 2006 Structure and function of myosin filaments *Curr. Opin. Struct. Biol.* **16** 204–212.

[3] Xu JQ, Harder BA, Uman P, Craig R 1996 Myosin filament structure in vertebrate smooth muscle *J. Cell Biol.* **134** 53-66

[4] Sohn RL, Vikstrom KL, Strauss M, Carolyn C, Szent-Gyorgyi AG, Leinwand LA 1997 A 29 residue region of the sarcomeric myosin rod is necessary for filament formation *J. Mol. Biol.* **266** 317-330.

[5] Niederman R, Pollard TD 1975 Human platelet myosin. II. In vitro assembly and structure of myosin filaments. *J. Cell Biol.* **67** 72-92.

[6] Sinard JH, Stafford WF, Pollard TD 1989 The mechanism of assembly of Acanthamoeba myosin-II minifilaments: minifilaments assemble by three successive dimerization steps *J. Cell Biol.* **109** 1537-1547

[7] Lin TM, Park JW 2008 Solubility of Salmon Myosin as Affected by Conformational Changes at Various Ionic Strengths and pH *J. Food Sci.* **63** 215-218.

[8] Tsunashima Y, Akutagawa T 2004 Structure transition in myosin association with the change of concentration: Solubility equilibrium under specified KCl and pH condition *Biopolymers* **75** 264-277.

[9] Ishioroshi M, Samejima K, Yasui T 1979 Heat‐induced gelation of myosin: factors of pH and salt concentrations *J. Food Sci.* **44** 1280-1284.

[10] Ito Y, Tatsumi R, Wakamatsu J, Nishimura T, Hattori A 2003 The solubilization of myofibrillar proteins of vertebrate skeletal muscle in water *Anim. Sci. J.* **74** 417-425.

[11] Hayakawa T, Ito T, Wakamatsu J, Nishimura T, Hattori A 2009 Myosin is solubilized in a neutral and low ionic strength solution containing l-histidine *Meat Sci.* **82** 151-154

[12] Hayakawa T, Ito T, Wakamatsu J, Nishimura T, Hattori A 2010 Myosin filament depolymerizes in a low ionic strength solution containing l-histidine *Meat Sci.* **84** 742-746

[13] Reddy KRC., Lilie H,Rudolph R, Lange C 2005 l-Arginine increases the solubility of unfolded species of hen egg white lysozyme *Protein Sci.* **14** 929-935

[14] Arakawa T, Tsumoto K 2003 The effects of arginine on refolding of aggregated proteins: not facilitate refolding, but suppress aggregation *Biochem. Biophys. Res. Commun.* **304** 148-152.

[15] Shiraki K, Kudou M, Fujiwara S, Imanaka T, Takagi M Biophysical effect of amino acids on the prevention of protein aggregation *J. Biochem.* **132** 591-595

[16] Lyutova EM, Kasakov AS, Gurvits BY 2007 Effects of arginine on kinetics of protein aggregation studied by dynamic laser light scattering and tubidimetry techniques *Biotechnol. Prog.* **23** 1411-1416

[17] Hamada H, Takahashi R, Noguchi T, Shiraki K Differences in the effects of solution additives on heat- and refolding-induced aggregation *Biotechnol. Prog.* **24** 436-443

[18] Matsuoka T, Hamada H, Matsumoto K, Shiraki K Indispensable structure of solution additives to prevent inactivation of lysozyme for heating and refolding *Biotechnol. Prog.* **25** 1515-1524

[19] Buchner J, Rudolph R 1991 Renaturation, purification and characterization of recombinant Fab-fragments produced in Escherichia coli *Nat. Biotechnol.* **9** 157-162

[20] De Bernardez Clark E, Schwarz E, Rudolph R 1999 Inhibition of aggregation side reactions during in vitro protein folding *Methods Enzymol.* **309** 217-236

[21] Lange C, Rudolph R 2009 Suppression of protein aggregation by L-Arginine *Curr. Pharm. Biotechnol.* **10** 408-414

[22] Tsumoto K, Umetsu M, Kumagai I, Ejima D, Philo JS, Arakawa T 2004 Role of arginine in protein refolding, solubilization, and purification *Biotechnol. Prog.* **20** 1301-1308

[23] Ito L, Shiraki K, Yamaguchi H 2010 Comparative analysis of amino acids and amino-acid derivatives in protein crystallization *Acta Crystallogr., Sect. F: Struct. Biol. Cryst. Commun.* **66** 744-749

[24] Ejima D, Yumioka R, Tsumoto K, Arakawa T 2005 Effective elution of antibodies by arginine and arginine derivatives in affinity column chromatography *Anal. Biochem.* **345** 250-257

[25] Ejima D, Yumioka Y, Arakawa T, Tsumoto K 2005 Arginine as an effective additive in gel permeation chromatography *J. Chromatogr., A* **1094** 49-55

[26] Arakawa T, Kita Y, Sato H, Ejima D 2009 MEP chromatography of antibody and Fc-fusion protein using aqueous arginine solution *Protein Expression Purif.* **63** 158-163

[27] Arakawa T, Tsumoto K, Nagase K, Ejima D 2007 The effects of arginine on protein binding and elution in hydrophobic interaction and ion-exchange chromatography *Protein Expression Purif.* **54** 110-116

[28] Mason PE, Dempsey CE, Neilson GW, Kline SR, Brady JW 2009 Preferential Interactions of Guanidinum Ions with Aromatic Groups over Aliphatic Groups *J. Am. Chem. Soc.* **131** 16689-16696

[29] Ito L, Shiraki K, Matsuura T, Okumura M, Hasegawa K, Baba S, Yamaguchi H, Kumasaka T High-resolution X-ray analysis reveals binding of arginine to aromatic residues of lysozyme surface: implication of suppression of protein aggregation by arginine *Protein Eng., Des. Sel.* **24** 269-274

[30] Hirano A, Kameda T, Arakawa T, Shiraki K Arginine-assisted solubilization system for drug substances: Solubility experiment and simulation *J. Phys. Chem. B* **114** 13455-13438

[31] Shukla D, Trout BL 2010 Interaction of arginine with proteins and the mechanism by which it inhibits aggregation *J. Phys. Chem. B* **114** 13426- 13438

[32] Arakawa T, Ejima D, Tsumoto K, Obeyama N, Tanaka Y, Kita Y, Timasheff SN 2007 Suppression of protein interactions by arginine: A proposed mechanism of the arginine effects *Biophys. Chem.* **127** 1-8.

[33] Hirano A, Arakawa T, Shiraki K 2008 Arginine increases the solubility of coumarin: Comparison with salting-in and salting-out additives *J. Biochem.* **144** 363-369

[34] Baynes BM, Wang DIC, Trout BL 2005 Role of arginine in the stabilization of proteins against aggregation *Biochemistry* **44** 4919-4925

[35] Schneider CP, Trout BL 2009 Investigation of cosolute-protein preferential interaction coefficients: New insight into the mechanism by which arginine inhibits aggregation *J. Phys. Chem. B* **113** 2050-2058

[36] Mclachlan AD, Karn J 1982 Periodic charge distributions in the myosin rod amino acid sequence match

cross-bridge spacings in muscle *Nature* **299** 226-231

# Chapter 5

# Degeneration of Amyloid Fibrils

## 5.1 Degeneration of Amyloid-ß Fibrils Caused by Exposure to Low-Temperature Atmospheric-Pressure Plasma in Aqueous Solution

# Introduction

Low-temperature atmospheric-pressure plasma (LTAPP) generates reactive oxygen species (ROS)[1], typically hydroxyl radicals (OH•) [2-6], superoxide anion radicals ($O_2^-$•) [7], hydroperoxyl radicals (HOO•) [8], singlet oxygen ($^1O^2$), and atomic oxygen (O) [9] in the gas phase. It has been reported that the plasma processing of solids is useful in producing surface coatings for biomedical materials [10-12]. In contrast, once LTAPP is exposed to a solution, advanced reaction fields are induced inside the liquid because some of the plasma-induced ROS diffuse into the solution. This feature of LTAPP processing allows the exploitation of a type of chemical reactions in solution [13-15]. Because organisms also present aqueous conditions, this phenomenon is expected to inform the development of plasma medicines [16, 17] for cancer [18-21], glioma [22], dentistry [23], blood coagulation [24], disruption of the human hepatocyte cytoskeleton [25], sterilization [26-35], and Parkinson's disease[36]. In this letter, we examine the application possibilities of LTAPP for the treatment of Alzheimer's disease (AD), which is a progressive neurodegenerative disorder characterized by memory loss and dementia that was reported by Alois Alzheimer in 1906; it is the most common cause of dementia in elderly people, accounting for more than 15 million cases worldwide.

AD is characterized pathologically by proteinaceous deposits in various areas of the brain, particularly in the hippocampus and cerebral cortex [37]. Such deposits and neurofibrillary tangles in the brain, accompanied by neuronal and synaptic loss, are pathological hallmarks of AD. The plaques mainly consist of fibrils of amyloid-ß (Aß) peptides [38]. Aβ fibrils are linear β-sheet-rich aggregates of protein that form spontaneously in solution. Aβ fibrils have cytotoxicity and high structural stability that is not easily degraded by protease; thus, they are considered to be protease resistant, and this resistance means that they constitute a major component of neuritic plaque in the

brain of an AD patient. Therefore, techniques for destabilizing or breaking down Aß fibrils will be valuable in AD therapy. In this study, using an in vitro system, we demonstrated that LTAPP processing changed the protease resistance, ß-sheet structure, and surface properties of Aß fibrils in solution, although the morphology, length, and cytotoxicity of a plasma-exposed fibril remained unchanged.

# Materials and methods

## Materials

Lyophilized human amyloid-β 1–40 (Aβ) was acquired from Peptide Institute Inc. (Osaka, Japan). Sodium chloride (NaCl) and sodium phosphate were obtained from Nacalai Tesque Inc. (Kyoto, Japan). Thioflavin-T (ThT) was obtained from Wako Pure Chemical Industries, Ltd. (Osaka, Japan). 8-Anilino-1-naphthalenesulfonic acid (ANS) was acquired from Sigma Chemical Co. (St. Louis, MO, USA). An HMW native marker kit (GE Healthcare) comprising thyroglobulin (669 kDa), ferritin (440 kDa), catalase (232 kDa), lactate dehydrogenase (140 kDa), and albumin (66 kDa) was used as a molecular-weight marker.

## Plasma-jet generation

A low-frequency (LF) plasma jet was used in a similar manner as described previously[1-3]. The plasma shape was elongated from the end of a quartz glass tube, in which helium gas flowed, by the application of an alternating-current high voltage (ranging from -3.5 to +5.0 kV at a frequency of

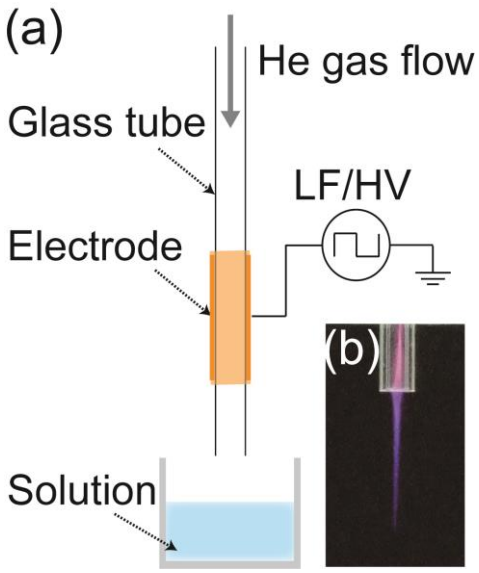


**Figure. 5.1.1.** Plasma jet generated using helium gas flowing through quartz glass tube. **(a)** Schematic representation of the plasma-jet system with sample solution. The plume-like structure of the plasma extends toward the surface of the sample solution. **(b)** Photograph of the plasma jet.

13.9 kHz) to a single-sided electrode. The electrode consisted of a small copper sheet wound around the glass tube (Fig. 5.1.1a). This LF plasma jet was generated inside an airtight chamber from its center port. The ambient gas of the chamber could be controlled using the other oxygen ($O_2$) gas supply port connected to the side of the plasma-jet port. The flow rates of He and $O_2$ gas were 0.50 and 0.15 l/min, respectively. Helium plasma with a low gas temperature was generated in an elongated shape (Fig. 5.1.1b). Various active oxygen species produced from the $O_2$ gas by the He plasma were supplied to the solution in the chamber. A sample of 0.3 ml containing 5 μM Aβ fibrils and 100 mM NaCl in 50 mM Na-phosphate buffer (pH 7.4) was applied to the solution in the vessel. To exchange the ambient gas, He and $O_2$ gas were pre-flowed in the chamber for 5 min.

## Preparation of amyloid- ß fibrils

Amyloid-β fibrils were formed as follows. A stock solution of Aβ was prepared by dissolving 1 mM of Aβ in 0.1% ammonia solution. The fibrillization solutions contained 25 μM Aβ, 100 mM NaCl, and 50 mM Na-phosphate buffer (pH 7.4). After incubation for 5 days at 37°C, the solution was diluted with PBS (100 mM NaCl and 50 mM Na-phosphate buffer at pH 7.4) and used as a sample.

## Proteolysis of amyloid fibrils

Aβ fibrils with/without plasma exposure were subjected to proteolysis using protease from Sigma Chemical Co. (St. Louis, MO) at a protease/Aβ ratio of 2:1(w/w). The aliquots were incubated for 24 h at 25°C. The samples were analyzed via light scattering and AFM.

## TEM and AFM imaging of amyloid fibrils

Transmission electron microscopy (TEM) images of the amyloid fibrils were obtained using stain (silicon tungstate) and a transmission microscope (JEM-1400; JEOL, Tokyo, Japan) with an acceleration voltage of 200 keV. The sample solution was diluted 100-fold with pure water. A volume of 2 μl of the solution was negatively stained with 2 μl of a 2% (w/v) silicon tungstate solution. A volume of 2 μl of the stained solution was placed on a 150-mesh copper grid covered with a carbon-coated hydrophilic film and dried for a few minutes.

Atomic force microscopy (AFM) images of the amyloid fibrils were obtained using an S-image system (SII NanoTechnology Inc., Chiba, Japan) operating in taping mode and a silicon cantilever (SI-DF20, SII Nanotechnology). The sample solution was diluted 10-fold with pure water. Subsequently, 3 μL of the diluted sample was placed on freshly cleaved mica coated with poly-lysine (Mw 1,000-5,000) and dried in air.

## Circular dichroism

Circular dichroism (CD) spectroscopy was performed in a 1 mm path-length quartz cuvette using a spectropolarimeter (J-720 W; Japan Spectroscopic Co., Ltd., Tokyo, Japan). The CD spectra were recorded for 195–260 nm at 25°C. The far-UV CD spectra of the samples were corrected by subtracting the corresponding spectra of the buffers in the absence of Aβ fibrils.

## ThT and ANS fluorescence and light-scattering assay

An Aβ fibril solution of 30 μl was mixed with 1,470 μl of 5 μM ThT in 50 mM Gly buffer (pH 8.5). The ThT fluorescence was monitored using a spectrofluorometer (FP-6500; Japan Spectroscopic Co., Ltd.) with a 1 cm path-length quartz cell. The sample was excited at 440 nm (5 nm slit width), and the fluorescence intensity at 480 nm (5 nm slit width) was monitored at 25°C; the temperature was controlled using a temperature controller (Jasco Corp.).

For the ANS fluorescence measurements, Aβ samples (10 μM) were prepared in a PBS buffer containing 50 μM ANS. The samples were excited at 370 nm (bandwidth of 10 nm), and the emission spectra were recorded at 470–580 nm.

Light scattering was measured using a spectrophotometer (V-630; Japan Spectroscopic Co., Ltd). The samples were assayed in triplicate, and the average of the three spectra was presented.

## Toxicity assay

Cell viability was determined with the use of a cell proliferation kit (Roche, Basel, Switzerland), which was based on the conversion of tetrazolium salt by mitochondrial dehydrogenase to a formazan product that is spectrophotometrically measurable at 550 nm, according to the manufacturer's instructions.

PC12 cells (a clonal line of rat pheochromocytoma) were maintained in RPMI1640 medium with 10% horse serum, 5% fetal bovine serum, penicillin (100 U/mL), and streptomycin (100 μg/mL) in 5% $CO_2$ at 37°C.

The viability of the PC12 cells was measured using Cell Proliferation Kit I (MTT) from Roche (Indianapolis, IN). The PC12 cells (40,000 cells/well in 80 μL of medium) were cultured in PDL-coated 96-well plates overnight. Aβ samples (20 μL), aliquoted from the plasma-exposed Aβ samples with the addition of catalase after plasma exposure and diluted with PBS to the desired Aβ concentrations, were added to the wells and incubated for 16 h for PC12 cells or 24 h for primary cortical neurons. For the control samples, the same volume of PBS was added to the wells. For the 3-(4,5-dimethylthiazol-2-yl)-2,5-diphenyltetrazolium bromide (MTT) reaction and measurements, the adsorption values at 550 nm were determined using a Tecan (Männedorf, Switzerland) microplate reader. The viability for cells exposed to PBS was used as the 100% viability control.

# Results and discussion

For the present study, a low-frequency (LF) plasma jet was used for the LTAPP processing in a manner similar to that described in our previous study[8, 34, 39]. The plasma shape was elongated from the end of a quartz glass tube, in which helium gas flowed, by the application of an alternating-current high voltage (ranging from -3.5 to +5.0 kV at a frequency of 13.9 kHz) to a single-sided electrode (Fig. 5.1.1a). Helium plasma with a low gas temperature was generated in an elongated shape (Fig. 5.1.1b). The discharge power of the plasma was 3 W. The LF plasma jet was generated inside an airtight chamber from its center port. The ambient gas of the chamber could be controlled using the other oxygen ($O_2$) gas supply port connected to the side of the plasma-jet port. The flow rates of He and $O_2$ gas were 0.50 and 0.15 l/min, respectively. Various active oxygen species produced from the $O_2$ gas by the plasma were supplied to the solution.

Amyloid fibrils of human protein Aß were prepared in vitro. Briefly, lyophilized Aß1–40 from Peptide Institute Inc. (Osaka, Japan) was dissolved in phosphate-buffered saline (PBS; 100 mM NaCl, 50 mM Na-phosphate buffer at pH 7.4), and then the sample was incubated at 37°C for 5 days. As expected, typical mature Aß fibrils were formed, which are characterized by (i) a sigmoidal evolution of the Thioflavine T (ThT) fluorescent intensity with a lag time of 1-2 days (Fig. 5.1.2a), (ii) linear protein aggregates visualized via transmission electron microscopy (TEM) with stain (Fig. 5.1.2a inset), and (iii) a ß-sheet structure identified by a negative peak at 218 nm in the far-UV circular dichroism (CD) spectra (Fig. 5.1.2b). The Aß fibril solution was treated with an LF plasma jet (Fig. 5.1.1). Then, the plasma-exposed Aß fibrils were analyzed using several biochemical and biophysical methods to detect changes in physiological activity. These experimental procedures and systems are described in detail in the supplemental information[48].

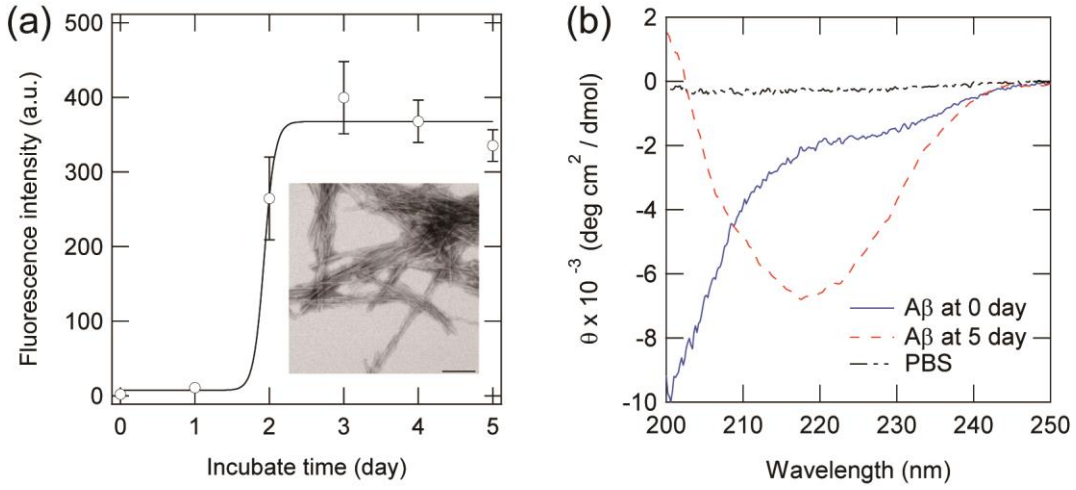


**Figure 5.1.2.** Preparation of Aβ fibrils. (a) Growth of Aβ fibrils detected via ThT fluorescence. The continuous line though the data points is the result of fitting with a sigmoidal curve. (Inset) TEM image of Aβ fibrils after incubation for 5 days. (b) Circular dichroism spectra of Aβ fibrils after incubation for 0 days (continuous line) and 5 days (broken line). The line corresponding to PBS represents the buffer without Aβ.

The morphology, length, aggregation extent, and molecular weight of the plasma-exposed fibrils were investigated. Figures 5.1.3a and 3b show TEM images of fibrils that were exposed to the plasma for 0 and 30 min, respectively. The Aß fibrils that were exposed for 30 min were observed to be non-branched fibrils of more than 1 μm in length, similar to the untreated fibrils (0 min). The length distributions of the plasma-exposed fibrils for 0 and 30 min were almost identical, indicating that the Aß fibrils were not fragmented by plasma exposure in solution (Fig. 5.1.3c and 5.1.3d). This result was supported by a native PAGE/Western-blotting analysis, which showed that there were no soluble oligomeric species in the plasma-exposed fibril samples (Fig. 5.1.3e). The aggregation extent of the Aß fibrils was monitored via light scattering at 350 nm, which is sensitive to the number and size of aggregates present in a solution, as reported previously[40, 41]. The light-scattering intensity was proportional to the concentration of Aß, but it was unchanged by the plasma exposure (Fig. 5.1.3f). These results demonstrated that the morphology, length, molecular weight, and aggregation extent of the Aß fibrils were unchanged by plasma exposure for a duration of several minutes. In contrast, it has been reported that amyloid fibrils of α-synuclein were

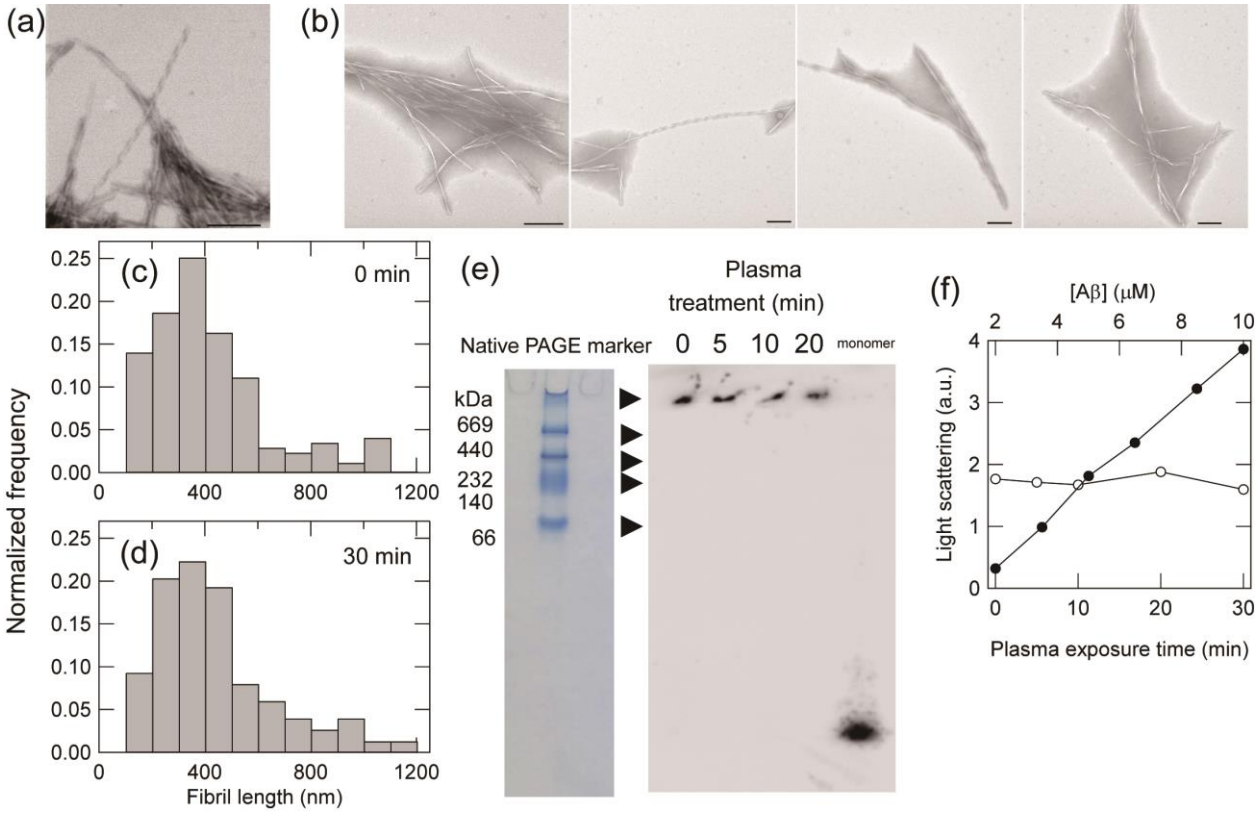


**Figure. 5.1.3.** Characterization of Aβ fibrils exposed to an LF plasma jet. **(a, b)** Morphology of Aβ fibrils (a) before and (b) after the plasma exposure (30 min) as imaged via TEM. The scale bars represent 200 nm. **(c, d)** Contour-length distribution of Aβ fibrils (c) before and (d) after the plasma exposure, calculated from TEM images. The sampling numbers were 150 in (c) and 171 in (d). **(e)** Native PAGE/Western-blotting analysis of Aβ fibrils exposed to an LF plasma jet using mouse monoclonal anti-Aβ (6E10). Unincubated Aβ monomers were used as a control. **(f)** Light scattering at 350 nm as a function of the Aβ concentration (closed circles, top axis) and the plasma-exposure time (open circles, bottom axis).

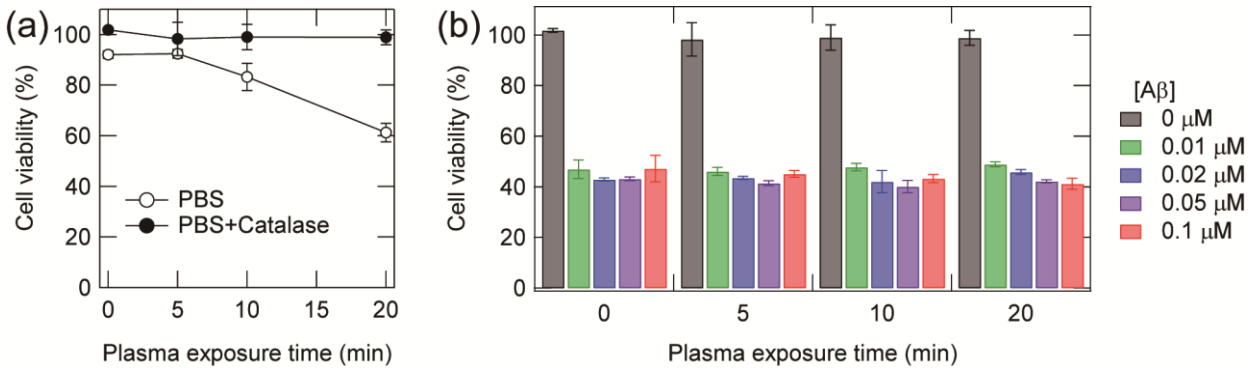


**Figure. 5.1.4.** Cytotoxicity assays of the plasma-treated samples with PC12 cells using an MTT assay. **(a)** Cytotoxicity assays of plasma-treated PBS without Aβ in the absence (open circles) or presence (closed circles) of 2 μg/ml of catalase. The catalase was added after plasma exposure and before the cytotoxicity assays. **(b)** Cytotoxicity assays of Aβ as a function of the exposure time with the addition of 2 μg/ml of catalase after plasma exposure.

fragmented by 6 min of exposure to a low-temperature plasma jet in solution [36]. These differing results may be attributable to the difference in the structural stability of the amyloid fibrils [42].

The cytotoxicity of the plasma-exposed Aß fibrils on a rat pheochromocytoma PC12 cell was examined using an MTT assay, as previously described [43]. First, we demonstrated that the plasma-exposed PBS without Aß also exhibited cytotoxicity (Fig. 5.1.4a) because of the hydrogen peroxide generated by a plasma-inactivated culture cell [18]. To overcome this problem, catalase, which is an enzyme that catalyzes the decomposition of hydrogen peroxide to water and oxygen, was added to the sample solution to avoid the confounding influence of hydrogen peroxide in the cytotoxicity assay (Fig. 5.1.4a). Figure 5.1.4b shows the cytotoxicity of plasma-exposed Aß fibrils with the inclusion of catalase, which was added after plasma exposure. The Aß fibrils without plasma exposure exhibited high cytotoxicity. The Aß fibrils that were exposed to plasma for 5-20 min also exhibited high cytotoxicity. Thus, it could be concluded that the cytotoxicity of the Aß fibrils was not changed by plasma exposure for a duration of several minutes.

The protease-resistant property of the plasma-exposed fibrils was examined using trypsin, which is a serine protease that cleaves peptide chains at the carboxyl end of the amino acids lysine and arginine [44]. Figure 5.1.5a shows the light-scattering intensity of the plasma-exposed fibrils after the trypsin treatment. The light-scattering intensity of the Aß fibrils decreased with increasing plasma-exposure time, indicating that the protease resistance of the Aß fibrils was decreased by the plasma treatment. The degradation of the plasma-exposed fibrils by trypsin was confirmed via atomic force microscopy (AFM) (Fig. 5.1.5b and 5.1.5c). The degraded Aß fibrils were primarily observed as spherical aggregates (Fig. 5.1.5b), which may consist of insoluble peptides of Aß formed via proteolysis. In contrast, the Aß fibrils that were not exposed to the plasma remained as fibrillar aggregates even after the trypsin treatment (Fig. 5.1.5c). No aggregates of the Aß peptides before incubation were observed (Fig. 5.1.5d). These results demonstrated that the protease

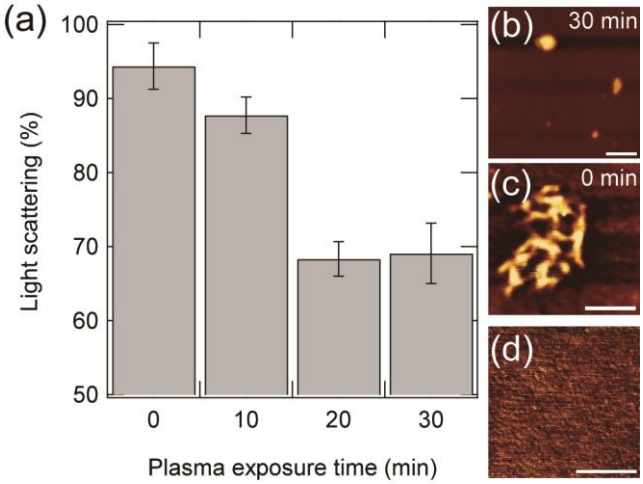


**Figure. 5.1.5.** Evaluation of the protease resistance of Aβ fibrils exposed to an LF plasma jet. **(a)** Light-scattering intensity at 350 nm of Aβ fibrils incubated with trypsin for 24 h as a function of the plasma-exposure time. The light-scattering intensity of 100% was defined by the measurement of a sample of unexposed Aβ fibrils without trypsin digestion. **(b, c)** AFM images of the Aβ fibrils that were exposed to the plasma for (b) 30 min and (c) 0 min and incubated with trypsin for 24 h. **(d)** AFM image of the Aβ before incubation. The scale bars represent 200 nm.

resistance of the Aß fibrils was degraded by plasma exposure.

To elucidate the mechanism of the loss of the protease resistance of the Aß fibrils caused by plasma exposure, we examined the structural properties of the plasma-exposed Aß fibrils via far-UV CD spectroscopy to determine the ß-sheet content and via fluorescence assay with thioflavin T (ThT) to determine the amount of accumulated cross-ß structure and 8-anilino-1-naphthalenesulfonic acid (ANS) to understand the surface hydrophobicity (Fig. 5.1.6).

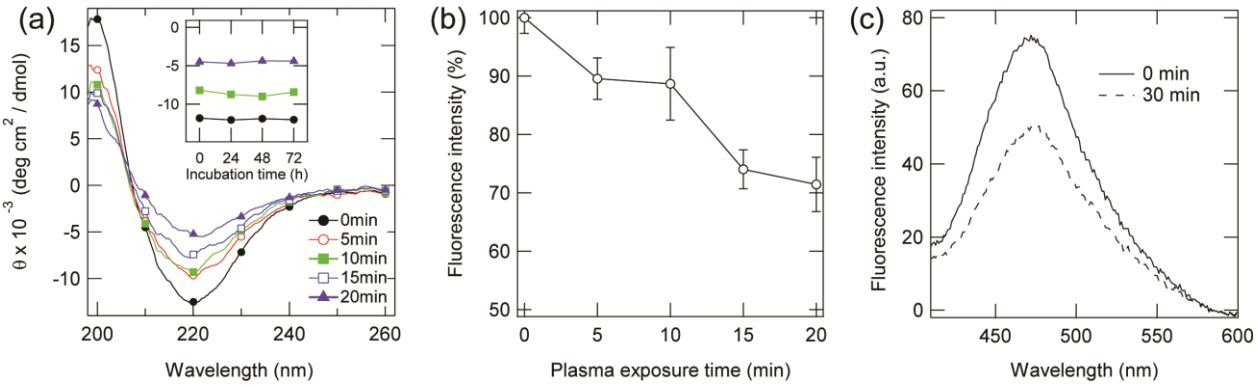


**Figure. 5.1.6. (a)** Circular dichroism spectra of Aβ fibrils exposed to an LF plasma jet for various durations. (Inset) The intensity at 218 nm of the Aβ fibrils incubated at 37°C after the plasma exposure. **(b)** ThT fluorescence intensity of Aβ fibrils as a function of the plasma-exposure time. The fluorescence emission at 480 nm was measured for excitation at 420 nm. **(c)** ANS fluorescence spectra of the Aβ fibrils before and after plasma exposure for 30 min. The samples were excited at 370 nm.

The peak at 218 nm in the CD spectrum decreased in intensity with increasing plasma-exposure time, indicating that the regular cross-ß structure of the Aß fibrils [45] was destroyed by plasma exposure. The intensity at 218 nm of the plasma exposed Aβ fibrils was unchanged even after incubation at 37°C for 24-72 hours (Fig. 5.1.6a inset), indicating that there is no recovery of Aβ fibrils from the damages unlike living cells. The ThT fluorescence intensity decreased with increasing plasma-exposure time (Fig. 5.1.6b), which is consistent with the results from the CD spectra (Fig. 5.1.6a), indicating the unfolding of the ß-sheet core in the Aß fibrils as a result of the plasma exposure. The ANS fluorescence of the plasma-exposed Aß fibrils was quenched (Fig. 5.1.6c), which indicates that the surface hydrophobicity of the Aß fibrils was decreased by the plasma exposure. These results suggest that the degeneration of Aß fibrils induced by plasma exposure might cause the loss of their protease-resistant property.

Plasma exposure in solution induces chemical reaction fields not only on the surface of the liquid but also inside the liquid itself because of the diffusion of ROS generated in the gas phase. These species should react with Aß fibrils. In fact, some amino-acid residues of Aß peptides, such as methionine, tyrosine, and histidine, are oxidized by the ROS generated via laser irradiation in solution [46]. We have previously reported that chemical modifications of amino-acid residues induced the denaturation and inactivation of proteins via plasma exposure in solution [39]. Therefore, it is plausible that chemical reactions of the amino-acid residues with the ROS generated by plasma may result in the degeneration of Aß fibrils and the loss of their protein-resistant property.

It was demonstrated that the protease resistance, ß-sheet structure, and surface properties of Aß fibrils were changed by LTAPP processing in aqueous solution, while the morphology, length, and cytotoxicity remained unchanged. In a previous study, the degradation of Aß fibrils induced by direct LTAPP treatment on a solid surface has been reported [47]. Any species can act in direct LTAPP treatment; on the other hand, only soluble and long-lived species, such as HOO•, can attack in LTAPP processing in aqueous solution [34]. Therefore, the seemingly contradictory results of the two studies might be attributable to the difference in the amount and type of ROS attacking the Aß fibrils.

# Conclusion

In conclusion, we demonstrated that LTAPP treatment caused the degeneration of Aß fibrils, which are a major component of the neuritic plaque associated with AD, in terms of accumulated ß-sheet content and protease resistance, while the morphology, contour length, and cytotoxicity of the Aß fibrils remained unchanged. The loss of the protease resistance of the Aß fibrils caused by plasma exposure suggests prospects for utilizing LTAPP for the elimination of neuritic plaque associated with AD by accelerating the proteolysis of Aß fibrils.

# References


[1] Bruggeman P, Iza F, Lauwers D and Gonzalvo Y A 2010 Mass spectrometry study of positive and negative ions in a capacitively coupled atmospheric pressure RF excited glow discharge in He-water mixtures *Journal of Physics D-Applied Physics* **43** 012003

[2] Locke B R, Sato M, Sunka P, Hoffmann M R and Chang J S 2006 Electrohydraulic discharge and nonthermal plasma for water treatment *Ind. Eng. Chem. Res.* **45** 882-905

[3] Sahni M and Locke B R 2006 The effects of reaction conditions on liquid-phase hydroxyl radical production in gas-liquid pulsed-electrical-discharge reactors *Plasma Processes and Polymers* **3** 668-81

[4] Sahni M and Locke B R 2006 Quantification of hydroxyl radicals produced in aqueous phase pulsed electrical discharge reactors *Ind. Eng. Chem. Res.* **45** 5819-25

[5] Bruggeman P and Leys C 2009 Non-thermal plasmas in and in contact with liquids *Journal of Physics D-Applied Physics* **42** 053001

[6] Burlica R, Shih K Y and Locke B R 2010 Formation of H-2 and H2O2 in a Water-Spray Gliding Arc Nonthermal Plasma Reactor *Ind. Eng. Chem. Res.* **49** 6342-9

[7] Tani A, Ono Y, Fukui S, Ikawa S and Kitano K 2012 Free radicals induced in aqueous solution by non-contact atmospheric-pressure cold plasma *Appl. Phys. Lett.* **100** 254103

[8] Ikawa S, Kitano K and Hamaguchi S 2010 Effects of pH on Bacterial Inactivation in Aqueous Solutions due to Low-Temperature Atmospheric Pressure Plasma Application *Plasma Processes and Polymers* **7** 33-42

[9] Liu D X, Rong M Z, Wang X H, Iza F, Kong M G and Bruggeman P 2010 Main Species and Physicochemical Processes in Cold Atmospheric-pressure He + O-2 Plasmas *Plasma Processes and Polymers* **7** 846-65

[10] Favia P 2012 Plasma deposited coatings for biomedical materials and devices: Fluorocarbon and PEO-like coatings *Surface & Coatings Technology* **211** 50-6

[11] Di Mundo R, Gristina R, Sardella E, Intranuovo F, Nardulli M, Milella A, Palumbo F, d'Agostino R and Favia P 2010 Micro-/Nanoscale Structuring of Cell-Culture Substrates with Fluorocarbon Plasmas *Plasma Processes and Polymers* **7** 212-23

[12] Detomaso L, Gristina R, Senesi G S, d'Agostino R and Favia P 2005 Stable plasma-deposited acrylic acid surfaces for cell culture applications *Biomaterials* **26** 3831-41

[13] Furusho H, Miyamoto D, Nagasaki Y, Kitano K and Hamaguchi S 2007 Synthesis of uniformly dispersed metal nanoparticles with dispersion stability by nonequilibrium atmospheric plasma jets *J. Photopolym. Sci. Technol.* **20** 229-33

[14] Furusho H, Kitano K, Hamaguchi S and Nagasaki Y 2009 Preparation of Stable Water-Dispersible PEGylated Gold Nanoparticles Assisted by Nonequilibrium Atmospheric-Pressure Plasma Jets *Chem. Mater.* **21** 3526-35

[15] Sumitani S, Murotani H, Oishi M, Kitano K, Hamaguchi S and Nagasaki Y 2009 Nonequilibrium Atmospheric Plasma Jets Assisted Stabilization of Drug Delivery Carriers: Preparation and Characterization of Biodegradable Polymeric Nano-Micelles with Enhanced Stability *J. Photopolym. Sci. Technol.* **22** 467-71

[16] Kong M G, Kroesen G, Morfill G, Nosenko T, Shimizu T, van Dijk J and Zimmermann J L 2009 Plasma medicine: an introductory review *New Journal of Physics* **11** 115012

[17] Babaeva N Y and Kushner M J 2013 Reactive fluxes delivered by dielectric barrier discharge filaments to slightly wounded skin *J. Phys. D: Appl. Phys.* **46** 025401

[18] Sato T, Yokoyama M and Johkura K 2011 A key inactivation factor of HeLa cell viability by a plasma flow *J. Phys. D: Appl. Phys.* **44** 372001

[19] Kim K, Choi J D, Hong Y C, Kim G, Noh E J, Lee J-S and Yang S S 2011 Atmospheric-pressure plasma-jet from micronozzle array and its biological effects on living cells for cancer therapy *Appl. Phys. Lett.* **98** 073701

[20] Kim S J, Chung T H, Bae S H and Leem S H 2010 Induction of apoptosis in human breast cancer cells by a pulsed atmospheric pressure plasma jet *Appl. Phys. Lett.* **97** 023702

[21] Kim C H, Kwon S, Bahn J H, Lee K, Jun S I, Rack P D and Baek S J 2010 Effects of atmospheric nonthermal plasma on invasion of colorectal cancer cells *Appl. Phys. Lett.* **96** 243701

[22] Vandamme M, Robert E, Pesnel S, Barbosa E, Dozias S, Sobilo J, Lerondel S, Le Pape A and Pouvesle J M 2010 Antitumor Effect of Plasma Treatment on U87 Glioma Xenografts: Preliminary Results *Plasma Processes and Polymers* **7** 264-73

[23] Yamazaki H, Ohshima T, Tsubota Y, Yamaguchi H, Jayawardena J A and Nishimura Y 2011 Microbicidal activities of low frequency atmospheric pressure plasma jets on oral pathogens *Dent. Mater. J.* **30** 384-91

[24] Fridman G, Peddinghaus M, Balasubramanian M, Ayan H, Fridman A, Gutsol A and Brooks A 2006 Blood Coagulation and Living Tissue Sterilization by Floating-Electrode Dielectric Barrier Discharge in Air *Plasma Chem. Plasma Process.* **26** 425-42

[25] Gweon B, Kim D, Kim D B, Jung H, Choe W and Shin J H 2010 Plasma effects on subcellular structures *Appl. Phys. Lett.* **96** 101501

[26] Perni S, Shama G, Hobman J L, Lund P A, Kershaw C J, Hidalgo-Arroyo G A, Penn C W, Deng X T, Walsh J L and Kong M G 2007 Probing bactericidal mechanisms induced by cold atmospheric plasmas with Escherichia coli mutants *Appl. Phys. Lett.* **90** 073902

[27] Feng H Q, Wang R X, Sun P, Wu H Y, Liu Q, Fang J, Zhu W D, Li F T and Zhang J 2010 A study of eukaryotic response mechanisms to atmospheric pressure cold plasma by using Saccharomyces cerevisiae single gene mutants *Appl. Phys. Lett.* **97** 131501

[28] Bussiahn R, Brandenburg R, Gerling T, Kindel E, Lange H, Lembke N, Weltmann K D, von Woedtke T and Kocher T 2010 The hairline plasma: An intermittent negative dc-corona discharge at atmospheric pressure for plasma medical applications *Appl. Phys. Lett.* **96** 143701

[29] Kolb J F, Mohamed A A H, Price R O, Swanson R J, Bowman A, Chiavarini R L, Stacey M and Schoenbach K H 2008 Cold atmospheric pressure air plasma jet for medical applications *Appl. Phys. Lett.* **92** 241501

[30] Zhang X, Huang J, Liu X, Peng L, Guo L, Lv G, Chen W, Feng K and Yang S-z 2009 Treatment of Streptococcus mutans bacteria by a plasma needle *J. Appl. Phys.* **105** 063302

[31] Lu X, Ye T, Cao Y, Sun Z, Xiong Q, Tang Z, Xiong Z, Hu J, Jiang Z and Pan Y 2008 The roles of the various plasma agents in the inactivation of bacteria *J. Appl. Phys.* **104** 053309

[32] Majumdar A, Singh R K, Palm G J and Hippler R 2009 Dielectric barrier discharge plasma treatment on E. coli: Influence of CH[sub 4]/N[sub 2], O[sub 2], N[sub 2]/O[sub 2], N[sub 2], and Ar gases *J. Appl. Phys.* **106** 084701

[33] Burlica R, Grim R G, Shih K Y, Balkwill D and Locke B R 2010 Bacteria Inactivation Using Low Power

Pulsed Gliding Arc Discharges with Water Spray *Plasma Processes and Polymers* **7** 640-9

[34] Takai E, Ikawa S, Kitano K, Kuwabara J and Shiraki K 2013 Molecular mechanism of plasma sterilization in solution with the reduced pH method: importance of permeation of HOO radicals into the cell membrane *Journal of Physics D-Applied Physics* **46** 295402

[35] Nagatsu M, Zhao Y, Motrescu I, Mizutani R, Fujioka Y and Ogino A 2012 Sterilization Method for Medical Container Using Microwave-Excited Volume-Wave Plasma *Plasma Processes and Polymers* **9** 590-6

[36] Karakas E, Munyanyi A, Greene L and Laroussi M 2010 Destruction of alpha-synuclein based amyloid fibrils by a low temperature plasma jet *Appl. Phys. Lett.* **97** 143702

[37] Jucker M and Walker L C 2013 Self-propagation of pathogenic protein aggregates in neurodegenerative diseases *Nature* **501** 45-51

[38] Kang J, Lemaire H G, Unterbeck A, Salbaum J M, Masters C L, Grzeschik K H, Multhaup G, Beyreuther K and Mullerhill B 1987 The Precursor of Alzheimers-Disease Amyloid-A4 Protein Resembles a Cell-Surface Receptor *Nature* **325** 733-6

[39] Takai E, Kitano K, Kuwabara J and Shiraki K 2012 Protein Inactivation by Low-temperature Atmospheric Pressure Plasma in Aqueous Solution *Plasma Processes and Polymers* **9** 77-82

[40] Demeule B, Gurny R and Arvinte T 2007 Detection and characterization of protein aggregates by fluorescence microscopy *Int. J. Pharm.* **329** 37-45

[41] Yoshimura Y, Lin Y X, Yagi H, Lee Y H, Kitayama H, Sakurai K, So M, Ogi H, Naiki H and Goto Y 2012 Distinguishing crystal-like amyloid fibrils and glass-like amorphous aggregates from their kinetics of formation *Proc. Natl. Acad. Sci. U. S. A.* **109** 14446-51

[42] Meersman F and Dobson C M 2006 Probing the pressure-temperature stability of amyloid fibrils provides new insights into their molecular properties *Biochimica Et Biophysica Acta-Proteins and Proteomics* **1764** 452-60

[43] Zako T, Sakono M, Hashimoto N, Hara M and Maeda M 2009 Bovine Insulin Filaments Induced by Reducing Disulfide Bonds Show a Different Morphology, Secondary Structure, and Cell Toxicity from Intact Insulin Amyloid Fibrils *Biophys. J.* **96** 3331-40

[44] Fowler J D, Brown J A, Kvaratskhelia M and Suo Z C 2009 Probing Conformational Changes of Human DNA Polymerase lambda using Mass Spectrometry-Based Protein Footprinting *J. Mol. Biol.* **390** 368-79

[45] Fandrich M, Schmidt M and Grigorieff N 2011 Recent progress in understanding Alzheimer's beta-amyloid structures *Trends Biochem. Sci.* **36** 338-45

[46] Yagi H, Ozawa D, Sakurai K, Kawakami T, Kuyama H, Nishimura O, Shimanouchi T, Kuboi R, Naiki H and Goto Y 2010 Laser-induced propagation and destruction of amyloid beta fibrils *J Biol Chem* **285** 19660-7

[47] Bayliss D L, Walsh J L, Shama G, Iza F and Kong M G 2009 Reduction and degradation of amyloid aggregates by a pulsed radio-frequency cold atmospheric plasma jet *New Journal of Physics* **11** 115024

## 5.2 Scanning Electron Microscope Imaging of Amyloid Fibrils

# Introduction

Amyloid fibrils are linear β-sheet-rich aggregates of protein that form spontaneously both in vivo and in vitro. Amyloid fibrils are of considerable interest because amyloidogenesis has often been linked to fatal degenerative disorders, such as Alzheimer's and Parkinson's diseases. However, the well-defined structure and biocompatibility of amyloid fibrils have also suggested new functional materials [4], such as amyloid fibrils attached to yellow fluorescent protein[5], insulin amyloids as a biomaterial for cell culture surfaces[6], and templates of peptide fibres for metal nanowire[7].

Various measurement methods for amyloid fibrils have been developed, including (i) spectroscopic analysis by specific dyes, such as Congo red and thioflavin T, which are selectively adsorbed on the amyloid fibrils, (ii) spectroscopic determination of the β-sheet structure in amyloid fibrils, such as circular dichroism and infrared spectra, (iii) binding and elongation analyses of fibrils by calorimetry [8-10], and (iv) light, neutron, and x-ray scattering to detect the solution structure of amyloid fibrils. These methods provide an average ensemble picture of amyloid fibrils [11]. By contrast, atomic force microscopy (AFM) and transmission electron microscopy (TEM) can probe amyloid fibrils at the molecular level [12-19]. To our knowledge, scanning electron microscopy (SEM) has rarely been used for imaging amyloid fibrils, although it possesses a relatively high resolution of several nanometres and high usability through the detection of secondary electron emissions from specimen samples.

In this study, we demonstrated the imaging of amyloid fibrils by SEM. The results were compared with those of the well-used methods of TEM and AFM. Two types of amyloid fibrils were produced from hen egg white lysozyme (HEWL) [20] with different shapes and chemical compositions. As expected, the apparent fibril width in the SEM image was broadened compared with the height in the AFM image. This broadening, however, provides a high detectability of amyloid fibrils with diameters as thin as 3.5 nm. The chemical differences in the amyloid fibril are also reflected in the broadening of the image, which can thus be utilised for chemical-sensitive measurements.

# Materials and methods

## Materials

HEWL, sodium chloride (NaCl), potassium chloride (KCl), and sodium phosphate were from Nacalai Tesque Inc. (Tokyo, Japan). Thioflavin-T (ThT), sodium hydroxide (NaOH), and hydrochloric acid (HCl) were from Wako Pure Chemical Industries, Ltd. (Osaka, Japan).

S-amyloid was formed as follows. A stock solution containing 2.0 mg/mL HEWL, 137 mM NaCl, and 1.34 mM KCl was prepared and adjusted to pH 2.0 using HCl. Then, the solution was incubated at 50°C for 4 h with continuous agitation by a stirrer.

A-amyloid was formed as follows. A stock solution containing 5.0 mg/mL HEWL was prepared and adjusted to pH 1.0 using HCl. The solution was then incubated at 90°C for 9 h with continuous agitation by a stirrer.

The protein concentration was determined photometrically at 280 nm with an appropriate blank using a UV-vis spectrophotometer (ND-1000; NanoDrop Technologies Inc., Wilmington, DE). The extinction coefficient of 2.63 ml/mg cm was used for HEWL.

## Thioflavin T (ThT) fluorescence assay

The growth of amyloid fibrils was monitored by fluorescence analysis with ThT. After fibril formation, 15 μl of the sample solution was mixed with 1,485 μl of 5 μM ThT in 50 mM Gly NaOH buffer (pH 8.5). The ThT fluorescence was monitored using a spectrofluorimeter (FP-6500; Japan Spectroscopic Co., Ltd., Tokyo, Japan) with a 1-cm path-length quartz cell. The sample was excited at 440 nm (5 nm slit-width), and the fluorescence intensity at 480 nm (5 nm slit-width) was monitored at 25°C; the temperature was controlled using a temperature controller (Japan Spectroscopic Co., Ltd.).

## Mass spectra measurement

The mass spectra were obtained using matrix-assisted laser desorption/ionisation time of flight mass spectrometry (MALDI–TOF MS) (UltrafleXtreme MALDI–TOF/TOF; Bruker Daltonics Inc., Billerica, USA). The amyloid was centrifuged from the sample solution and dissolved in pure water for the MALDI-TOF MS measurements. The matrix solution used for these measurements was a saturated α-cyano-4-hydroxycinnamic acid (CHCA) solution in water/acetonitrile 1:1 v/v, diluted by a factor of 2 in the same solvent mixture. The sample was prepared by mixing 1.0 μl of the protein solution with 1.0 μl of the matrix solution directly on the sample probe and allowing the solution to dry at room temperature. S-amyloid and A-amyloid were analysed by MALDI-TOF-MS in the positive-ion liner and reflect modes, respectively. Native HEWL was also analysed by MALDI-TOF-MS in the positive-ion reflect mode.

## Imaging of amyloid fibrils by TEM, AFM, and SEM

Transmission electron microscopy (TEM) images of the amyloid fibrils were examined using stain (silicon tungstate) and a transmission microscope (JEM-1400; JEOL, Tokyo, Japan) with an acceleration voltage of 200 keV. The sample solution was diluted 100-fold with pure water. Then, 2 μl of the solution was negatively stained with 2 μl of 2% (w/v) silicon tungstate solution. Next, 2 μL of the stained solution was placed on a 150-mesh copper grid covered with a carbon-coated hydrophilic film. The solution on the grid was dried for a

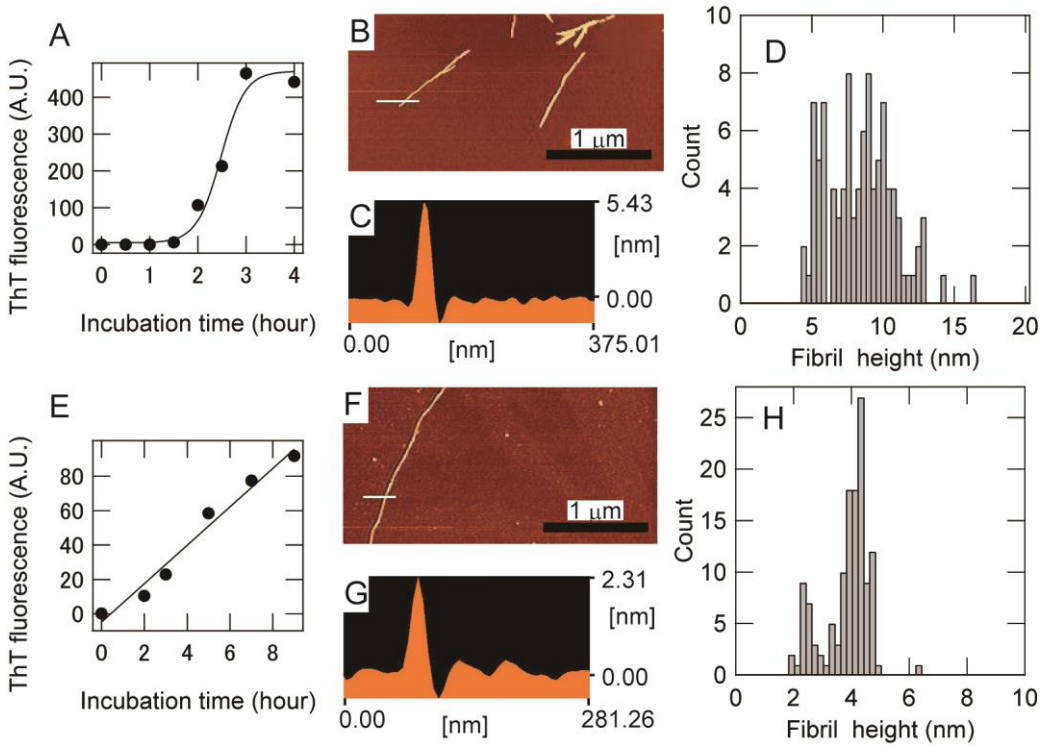


**Figure. 6.2.1.** Preparation and characterisation of S-amyloid and A-amyloid. (A) Growth of S-amyloid detected by thioflavin T (ThT) fluorescence. The continuous line though the data points was fitted with a sigmoidal curve. (B) AFM images of S-amyloid. The white line indicates the transversal profile of surface topology shown in C. (C) AFM topography image of S-amyloid, from which amyloid height was measured. (D) Histogram of S-amyloid AFM height (fibril diameter). (E-H) Figures for A-amyloid corresponding to the ones shown in Figs (A)-(D). In E, the continuous line though the data points was fitted with a linear curve.

few minutes.

Atomic force microscopy (AFM) images of amyloid fibrils were examined using S-image (SII NanoTechnology Inc., Chiba, Japan) operating in taping mode and a silicon cantilever (SI-DF20, SII Nanotechnology) with a tip curvature radius of 10 nm [25]. The sample solution was diluted 100-fold with pure water. Subsequently, 1 μL of the diluted samples was placed on freshly cleaved mica and dried in air for 10 min.

The scanning electron microscopy (SEM) images of amyloid fibrils were examined using an SEM system (Hitachi S4800) with an acceleration voltage of 15 keV. The sample solution was diluted 100-fold with pure water. Subsequently, 1 μL of the diluted samples was placed on silicone and dried in air for 10 min. The fibril width values in the TEM and SEM images were measured by comparison with each scale bar. The fibril width values in the AFM image were measured from the transversal profiles of AFM topology. The fibril height values were also determined by the transversal profiles of AFM topology.

# Results and discussion

## Preparation of amyloid fibril from self-assembled lysozyme (S-amyloid) and acid-hydrolysis lysozyme (A-amyloid)

For the present study, we prepared two types of amyloid fibrils (S-amyloid and A-amyloid) from HEWL. S-amyloid is generated from HEWL incubated under acidic conditions (pH 2) with saline under continuous agitation by a stirrer, as reported previously [21]. Under this condition, amyloid fibrils are mainly formed from nonfragmented monomers of HEWL without hydrolysis. As expected, S-amyloid was characterised by a typical sigmoidal evolution of the thioflavin T (ThT) fluorescent intensity with a lag time of 2-3 hours (Fig. 6.2.1A). S-amyloid is a non-branched straight fibril with a height of approximately 5 nm and a length of approximately 500 nm, with a helical structure (Fig. 6.2.1B, C). Figure 6.2.1D shows the histogram of the height of S-amyloid determined from an AFM image; the average diameter of the S-amyloid was 8.1 ± 2.4 nm, which is similar to the value previously reported for non-hydrolysed lysozyme fibril [13]. Notably, the histogram appears to exhibit two maxima centred at approximately 5 and 10 nm, corresponding to the inner-fibril corrugation due to the helical structure of amyloid fibrils [19].

A-amyloid was similarly generated by incubation under more acidic conditions (pH 1) at a higher

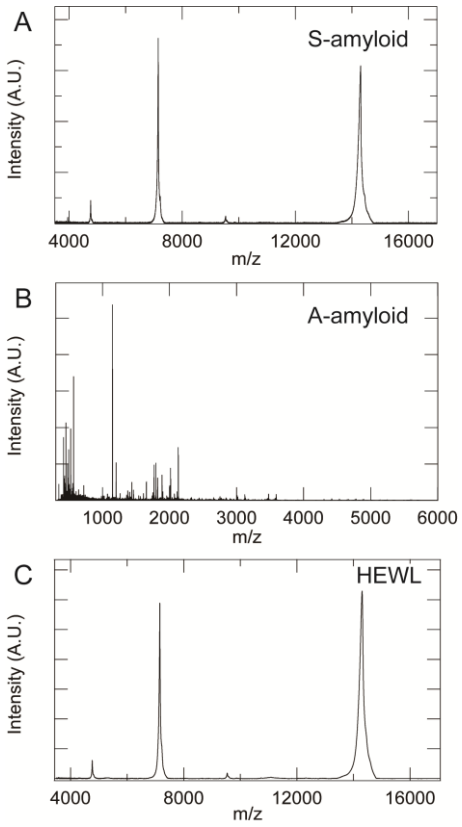


**Figure. 6.2.2.** MALDI–TOF MS spectra of S-amyloid (A), A-amyloid (B) and native HEWL as a control (C).

temperature (90°C), without saline but with continuous agitation by a stirrer. HEWL was hydrolysed under this condition [22]. The peptide fragment of hydrolysed HEWL was immediately assembled into longer fibrils, characterised by the linear increase in ThT intensity with increasing incubation, without any lag time (Fig. 1E). In the AFM measurements, long and non-branched fibrils of much greater than 1 μm were observed with a height of approximately 2 nm (Fig. 6.2.1F, G). Figure 1H shows the histogram of the height of A-amyloid, with an average diameter of 3.5 ± 0.8 nm. The histogram also shows two maxima, at 2 and 4 nm, corresponding to the helical shape of the fibril. The structure and dimensions agree with previously reported values [22].

Although they are generated from the same protein, S- and A-amyloid have different structural dimensions and chemical compositions. The MALDI–TOF MS spectra of S-amyloid showed two abundant peaks at m/z 7153, which corresponds to the doubly protonated HEWL, and at m/z 14306, which corresponds to the singly protonated HEWL (Fig. 6.2.2A). By contrast, the MALDI–TOF MS spectra of A-amyloid had many peaks below m/z 4000 (Fig. 6.2.2B). The MALDI–TOF MS spectra of native HEWL also had two abundant peaks at m/z 7153 and 14306 (Fig. 6.2.2C). These results show that S-amyloid was formed by nonfragmented monomers of HEWL without hydrolysis and A-amyloid was formed by aggregating peptide fragments of hydrolysed HEWL. Analysis using an amino acid analyser (JLC-500/V2, Japan Electron Optics Laboratory Ltd, Tokyo, Japan) revealed that A-amyloid contains fewer residues of Arg (pKa 12.5 [23]), Lys (pKa 10.2 [23]) and His (pKa 6.0 [24]) and more residues of Leu, Ile and Pro than native HEWL (data not shown), indicating that A-amyloid has less electrical capacity than S-amyloid. As described above, these two amyloid fibrils exhibited rather well-defined structures. Therefore, S-amyloid and A-amyloid are useful model fibrils for characterising the utility of SEM.

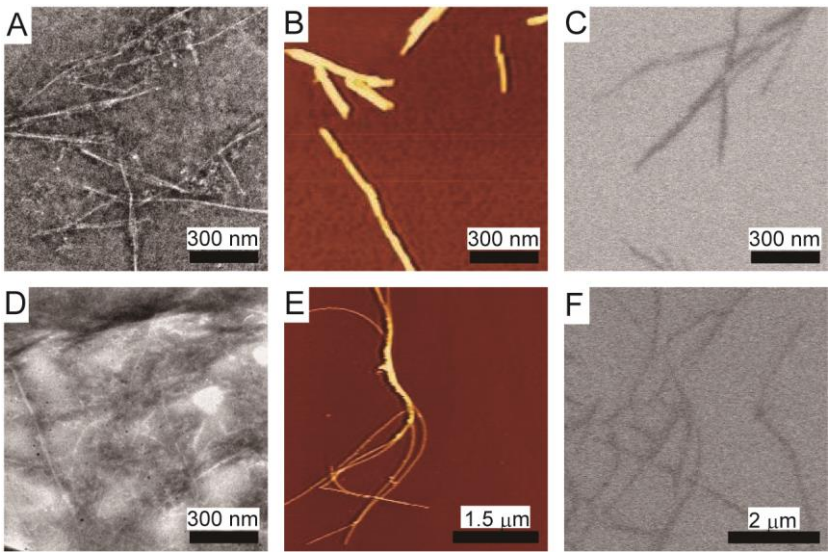


**Figure. 6.2.3.** Comparison of TEM, AFM, and SEM. S-amyloid was monitored by TEM (A), AFM (B) and SEM (C). A-amyloid was monitored by TEM (D), AFM (E) and SEM (F).

## Comparison with fibril-width values in TEM, AFM, and SEM images

Figure 6.2.3 displays large views of S-amyloid and A-amyloid imaged using TEM, AFM and SEM. In the TEM, AFM and SEM images, S-amyloid was consistently observed to form straight mature fibrils with lengths less than 1 μm (Fig. 6.2.3A-C). However, considering the scale of the A-amyloid images, the fibrils shown by SEM were clearly different from those shown by TEM and AFM. Thus, we further analysed the differences in the images of S-amyloid and A-amyloid by TEM, AFM and SEM.

Figure 6.2.4 A-C shows magnified images of a single S-amyloid. The histogram of the apparent width of the fibrils in each image is presented in Fig. 6.2.4D-F. The TEM images of S-amyloid show clear edges of the fibrils, and the centred value of the width was determined to be 12.5 ± 7.0 nm (Fig. 6.2.4A and 6.2.4D). The width determined from the TEM images, 12.5 ± 7.0 nm, was similar to the height of the fibril determined from the AFM images, 8.1 ± 2.4 nm. By contrast, the AFM images of S-amyloid had fine edges and exhibited wider widths of 38.0 ± 7.6 nm (Fig. 6.2.4B and 6.2.4E). This phenomenon is a well-known broadening that reflects the finite curvature of the cantilever, approximately 10 nm [25]. By contrast, the images of S-amyloid by SEM showed fuzzy edges due to its intrinsic lower resolution compared with TEM and AFM (Fig. 6.2.4C and 6.2.4F). The average width in the SEM images was as large as 21.9 ± 5.4 nm. During the SEM measurement, secondary electron emission from the amyloid fibril, which is an insulator, is less likely than that from the silicone plate, which is a semiconducting substrate, resulting in the dark appearance of the amyloid fibril in the SEM image. Thus, there are multiple possible causes of the fuzzy appearance of the edge of the S-amyloid, including (i) the charging of S-amyloid induced by its lower secondary electron emission and (ii) the influence of counter ions ($Na^+$), which produce large secondary electron emissions.

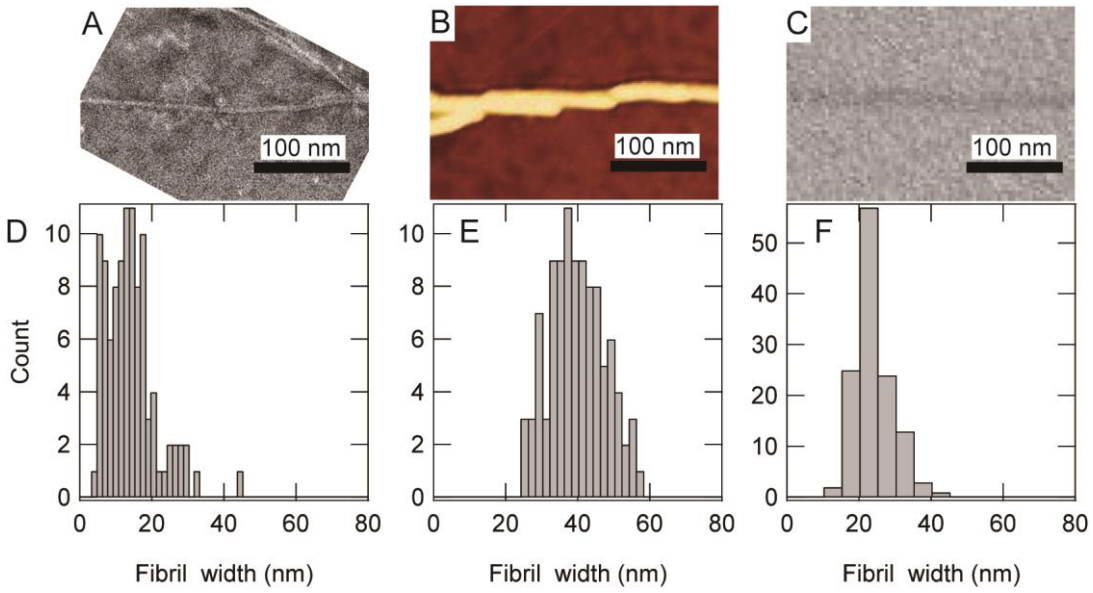


**Figure. 6.2.4.** Width of S-amyloid. Microscopic images of S-amyloid by TEM (A), AFM (B) and SEM (C). Histogram of width of S-amyloid by TEM (D), AFM (E), and SEM (F).

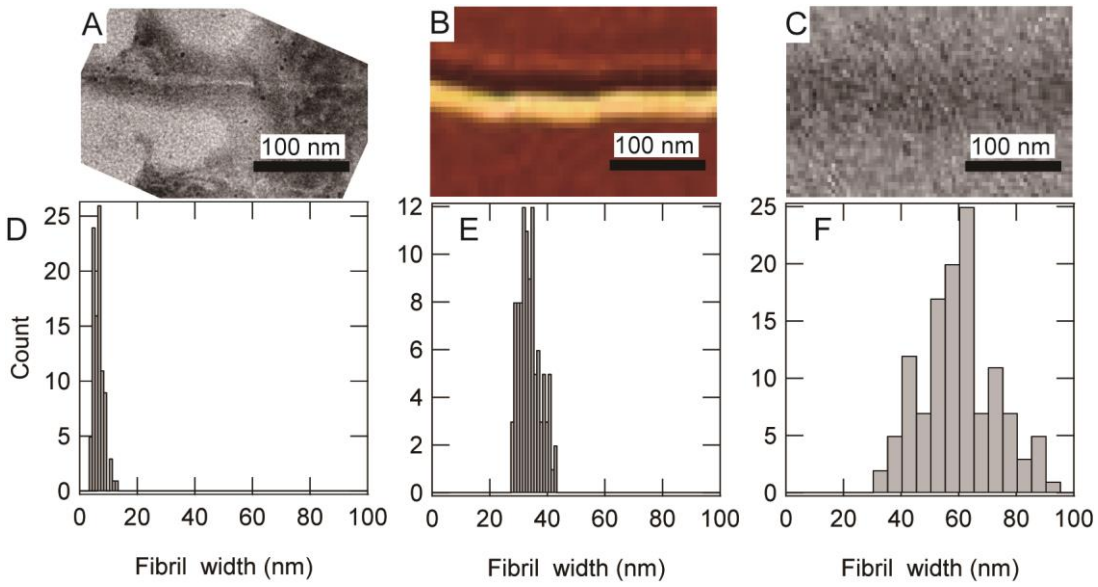


**Figure. 6.2.5.** Width of A-amyloid. Microscopic images of A-amyloid by TEM (A), AFM (B), and SEM (C). Histogram of the width of A-amyloid by TEM (D), AFM (E), and SEM (F).

A-amyloid was similarly characterised by TEM, AFM, and SEM (Fig. 6.2.5). The results for A-amyloid were found to be similar to the results for S-amyloid; the TEM image provides an apparent width of 5.4 ± 1.8 nm, which is close to the fibril height determined by AFM. The apparent width in the AFM image was again found to be as large as 33.1 ± 3.8 nm, reflecting the tip effect. A huge broadening of the apparent width, as large as 57.3 ± 13.6 nm, was observed in the SEM image of A-amyloid, although the original width of A-amyloid was much thinner than that of S-amyloid. This huge broadening of A-amyloid is probably due to the chemical nature of A-amyloid, which differs from the chemical nature of S-amyloid. A-amyloid should be more insulating than S-amyloid. A-amyloid consists of peptide fragments of hydrolysed HEWL and has fewer positively charged residues but more hydrophobic residues, whereas S-amyloid can contain plenty of non-beta-sheet side chains from non-fragmented HEWL, which can potentially be conducting. Thus, considering the different chemical natures of A-amyloid and S-amyloid, some possible causes of the huge broadening of A-amyloid in the SEM image include (i) more charging of A-amyloid and (ii) more influence from counterions ($Na^+$).

**Table 6.2.1.** Diameter and width of amyloid fibrils measured by TEM, AFM, and SEM.

| | | S−amyloid | | A−amyloid | |
|---|---|---|---|---|---|
| | | Sampling number | Average (nm) [a] | Sampling number | Average (nm) [a] |
| Height | AFM | 99 | 8 ±2 | 129 | 4 ±1 |
| | TEM | 102 | 13 ±7 | 96 | 5 ±2 |
| Width | AFM | 100 | 38 ±8 | 101 | 33 ±4 |
| | SEM | 125 | 22 ±5 | 123 | 57 ±14 |

[a] The average and standard deviation of the sampled fibril width and height are shown.

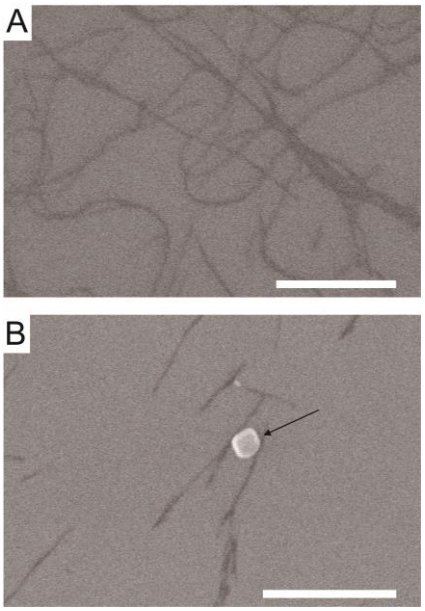


**Figure. 6.2.6.** (A) SEM image of A-amyloid. The scale bar is 3 μm. (B) SEM image of S-amyloid and a salt microcrystal (black arrow). The scale bar is 1 μm.

## Advantages of SEM for imaging of amyloid fibrils

The apparent width of amyloid fibrils by SEM was shown to be 7 to 10 times broader than the original value (Table 6.2.1). This broadening is not desirable for the detailed characterisation of the fibril structure, but the broadening of the apparent contrast can be utilised to increase the detectability of small fibrils. Indeed, in a large view, A-amyloid with diameters as small as 3.5 nm can be detected, as well as thicker fibrils (Fig. 6.2.6A). Although further characterisation of the relationship between the SEM appearance and the structure and composition of the amyloid fibrils is required, the high detectability of the small fibrils is useful for the screening of amyloid fibrils formed in vivo and in vitro.

A-amyloid and small crystals of NaCl were clearly distinguished in the SEM image (Fig. 6.2.6B). Amyloid fibrils are usually dispersed in the solution with other solutes, such as inorganic salts and low-molecular-weight compounds for pH buffering. These other solutes often disturb microscopic measurements in AFM and TEM. However, SEM clearly distinguishes amyloids from these contaminants because the secondary electron emission is sensitive to chemical natures (Fig. 6.2.6B). The easy distinction from contaminants indicates that SEM should be the first choice of microscopic measurement for amyloid fibril imaging.

# Conclusion

This study examined SEM images of two types of amyloid fibrils compared with well-characterised AFM and TEM images. Although the resolution of SEM was found to be poor for insulating amyloid fibrils, even conventional SEM was able to detect amyloid fibrils as thin as 3.5 nm in width through broadening in the image. The broadening effect was also found to be dependent on the chemical composition of the fibril,

which can be further utilised in chemical discrimination. Although further characterisation of the dependence of the chemical properties on the apparent broadening will be required, the several advantages of SEM, in combination with other observations in solution, such as the TIRFM system [26-29], cryo-TEM [30, 31], and in-liquid AFM [32], contribute to the investigation of amyloid fibrils.

# References


[1] Ikawa S, Kitano K and Hamaguchi S 2010 Effects of pH on Bacterial Inactivation in Aqueous Solutions due to Low-Temperature Atmospheric Pressure Plasma Application *Plasma Processes and Polymers* **7** 33-42

[2] Takai E, Kitano K, Kuwabara J and Shiraki K 2012 Protein Inactivation by Low-temperature Atmospheric Pressure Plasma in Aqueous Solution *Plasma Processes and Polymers* **9** 77-82

[3] Takai E, Ikawa S, Kitano K, Kuwabara J and Shiraki K 2013 Molecular mechanism of plasma sterilization in solution with the reduced pH method: importance of permeation of HOO radicals into the cell membrane *Journal of Physics D-Applied Physics* **46** 295402

[4] Knowles T P J and Buehler M J 2011 Nanomechanics of functional and pathological amyloid materials *Nature Nanotechnology* **6** 469-79

[5] Hamada D, Tsumoto K, Sawara M, Tanaka N, Nakahira K, Shiraki K and Yanagihara I 2008 Effect of an amyloidogenic sequence attached to yellow fluorescent protein *Proteins-Structure Function and Bioinformatics* **72** 811-21

[6] Sakono M, Akiyama S, Zako T, Sakaki S, Waku T, Tanaka N and Maeda M 2011 Application of two morphologically different fibrillar and filamentous insulin amyloids as a biomaterial for cell culture surfaces *React. Funct. Polym.* **71** 324-8

[7] Reches M and Gazit E 2003 Casting metal nanowires within discrete self-assembled peptide nanotubes *Science* **300** 625-7

[8] Sasahara K, Yagi H, Naiki H and Goto Y 2007 Heat-induced conversion of beta(2)-Microglobulin and hen egg-white lysozyme into amyloid fibrils *J. Mol. Biol.* **372** 981-91

[9] Morel B, Varela L and Conejero-Lara F 2010 The Thermodynamic Stability of Amyloid Fibrils Studied by Differential Scanning Calorimetry *J. Phys. Chem. B* **114** 4010-9

[10] Kardos J, Yamamoto K, Hasegawa K, Naiki H and Goto Y 2004 Direct measurement of the thermodynamic parameters of amyloid formation by isothermal titration calorimetry *J. Biol. Chem.* **279** 55308-14

[11] Nilsson M R 2004 Techniques to study amyloid fibril formation in vitro *Methods* **34** 151-60

[12] Anderson M, Bocharova O V, Makarava N, Breydo L, Salnikov V V and Baskakov I V 2006 Polymorphism and ultrastructural organization of prion protein amyloid fibrils: an insight from high resolution atomic force microscopy *J Mol Biol* **358** 580-96

[13] Chamberlain A K, MacPhee C E, Zurdo J, Morozova-Roche L A, Hill H A, Dobson C M and Davis J J 2000 Ultrastructural organization of amyloid fibrils by atomic force microscopy *Biophys J* **79** 3282-93

[14] Relini A, Rolandi R, Bolognesi M, Aboudan M, Merlini G, Bellotti V and Gliozzi A 2004 Ultrastructural organization of ex vivo amyloid fibrils formed by the apolipoprotein A-I Leu174Ser variant: an atomic force microscopy

study *Biochim Biophys Acta* **1690** 33-41

[15] Ikeda S and Morris V J 2002 Fine-stranded and particulate aggregates of heat-denatured whey proteins visualized by atomic force microscopy *Biomacromolecules* **3** 382-9

[16] Khurana R, Ionescu-Zanetti C, Pope M, Li J, Nielson L, Ramirez-Alvarado M, Regan L, Fink A L and Carter S A 2003 A general model for amyloid fibril assembly based on morphological studies using atomic force microscopy *Biophys. J.* **85** 1135-44

[17] Lashuel H A and Wall J S 2005 Molecular electron microscopy approaches to elucidating the mechanisms of protein fibrillogenesis *Methods Mol Biol* **299** 81-101

[18] Arimon M, Diez-Perez I, Kogan M J, Durany N, Giralt E, Sanz F and Fernandez-Busquets X 2005 Fine structure study of Abeta1-42 fibrillogenesis with atomic force microscopy *FASEB J.* **19** 1344-6

[19] Adamcik J, Jung J M, Flakowski J, De Los Rios P, Dietler G and Mezzenga R 2010 Understanding amyloid aggregation by statistical analysis of atomic force microscopy images *Nature Nanotechnology* **5** 423-8

[20] Morshedi D, Rezaei-Ghaleh N, Ebrahim-Habibi A, Ahmadian S and Nemat-Gorgani M 2007 Inhibition of amyloid fibrillation of lysozyme by indole derivatives - possible mechanism of action *FEBS J.* **274** 6415-25

[21] Hirano A, Uda K, Maeda Y, Akasaka T and Shiraki K 2010 One-Dimensional Protein-Based Nanoparticles Induce Lipid Bilayer Disruption: Carbon Nanotube Conjugates and Amyloid Fibrils *Langmuir* **26** 17256-9

[22] Lara C, Adamcik J, Jordens S and Mezzenga R 2011 General Self-Assembly Mechanism Converting Hydrolyzed Globular Proteins Into Giant Multistranded Amyloid Ribbons *Biomacromolecules* **12** 1868-75

[23] Jin Y and Manabe T 2005 High-efficiency protein extraction from polyacrylamide gels for molecular mass measurement by matrix-assisted laser desorption/ionization-time of flight-mass spectrometry *Electrophoresis* **26** 1019-28

[24] Edgcomb S P and Murphy K P 2002 Variability in the pKa of histidine side-chains correlates with burial within proteins *Proteins-Structure Function and Genetics* **49** 1-6

[25] Matsubara K, Kelly K L, Sakai N and Tatsuma T 2009 Plasmon resonance-based photoelectrochemical tailoring of spectrum, morphology and orientation of Ag nanoparticles on TiO2 single crystals *J. Mater. Chem.* **19** 5526-32

[26] Ozawa D, Yagi H, Ban T, Kameda A, Kawakami T, Naiki H and Goto Y 2009 Destruction of amyloid fibrils of a beta2-microglobulin fragment by laser beam irradiation *J Biol Chem* **284** 1009-17

[27] Ozawa D, Kaji Y, Yagi H, Sakurai K, Kawakami T, Naiki H and Goto Y 2011 Destruction of amyloid fibrils of keratoepithelin peptides by laser irradiation coupled with amyloid-specific thioflavin T *J Biol Chem* **286** 10856-63

[28] Yagi H, Ozawa D, Sakurai K, Kawakami T, Kuyama H, Nishimura O, Shimanouchi T, Kuboi R, Naiki H and Goto Y 2010 Laser-induced propagation and destruction of amyloid beta fibrils *J Biol Chem* **285** 19660-7

[29] Ban T, Yamaguchi K and Goto Y 2006 Direct observation of amyloid fibril growth, propagation, and adaptation *Acc. Chem. Res.* **39** 663-70

[30] Jimenez J L, Guijarro J L, Orlova E, Zurdo J, Dobson C M, Sunde M and Saibil H R 1999 Cryo-electron microscopy structure of an SH3 amyloid fibril and model of the molecular packing *EMBO J.* **18** 815-21

[31] Jimenez J L, Tennent G, Pepys M and Saibil H R 2001 Structural diversity of ex vivo amyloid fibrils studied by cryo-electron microscopy *J. Mol. Biol.* **311** 241-7

[32] Liu P, Zhang S, Chen M S, Liu Q, Wang C X, Wang C, Li Y M, Besenbacher F and Dong M D 2012 Co-assembly of human islet amyloid polypeptide (hIAPP)/insulin *Chem. Commun.* **48** 191-3

# Chapter 6

# General Discussion

The molecular mechanisms underlying plasma sterilization in solution was demonstrated. Low-temperature atmospheric-pressure plasma has attracted considerable attention for its use in medical applications involving the sterilization of biological tissue. With the use of plasma, a high level of bactericidal activity can be achieved in acidic solutions by means of the reduced pH method. Thus, the data indicate that the pH dependence of sterilization results from the difference in the semipermeability of radicals that penetrate the biomembrane. The reduced pH method involves the permeation of chemically reactive non-charged radicals (·OOH) into the cell membrane. The effective permeation of radicals into the cell membrane, in combination with the modification of the cell membrane, implies the possibility of using plasma therapy to remove cancer cells.

Alkyl gallates have pharmacological activity, such as antibacterial and antiviral activities, which are affected by the alkyl chain length of the alkyl gallates. However, physicochemical mechanisms for the effects of the alkyl chain length have not been clarified. Assuming that the membrane-binding affinity of the alkyl gallates is related with their activity, we investigated the effects of the alkyl chain length on the affinity. Consequently, results reported herein for the first time show that the alkyl chain length dependence on the membrane- binding affinity occurs according to three mechanisms: (1) Short alkyl chain species does not bind into the membrane. (No Membrane-binding), (2) Middle alkyl chain species bind into the membranes because of their hydrophobic alkyl chain. (Membrane-binding), (3) Long alkyl chain species self-associate rather than bind to the membrane. (Self-association). Actually, results show that the above membrane-binding affinity correlated with their pharmacological activity, suggesting the validity of the assumption presented above. This finding will be useful to enhance the bioavailability of the alkyl gallates by preventing the self-association using co-existing solutes.

To provide fundamental insights into the mechanism of action of plasma medicine, we reports the chemical effects of atmospheric-pressure cold plasma on 20 naturally occurring amino acids (the basic building blocks of proteins) in aqueous solution. A competitive reaction experiment with the 20 amino acids demonstrated that sulfur-containing (such as cysteine) and aromatic amino acids were preferentially decreased by the plasma treatment. These data are fundamental information for elucidating the mechanism of protein inactivation for biomedical applications of plasma and represent a crucial first step for understanding the mechanism of action of plasma medicine.

In this thesis, we investigate the chemical effects of APCP on protein in aqueous solution using lysozyme as a model protein. Plasma medicine as a plasma process is one of the new attractive research areas. Our APCP can sterilize bacteria in aqueous solution because the

bactericidal effect of the plasma is caused free radicals. To our knowledge, it is the first report that atmospheric plasma decreases the enzymatic activity of protein to provide fundamental insights into the mechanism of action of plasma medicine.

One of the amino acids, arginine (Arg), synergistically solubilized myosin at physiological salt concentrations without altering the tertiary structure. Myosin, an important protein resource for food industries, is practically insoluble in aqueous solutions at low ionic strength. The solubilization of insoluble myosin in physiological salt concentrations is required for the food industry. Therefore, a new function of Arg as a solution additive was found in which Arg stabilizes the supersaturated state of myosin in saline. This finding of Arg can be applied not only in the food industry but also in pharmaceutical applications of various proteins.

As a plasma-medicine application, APCP was applied to degenerate amyloid-ß (Aß) fibrils, which are a major component of neuritic plaque associated with Alzheimer's disease, in aqueous solution. We showed that the protease resistance of the Aß fibrils was lost as a result of the APCP processing, while the fibril length remained unchanged. These results suggest that APCP could be utilized for the treatment of Alzheimer's disease to eliminate neuritic plaque by accelerating the proteolysis of Aß fibrils.

For the further development of biological technique for the observation of amyloid fibrils, this thesis demonstrates the utility of scanning electron microscopy (SEM) without staining. The apparent fibril widths in the SEM images were considerably larger than the original diameters reported based on the conventional techniques of transmission electron microscopy (TEM) and atomic force microscopy (AFM). Although the broadening is undesirable for detailed imaging, it makes SEM sensitive to fibrils several micrometres in length and as thin as 3.5 nm. Note that the sensitivity also contributed to clearly distinguishing amyloid fibrils from salt microcrystals in the SEM images. These results suggest the high applicability of SEM for the imaging of amyloid fibrils, even in the presence of contamination.

# Chapter 7

# General Conclusion

In this thesis, we investigated the chemical effects of atmospheric-pressure cold plasma on an enzyme hen egg white lysozyme, 20 naturally occurring amino acids, and amyloid-ß fibrils in aqueous solution and the mechanism of plasma sterilization in solution using the reduced pH method. Chapter II describes demonstration of the mechanism of efficient bactericidal inactivation with the reduced pH method, by using 3 kinds of living bacteria and a simple bacterial model. In chapter III, the chemical modification of 20 amino acids in solution by low-frequency (LF) plasma jet, an APCP system was described. The side chains of 14 amino acids were oxidized and sulfur-containing and aromatic amino acids were preferentially modified in the amino acids. Chapter IV presented an investigation that APCP decreases the enzymatic activity of lysozyme and increases the molecular weight of the protein. This study is a first report to elucidating chemical reaction and structural change of protein by the plasma in aqueous solution. Chapter V showed that, using an in vitro system, APCP processing changed the protease resistance, ß-sheet structure, and surface properties of Aß fibrils in solution, although the morphology, length, and cytotoxicity of a plasma-exposed fibril remained unchanged.

LF plasma jet was used as an APCP system to examine the chemical effects of atmospheric-pressure cold plasma on an enzyme, hen egg white lysozyme, 20 naturally occurring amino acids, and amyloid-ß fibrils in aqueous solution and the mechanism of plasma sterilization in solution using the reduced pH method. This is the fundamental step for elucidating chemical reactions by plasma and essential for understanding the effect of plasma to human body. The LF plasma jet is a simple APCP system. Therefore, the reported findings in this study may occur when other APCP systems are used. Furthermore, for fundamental understanding of plasma medicine, discussions must be based on not the parameter of plasma generation but that of active species. The showed degeneration of Aß fibrils in solution can be achieved by plasma treatment and the fact suggests prospects for utilizing APCP for the elimination of neuritic plaque associated with AD by accelerating the proteolysis of Aß fibrils.

# List of Publications

**Related Publications**

1) **Eisuke Takai**, Atsushi Hirano, Kentaro Shiraki, Effects of alkyl chain length of gallate on self-association and membrane-binding, *The Journal of Biochemistry*, **2011**, 150, 165-171.
2) **Eisuke Takai**, Katsuhisa Kitano, Junpei Kuwabara, Kentaro Shiraki, Protein inactivation by low-temperature atmospheric pressure plasma in aqueous solution, *Plasma Processes and Polymers*, **2012**, 9, 77‑82.
3) **Eisuke Takai**, Satoshi Ikawa, Katsuhisa Kitano, Junpei Kuwabara, Kentaro Shiraki, Molecular mechanism of plasma sterilization in solution with the reduced pH method: importance of permeation of HOO radicals into cell membrane, *Journal of Physics D: Applied Physics*, **2013**, 46, 295402.
4) **Eisuke Takai**, Shunsuke Yoshizawa, Daisuke Ejima, Tsutomu Arakawa, Kentaro Shiraki, Synergistic solubilization of porcine myosin in physiological salt solution by arginine, *International Journal of Biological Macromolecules*, **2013**, 62, 647–651.
5) **Eisuke Takai**, Gai Ohashi, Tomonori Yoshida, Karin Margareta Sorgjerd, Tamotsu Zako, Mizuo Maeda, Katsuhisa Kitano, Kentaro Shiraki, Degeneration of amyloid-ß fibrils by low temperature atmospheric pressure plasma in solution. *Applied Physics Letters*, **2014**, 104, 023701.
6) **Eisuke Takai**, Gai Ohashi, Ryuichi Ueki, Yoichi Yamada, Jun-ichi Fujita, Kentaro Shiraki, Scanning electron microscope imaging of amyloid fibrils. Submitted.

**Other Publications**

1) Naoto Inoue, **Eisuke Takai**, Tsutomu Arakawa, Kentaro Shiraki Arginine and lysine reduce the high viscosity of serum albumin solutions for pharmaceutical injection. *Journal of Bioscience and Bioengineering*, **2013**, 13, 1389-1723.
2) **Eisuke Takai**, Ken Uda, Tomonori Yoshida, Tamotsu Zako, Mizuo Maeda, Kentaro Shiraki, Cysteine inhibits the fibrillisation and cytotoxicity of amyloid-ß 40 and 42: implications for the contribution of the thiophilic interaction. *Physical Chemistry Chemical Physics*, **2014**, DOI: 10.1039/c3cp54245a.
3) **Eisuke Takai**, Ken Uda, Shuhei Matsushita, Yui Shikiya, Yoichi Yamada, Zako Tamotsu, Mizuo Maeda, Kentaro Shiraki, Cysteine inhibits amyloid fibrillation of lysozyme and directs the formation of small worm-like aggregates through non-covalent interactions. *Biotechnology Progress*, **2014**, DOI 10.1002/btpr.1866.
4) **Eisuke Takai**, Tsuyoshi Kitamura, Junpei Kuwabara, Satoshi Ikawa, Shunsuke Yoshizawa, Kentaro Shiraki, Hideya Kawasaki, Ryuichi Arakawa, Katsuhisa Kitano, Chemical modification of amino acids by atmospheric-pressure cold plasma in aqueous solution. Submitted.
5) Naoto Inoue, **Eisuke Takai**, Tsutomu Arakawa, Kentaro Shiraki, Specific decrease in solution viscosity of antibodies by arginine for therapeutic formulations. Submitted.

# Acknowledgements

This dissertation is dedicated to all the people who have supported the author.

The studies described herein were conducted under the direction of Associate Professor Kentaro Shiraki, Institute of Applied Physics, University of Tsukuba. The author extends his sincerest gratitude to Associate Professor Kentaro Shiraki for helpful advice and timely guidance during this study.

To Professor Jun-ichi Fujita, Associate Professor Muneaki Hase (University of Tsukuba), and Associate Professor Tamotsu Zako (RIKEN Institute), the author is deeply indebted for their critical comments, which were valuable for preparing this dissertation for submission.

Professor Yukio Nagasaki, Professor Masahiro Sasaki, Associate Professor Junpei Kuwabara, Assistant Professor Yoichi Yamada, and Dr. Ryuichi Ueki (University of Tsukuba), Dr. Tsutomu Arakawa (Alliance Protein Laboratories, USA), Dr. Daisuke Ejima (Ajinomoto Co., Inc.), Professor Mizuo Maeda, Dr. Karin Margareta Sörgjerd, and Mr. Tomonori Yoshida, (RIKEN Institute), Associate Professor Katsuhisa Kitano (Osaka University), Dr. Satoshi Ikawa (TRI Osaka), Mr. Tsuyoshi Kitamura (Kansai University), and Dr. Tomoshi Kameda and Dr. Atsushi Hirano (Advanced Industrial Science and Technology) are also appreciated for their invaluable discussion, suggestions, and technical advice. Professor Toshiaki Hattori, and Mr. Katsuyoshi Aoki (University of Tsukuba) are acknowledged for their valuable technical advice. Associate Professor Yohei Yamamoto and Mr. Toru Nakayama are acknowledged for their valuable experimental helps.

The author expresses thanks also to the members of Associate Professor Shiraki's laboratory—including Messrs. Dr. Shunsuke Tomita, Akiko Fujimoto, Ken Uda, Ryosuke Ariki, Soichiro Kayano, Syuhei Matsushita, Ryo Shirato, Kohei Kabei, Hiroki Yoshikawa, Yui Shikiya, Daisuke Shinozaki, Chie Tanaka, Takaaki Kurinomaru, Masato Shimada, Yumiko Tanabe, Yuuri Kamiyama, Naoto Inoue, Gai Ohashi, Shunsuke Yoshizawa, Takuya Maruyama, Kazuki Iwasaki, and Kengo Kuwabara —for their technical assistance, kind cooperation, and friendship.

Finally, for their hearty encouragement and support, the author extends his warmest appreciation to his parents and brother.

Eisuke Takai

February, 2014